Laser-ultrasonics and imaging through metal layers

Ph.D. thesis, Vrije Universiteit Amsterdam, 2022
Laser-Ultrasonics and Imaging through Metal Layers.
Alessandro Antoncecchi

ISBN
An electronic version of this dissertation is available at: research.vu.nl

Cover design: The composition has been designed by the author. It represents the pump and probe hitting a gold metal layer which is covering the city Amsterdam. The Amsterdam skyline has been designed by: Freepik.

VRIJE UNIVERSITEIT

LASER-ULTRASONICS AND IMAGING THROUGH METAL LAYERS

ACADEMISCH PROEFSCHRIFT

ter verkrijging van de graad van Doctor of Philosophy
aan de Vrije Universiteit Amsterdam,
op gezag van de rector magnificus
prof.dr. J.J.G. Geurts,
in het openbaar te verdedigen
ten overstaan van de promotiecommissie
van de Faculteit der Bètawetenschappen
op woensdag 30 maart 2022 om 13.45 uur
in een bijeenkomst van de universiteit,
De Boelelaan 1105

door

Alessandro Antoncecchi

geboren te Bari, Italië

promotoren:	dr. S.M. Witte prof.dr. K.S.E. Eikema
promotiecommissie:	prof.dr. A. Freise dr. I. Avci prof.dr. E. Verhagen prof.dr. B. Audoin prof.dr. I. Setija

The work described in this thesis was carried out at the Advanced Research Center for Nanolithography (ARCNL), a public-private partnership between the University of Amsterdam (UvA), the Vrije Universiteit Amsterdam (VU), the Netherlands Organisation for Scientific Research (NWO), and the semiconductor equipment manufacturer ASML.

Contents

Summary

Electronic devices, such as personal computers and smartphones, are continuously growing in terms of calculation power, while their dimensions are shrinking, making them convenient tools for daily-life activities and business. To obtain smaller but powerful devices, manufacturers use more complex circuit design for their microchips. Modern circuits are no longer limited to one plane, but also extend also in the vertical dimension, transforming the microchip into a 3D architecture at small scales. Manufacturers need to be very precise in the fabrication steps to have all the different layers accurately aligned. Before printing a circuit on a new layer, the machine determines the position of the silicon wafer using optical alignment sensors. The alignment process relies on the collection of light diffracted by alignment gratings etched on the wafer. Interferometric measurements of the phase difference between the $+1^{st}$ and -1^{st} diffraction orders allow the determination of wafer position with sub-nm accuracy. However, the complexity of the circuit design sometime requires that multiple material layers are deposited on top of the wafer. In such cases, the alignment gratings become invisible to light. In contrast, sound would still be able to propagate through such optically opaque layers.

The combination of light and sound can be used to detect and image structures under opaque layers. In this thesis, we present the result of our studies on imaging and metrology through metal layers using laser-induced ultrasound. Ultrafast lasers can generate acoustic waves at high frequencies through the thermoelastic effect. The absorption of the energy of the laser pulse is followed by an increase in temperature and a subsequent expansion of the metal lattice. Stress is generated in the lattice, launching an acoustic wave inside the metal layer. The acoustic waves travel through the layers that compose the samples, reflecting off different interfaces and returning to the surface. When the reflected acoustic pulse comes back to the surface, it causes a change in the optical constants, as well as a physical displacement of the surface. A second laser pulse can be used to detect these changes in optical properties of the surface caused by the acoustic wave. In our research, we performed pump-probe experiments to study the generation, propagation and detection of ultrasound waves in metal layers.

After a small review on laser-induced ultrasound in Chapter 2, we present the experimental results. Chapter 3 reports the pump-probe measurements on gold layers in the first 10 ps after the pump pulse. The energy of the pump laser is partially absorbed by the free-electron gas, which increases its temperature. The electron gas thermalizes with the lattice. Simultaneously the electron energy diffuses out the excitation region. As a result, the lattice temperature rises over a depth that extends beyond the optical penetration depth. The extension of the heated region determines the properties of the acoustic waves. The results of Chapter 3 show how the electron dynamics are influenced not only by the electron-phonon coupling of the metal illuminated by the pump laser but also by the thickness of the metal and the presence of a buried layer.

Acoustic wave generation and propagation occur at a longer time scale. Measurements for longer pump-probe time delay are reported in Chapter 4 and Chapter 5. For these measurements, we use two different configurations to generate ultrasound waves and study different propagating modes. In the experiments presented in Chapter 4, we use a transient grating to pump free-standing metal layers. A grating-shaped acoustic wave is launched in the metal layer. We measure the diffraction of the probe beam as function of delay time to detect the acoustic waves. The experimental results are used in combination with an advanced numerical model to distinguish the contribution of the surface displacement and the strain-optic effects to the signal. In the simulations, based on the numerical model, we observe various mode of the propagating waves. In particular, we can identify the Lamb waves supported by a free-standing layer. Lamb waves are guided modes propagating in the lateral direction along the surface. In the experiment reported in Chapter 5, we use a focused pump beam to generate Lamb waves that propagate radially from the pump spot. We measure the reflectivity change of the surface. To study the evolution of Lamb waves in the lateral direction, we scan the position of the probe beam. Reflectivity measurements for different distances between pump-probe are included in this chapter. The analysis of the measurements is performed using a 2D version of the numerical model, which allowed the identification of the main component to the lateral propagation as the S_0 symmetric Lamb mode. Furthermore, the fit of the numerical model to the measurements enables quantification of several material parameters, such as the strain-optic coefficients.

The strain-induced relative reflectivity changes induced by the acoustic wave

are on the order of 10^{-4}. In the experimental setup, we use a lock-in amplification scheme to improve the signal to noise ratio of the signal coming from the detector. To increase the signal strength, we explore the physics underlying the detection of acoustic waves. The detection of the strain-induced reflectivity changes is subject to the light-matter interaction at the material interface. Boundary conditions require that the stress is always zero at the surface. Having zero stress at the surface greatly influence the detectable signal since the probe intensity is highest at the surface. In this case, the signal strongly depends on the penetration depth of the probe and the strain within this depth range. In metals, the penetration depth is on the order of a few nm, resulting in a limited detection efficiency of the acoustic waves. In Chapter 6, we show numerical and experimental evidence of the role of boundary conditions on the detection of acoustic waves.

In the final chapter of the thesis (Chapter 7), we show an application of laser-induced ultrasound. A scanning pump-probe microscope has been built to detect and to image structures buried underneath opaque layers. We find that the returning echoes provide sufficient contrast to reconstruct the topography of buried interfaces. The resolution of the microscope is limited by the spot size of the probe beam,beam, and that the presence of the metal layer does not degrade this resolution. We compare the images obtained with the scanning pump-probe technique with AFM images, recorded from the structured side of the samples. The height profiles determined from the spatially resolved pump-probe time delay scans agree with the AFM reference measurements within the experimental accuracy.

1

Introduction

1

1.1. Motivation

During the last century, the world has witnessed exponential technological growth in the field known as Information and Communication Technologies (ICT). Just before the beginning of the 20^{th} century, the first radio was invented. The first computers were used by English cryptologists to decipher the encrypted communication of the German army during World War II. These computers were as large as laboratory rooms. However, in the last decade of the century, it became common to find devices like telephones and Personal Computers (PC) in every home. Fast enough, portable version of these devices were already available in the market. In the last twenty years, smartphones became part of our daily lives. The smartphone combines the functionalities of both phones and computers, allowing us to communicate with each other and do all our daily activities from any part of the world, using a single and small device.

This technological revolution started with the invention of the transistor. Transistors are electronic switching elements that allow electronic devices to perform logical operations and computational tasks. A device with many transistors can perform multiple logical operations in parallel, increasing its computational power. This is why technological advances has an intimate link with the miniaturization of the integrated circuit. Gordon E. Moore, the co-founder of Intel, predicted in 1965 that the number of transistors in a given unit of area would double every year [1]. After some time the prediction was adjusted so that the number of transistors per unit area is expected to double every 2 years. This prediction is known as Moore's law and the semiconductor industry uses it as guidance for their production road-maps.

Nowadays, the number of transistors per mm^2 is $\approx 40 MT/mm^2$ (where MT stands for "Mega Transistor") [2]. To achieve ever higher transistor density in an integrated circuit, the transistor size has now shrunken down to few nanometers. The fabrication technique with which micro-chips are created at nanometer scales is called "photo-lithography". The name itself describes the process: light (from the Greek "phos") is used to print ("graphein" means "to write" or "to draw") a pattern on a wafer of a semiconductor material ("lithos" means "stone", referring to the silicon). Figure 1.1 illustrates the steps involved in photo-lithography. First, a photo-resist layer is deposited on top of the wafer. A photo-resist is a polymer with the property of changing its solubility after being exposed to short-wavelength light. Two types of photo-resist exist: positive and negative. A photo-resist is positive if it

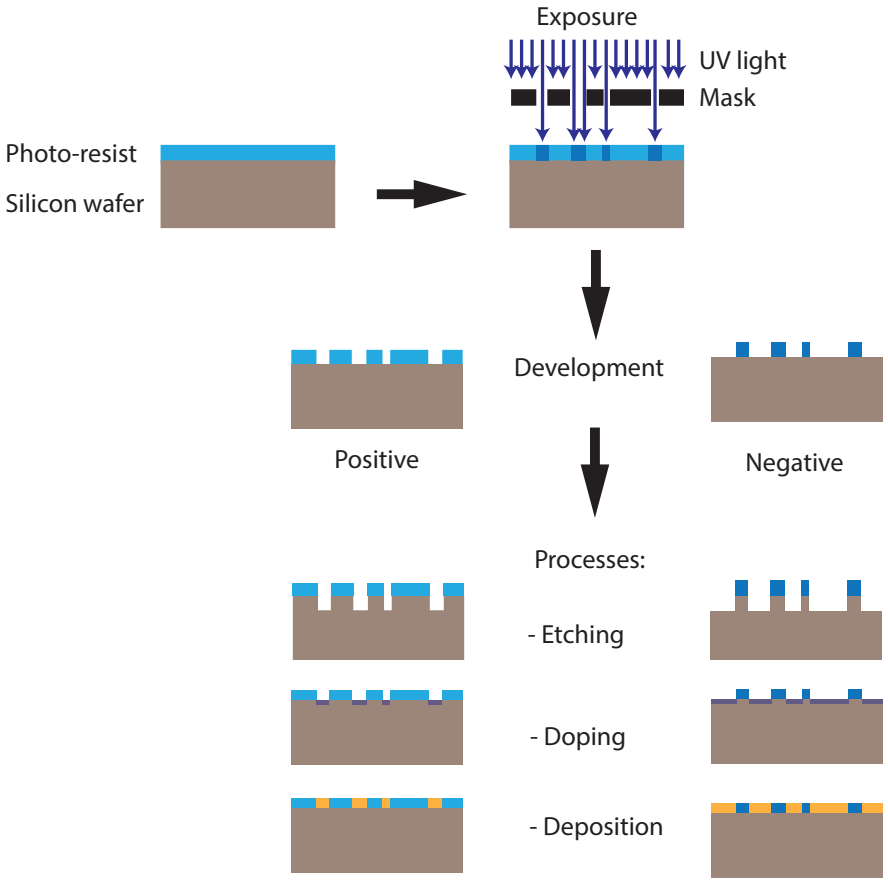

Figure 1.1: The photo-lithography steps. The silicon wafer is covered by a layer of photo-resist Then, the photo-resist is exposed to UV light which passes through a mask. In this way, a pattern is printed to the resist layer, after the development. The uncovered areas are exposed to different kind of fabrication processes, like doping and etching. These steps can be iterated according to the design of the microchip.

becomes more soluble after exposure to the light, while a negative resist becomes less soluble. In the second step of photo-lithography, we use the light transmitted through a mask to expose the wafer with the photo-resist on top. The mask is used to shape the intensity distribution of the light according to a designed pattern. The development of the pattern in the resist layer is obtained in the next step, by immersing the wafer in a developer. The parts of the resist exposed to the light are dissolved. However, if it is a negative resist, the unexposed parts are dissolved. At this point, the wafer

parts left uncovered can go through different processes: etching, doping or a new material deposition. All these steps are iterated multiple times until the entire micro-chip is created.

The size of the smallest feature that can be printed is determined by the diffraction limit and it is referred to as critical dimension (CD). This limit is described by a modified Rayleigh equation, $CD = k_1 \frac{\lambda}{NA}$, where k_1 is a constant related to the fabrication process, NA is the numerical aperture of the optical system and λ is the wavelength of the light used. From the expression of the CD, it is evident that if shorter wavelengths are used, smaller features can be printed.

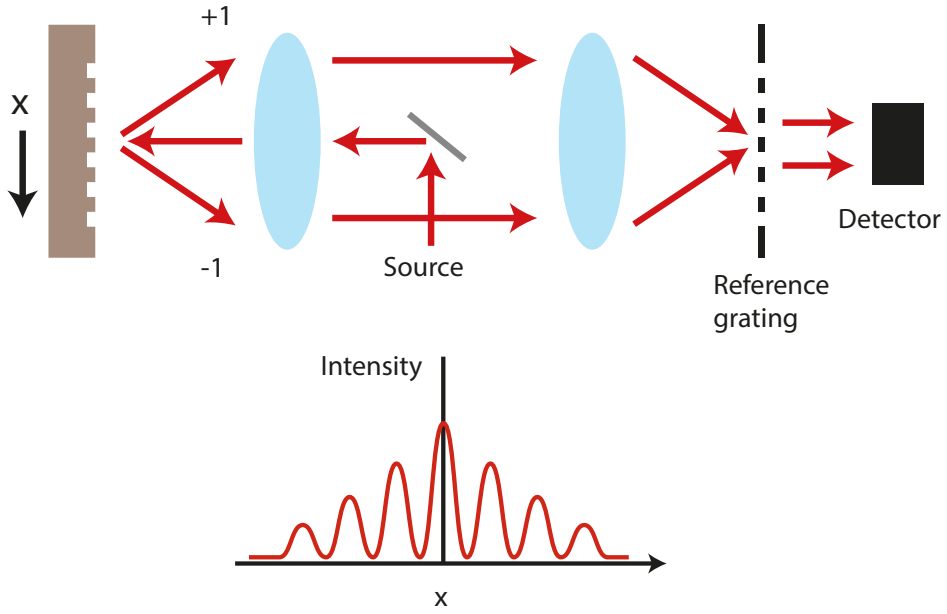

Figure 1.2: Working principle of the alignment sensor. The diffraction from the alignment grating is collected. The +1 and -1 diffraction order interfere with each other on the plane of the reference grating. The detector measures the intensity transmitted from the reference grating while the wafer is scanned along the direction of the grating vector. An interferogram is recorded and its signal is maximum at the centre of the grating.

ASML, a leading company in the nano-lithography industry, is delivering a new generation of scanners, the machines where wafers are exposed to light. The resolution of the new scanners is strongly enhanced by the use of extreme

ultra-violet radiation at a wavelength of 13.5 nm. However, even though the use of short wavelength light reduces the fundamentally achievable CD, there are other aspects of the printing procedure that can degrade the performance of the scanner. As mentioned, micro-chips are fabricated layer after layer. Positioning of the wafer affects the vertical alignment between neighbouring layers, degrading for example the electronic connection between them. So, it is critical that before the exposure of the new layer the position of the wafer is known with high accuracy. Currently, wafer alignment is done by detecting markers in different locations of the wafer. These markers are usually gratings and their absolute position can be measured by recording the interferogram of the $+1^{st}$ and -1^{st} orders while scanning the wafer across the grating, in the direction perpendicular to the lines. The simplified working principle is illustrated in Figure 1.2. During the scan of the wafer, the diffraction efficiency of the grating stays the same while the phase difference between plus and minus order changes. An example of the signal measured by the detector as function of the grating position is shown at the bottom of Figure 1.2. The oscillations are the result of the phase difference between the two diffraction orders while the envelope is determined by the length of the grating [3, 4]. This method allows aligning the wafer with an accuracy better than a nanometer [3].

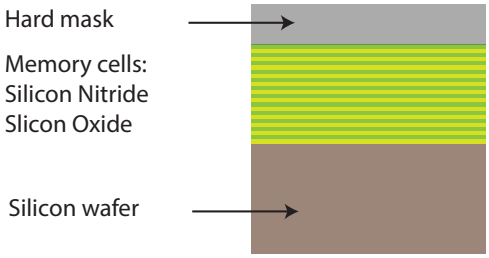

Figure 1.3: The 3D NAND architecture. Alternating layers of silicon nitride and silicon oxide films are placed on top of the silicon wafer. Memory cells composed of these two materials can be fabricated on top of each other, increasing the memory density of the micro-chip. A thick hardmask layer is included to protect the bilayers system during etching processes.

The wavelengths used for the alignment sensors are usually in the visible or infra-red range. The advantage of using light in this range is to maintain a

good resolution while preventing the exposure of the photo-resist layer during the alignment process, plus the availability of bright light sources and detectors in this wavelength range. However, the disadvantage of using visible wavelength is related to the growing complexity of microchips. In fact, more layers are added to the wafer, making the alignment targets invisible to the light. For example, Figure 1.3 shows the design of a new architecture for flash memory chips, called 3D NAND. The alternating layers of silicon nitride and silicon oxide allow to stack memory cells on top of each other, in contrast with the older design where the cells were arranged in a 2D geometry side by side. The etching processes for the 3D NAND require a longer time due to the increased thickness. As a consequence, a simple photoresist layer can not protect the patterned area during the etching. A stronger and more stable layer is needed. For this reason, a hardmask layer is included in the design of the 3D NAND. This layer is often made of materials that are opaque to IR/visible wavelength, i.e. tungsten, and it can be very thick, even a few microns. The thick hardmask and the multiple bi-layers make it impossible for the visible light to penetrate and see the alignment structures at the wafer level. In the following, we present a possible solution to this problem.

Most materials transmit sound. This property can be used to expand the capabilities of the existing alignment sensor. We developed a method to detect buried structures such as the alignment markers. With this method, we combine the speed and the resolution of the optical wavelength with the long penetration length of sound in many materials. The operation principle is described in Figure 1.4. An ultrafast laser generates an acoustic wave at the surface of the wafer. The acoustic wave propagates inside the layer until it reaches the interface with the target stack. There, the acoustic wave is partially reflected towards the surface. The wavefront of the acoustic wave is modified by the presence of the structure. After the time needed for the acoustic wave to go back and forth the entire thickness, a ”copy” of the target structure emerges at the surface and diffraction can be measured by illuminating the wafer with a second pulse. The diffraction orders of this second pulse can be used as in a regular alignment sensor.

Outline of the thesis

To study the physical mechanism and the feasibility of our proposed solution based on laser-induced acoustic waves, we have performed studies on the dif-

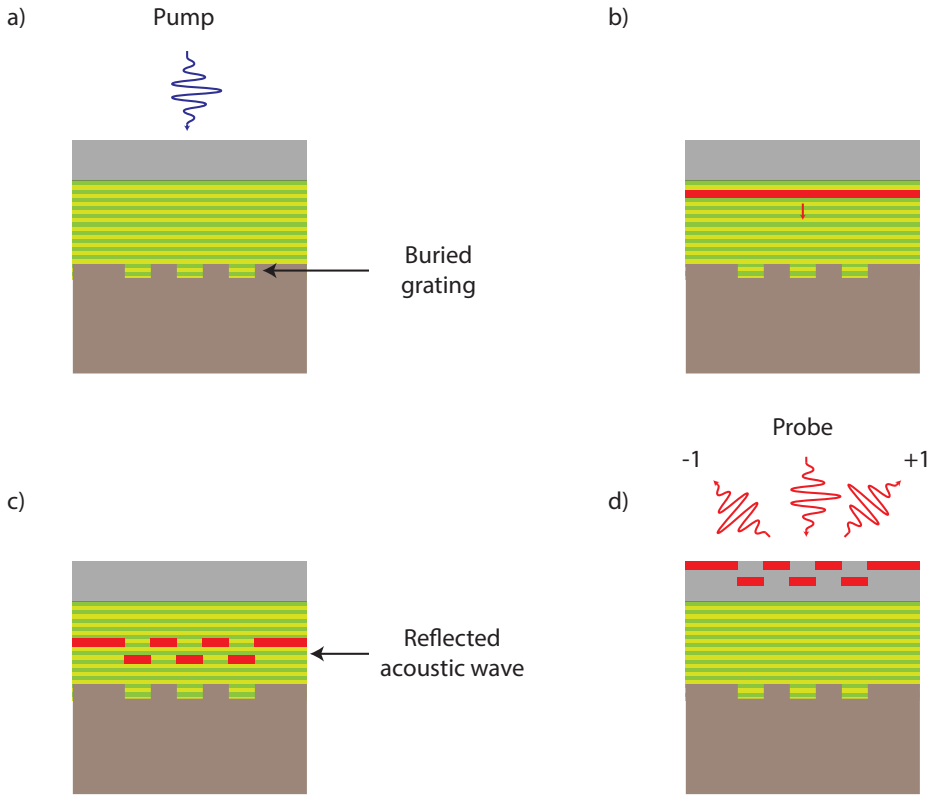

Figure 1.4: Light-induced ultrasound to detect buried structures. a) An ultrafast laser pulse is absorbed by the top layer of the stack. b) After the absorption, an acoustic wave is generated at the surface which propagates through multiple layers until it reaches the alignment grating. c) The acoustic wave is partially reflected at the interface with the grating and returns to the surface with a modified wavefront. There the acoustic wave changes the optical properties of the surface according to the periodic pattern of the grating. d) By measuring the diffraction of a second laser pulse from the surface, the buried grating can be detected.

ferent aspects of photoacoustic measurement. The results of this study are summarized and included in this thesis.

Photoacoustic experiments are governed by thermoelastic laws, the deformation of materials in response to temperature changes. In Chapter 2 we give a theoretical introduction to thermo-elasticity. We describe the generation, propagation and detection of the acoustic waves after a metal absorbs the energy of an ultrafast laser pulse. We introduce the equations that govern these

effects and the numerical model with which we can perform simulations of the experiments. In Chapter 3 we report the results of experiments to measure the electron dynamics in metals. This process influences the generation of the acoustic waves inside metals. In Chapter 4 and Chapter 5 we include the studies on the propagation of acoustic waves in metal layers. Different modes of acoustic waves can be excited according to the different schemes we use to excite the samples during the experiments. Chapter 6 presents a preliminary experiment where we use transparent layers on top of metals to amplify the detected photoacoustic signal. Finally, in Chapter 7 we present an application of a photoacoustic microscope used to image buried structures underneath opaque layers.

2

Thermo-elasticity: laser-induced ultrasound in metals

Parts of this chapter have been published in Phys. Rev. Applied 13, 014010 (2020) [5]

2.1. Introduction

The knowledge of how sound propagates in a specific medium is important for the reconstruction of buried objects and their surrounding. We performed photoacoustic measurements to study the propagation of ultra-sound waves in different opaque materials. To understand the experimental results, we developed an advanced numerical model based on thermoelastic theory. In this chapter, we introduce both the physics and the numerical model used during our research.

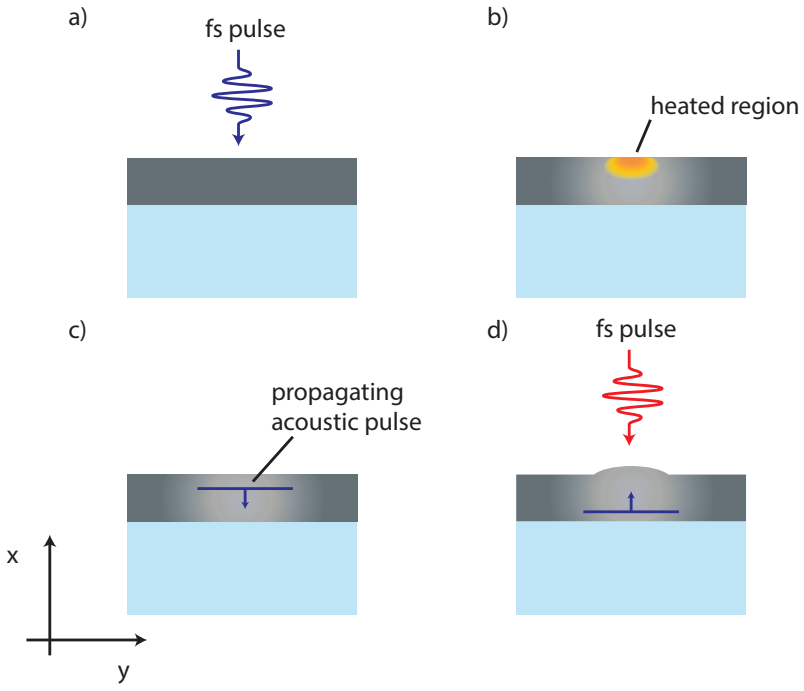

Figure 2.1: Steps of a photoacoustic experiment. a) A fs pulse illuminates the sample surface. Its energy is absorbed by the electrons in the material. b) A gradient of the lattice temperature is caused by the thermalization between hot electrons and lattice. c) An acoustic wave is generated and propagates inside the material. d) The acoustic wave is partially reflected after encountering an interface. Once it returns to the surface, it causes atomic displacement and changes refractive index of the material. A second fs pulse is used to measure the optical changes induced by the acoustic wave.

Fig.2.1 gives an overview of the processes that occur after illuminating the sample with an ultrafast laser pulse. The electrons absorb most of the energy and thermalize with the lattice, which increases its temperature in a time of the order of picosecond. This swift change in lattice temperature generates a thermal stress at the surface and launches an acoustic pulse propagating into the sample. The acoustic pulse changes the local density of the material as it propagates, which can be seen as a propagating strain wave. The presence of strain, together with the temperature increment, alters the optical properties of the material, thus it can be detected using a second laser pulse. In the following, we describe in detail our three-step model on the generation, propagation and detection of laser-excited acoustic waves.

2.2. Generation: two temperature model

Ultrafast lasers can generate high frequency acoustic waves in the GHz to THz range. Depending on the material, different processes are involved in the generation of acoustic waves. The dominant mechanism for sound generation in metals is thermo-elasticity [6]. Since this thesis focuses on the generation of acoustic waves in metals, we discuss only the thermoelastic process.

At macroscopic scales, we are already familiar with the daily experience that when a metal is heated, it expands. This remains true at smaller scales. After illuminating the sample with a laser pulse, the lattice temperature increases and a thermal stress is built up. Since the thermal stress is the origin of acoustic waves, it is important to follow the dynamics of the lattice temperature and study how it evolves in time and space after the absorption of the laser pulse.

In photoacoustic experiments involving ultrafast pulses, the temperature of the lattice does not directly follow the intensity of the illuminating laser pulse. After the illumination, only as a small part of pulse energy is absorbed by the electrons in the metal, while the lattice remains cold. Directly after light absorption, the electrons acquire the energy of the photons, yet their energies have not formed a distribution, i.e., they are in a non-equilibrium state. Via electron-electron scattering processes the electron system thermalizes towards an equilibrium state at an elevated temperature. In the mean time, the electrons, while thermalizing, start to transfer their energy to the lattice, in a process called electron-phonon coupling [7, 8]. To describe these

processes from the absorption of a laser pulse to the electron-phonon energy exchange, we use the following two-temperature model which describes also electron and lattice thermal diffusion [9, 10]:

$$C_e(T_e)\frac{\partial T_e}{\partial t} + \nabla \cdot \mathbf{Q}_e = -G(T_e - T_l) + S \quad , \tag{2.1a}$$

$$\tau_e \frac{\partial \mathbf{Q}_e}{\partial t} + \mathbf{Q}_e = -k_e \nabla T_e \quad , \tag{2.1b}$$

$$C_l(T_l)\frac{\partial T_l}{\partial t} + \nabla \cdot \mathbf{Q}_l = G(T_e - T_l) \quad , \tag{2.1c}$$

$$\tau_l \frac{\partial \mathbf{Q}_l}{\partial t} + \mathbf{Q}_l = -k_l \nabla T_l \quad . \tag{2.1d}$$

Here, C_e and C_l are respectively the heat capacity of the electron gas and the lattice, k_e and k_l are the thermal conductivity for the electron gas and the lattice, respectively, G is the electron-phonon coupling constant, τ_e and τ_e are the electron and lattice relaxation time [9, 10], T_e and T_l describes the spatial distributions of the electron gas temperature and the lattice temperature as function of time, S is the energy source term and $\mathbf{Q}_e$ and $\mathbf{Q}_l$ are the heat fluxes for the electron gas and the lattice. For the lattice we do not consider the temperature dependence of the heat capacity and conductivity. This is justified by the fact that for our experimental conditions the lattice temperature changes only by a few tens of Kelvin. For the electron gas, however, the temperature rise is on the order of a few thousand Kelvin, for which the temperature dependencies cannot be ignored. Thus, we include a linear relation for the heat capacity $C_e = A_e T_e$, and the relation $K_e = K_0 T_e / T_l$ for the heat conductivity [11]. The T_e and T_l are coupled through Eq. (2.1a) and Eq. (2.1c). Thermal diffusions are included in the divergences term involving the heat flux $\mathbf{Q}$.

The source term, S accounts for the energy of the laser pulse absorbed by the electron gas. To calculate it we use a simple Lambert-Beer law:

$$S(x, y, t) = (1 - R) I_0(x, y, t) e^{-x\alpha} \tag{2.2}$$

where R is the sample reflectivity, I_0 the intensity of the incident pulse laser and α is the absorption coefficient which depends on the imaginary part of the refractive index at the pump wavelength.

Lambert-Beer law can be used to calculate the absorption when the metal layer is much thicker than the penetration length. For thinner layers a trans-

fer matrix method is preferred. This method takes into account possible reflection at the interfaces. A more general solution requires to solve the Maxwell equations. However, this is strictly necessary only when the problem involves sub-wavelength structures.

The system of equations Eq. (2.1) can be solved numerically by implementing a Finite Difference Time Domain (FTDT) scheme. In this way, T_e and T_l are calculated at different instants of time. In particular, from T_l we can calculate the thermal stress as [6, 12]:

$$\sigma^{th} = -3B\beta\Delta T_L \tag{2.3}$$

where B is the bulk modulus, β is the linear expansion coefficient and ΔT_L is the increase of lattice temperature from room temperature.
The gradient of (Eq. 2.3) is used as source term in the acoustic wave equation introduced in the next section. The spatial profile of the lattice temperatures depends on the distance at which the electrons and lattice thermalize. From Eq. (2.1a) and Eq. (2.1c), it can be seen that this process is regulated by the electron-phonon coupling constant G.

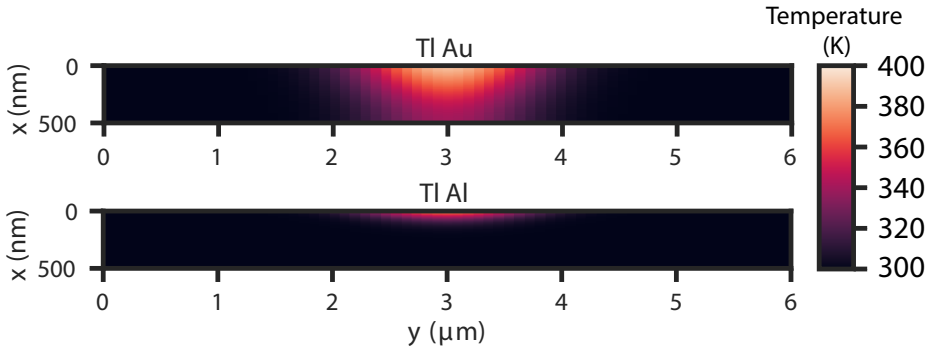

Figure 2.2: Lattice temperature calculated solving the two temperature model with a 2D-FDTD scheme. On the left the lattice temperature for 500 nm of gold (G=2.7 × 10^{16} W/(m^{3}K), and on the right for 500 nm aluminum (G=2 × 10^{17} W/(m^{3}K). The maps show the distribution after 20 ps from the pump pulse.

In Fig. 2.2, we show the lattice temperature distribution after 20 ps in 500 nm of gold and aluminum. In the aluminum case, the electron-phonon coupling constant is: $G_{Al} = 2 \times 10^{17}$ W/(m^{3}K) [11]. The thermalization between electrons and lattice happens at high rate and, hence, the electrons with high energy have no time to diffuse much deeper than the optical skin depth. In this situation, the lattice temperature increases only in a localized area

near the surface of the sample. In contrast, gold is considered to have a low electron-phonon coupling constant $G_{Au} = 2.7 \times 10^{16}$ W/(m^{3}K) [7], an order of magnitude lower than the aluminum one. In this case, the high energy electrons have time to diffuse away from the surface before they start thermalizing with the lattice. Because of this, the lattice heats up homogeneously hundreds of nanometers away from the surface of the metal.

The spatial extension of the temperature gradient has an effect on the frequency spectrum generated. A spatially localized source can generate acoustic wave packets at higher frequency with a short pulse width [6]. We can roughly calculate the characteristic frequency. We can, for example, consider the extension of the source in aluminum to be ≈30 nm (Fig. 2.2), while the speed of sound is ≈ 6 nm/ps. From these two quantities we obtain the temporal pulse width, $\Delta t = 5$ ps. Using the relation $f = \frac{1}{2\pi\Delta t}$ for the characteristic frequency [6, 12], we obtain $f \approx 30$ GHz.

2.3. Acoustic wave propagation

2.3.1. The thermoelastic wave equation

The equation of motion of a point in a material is derived from Newton's second law applied to an infinitesimal volume around that point [13]:

$$\rho a_i = \frac{\partial \sigma_{ij}}{\partial x_j} + f_i \tag{2.4}$$

where ρ is the density of the material, a_i is the acceleration of the point along the i direction, σ_{ij} are the elements of the stress tensor corresponding to the traction forces acting on the material in the direction i and, finally, f_i are the body forces components along the i direction. In the first term of the right hand side of the equation, the indices i and j are in place of the x, y and z direction. We assume a sum over the the possible permutation of the index j. Also for the proceeding we will neglect the body forces, and consider them equal to zero ($\mathbf{f_i} = 0$).

In elastic theory, we can relate the stress tensor to the strain in the material using the famous Hooke's law. The general form of the strain-stress relation is:

$$\sigma_{ij} = c_{ijkl}\epsilon_{kl} \tag{2.5}$$

where c is the stiffness coefficient tensor and ϵ is the strain tensor. The 81 coefficients can be reduced by symmetry considerations for both the strain and stress tensor. Eq. (2.5) is further simplified in the case of an isotropic material, where only 6 coefficients remain independent:

$$c_{ijkl} = \lambda\delta_{ij}\delta_{kl} + \mu(\delta_{ik}\delta_{jl} + \delta_{il}\delta_{jk}) \tag{2.6}$$

where λ and μ are the Lamé parameters and δ stands for the Kronecker delta. Inserting Eq. (2.6) into Eq. (2.5), the stress-strain relation for an isotropic medium is obtained:

$$\sigma_{ij} = \lambda\delta_{ij}\epsilon_{kk} + 2\mu\epsilon_{ij} = \lambda\delta_{ij}\theta + 2\mu\epsilon_{ij} \tag{2.7}$$

where the equality $\theta = \delta_{ij}\epsilon_{ij} = \epsilon_{xx} + \epsilon_{yy} + \epsilon_{zz}$ is used. This sum is equal to the dilatation of the material, i.e. the volume change. In fact, the strain is linked to the components of the displacement $\mathbf{u}$ by the definition:

$$\epsilon_{ij} = \frac{1}{2}\left(\frac{\partial u_j}{\partial x_i} + \frac{\partial u_i}{\partial x_j}\right) \tag{2.8}$$

Substituting Eq. (2.7) and Eq. (2.8) into Eq. (2.4) returns the equation of motion for the displacement component i:

$$\rho\frac{\partial^2 u_i}{\partial t^2} = \mu\nabla^2 u_i + (\mu + \lambda)\frac{\partial\theta}{\partial x_i} \tag{2.9}$$

The Lamé parameters are considered constants. In its vector form, Eq. (2.9) becomes the well-known Navier equation [14]:

$$\rho\frac{\partial^2\vec{u}}{\partial t^2} = \mu\nabla^2\vec{u} + (\mu + \lambda)\nabla(\nabla\cdot\vec{u}) \tag{2.10}$$

This equation describes the propagation of elastic waves in a medium. In thermo-elasticity we have to consider the stress generated by the temperature gradient. From the previous section, we derived the components of the stress tensor generated by the temperature increment $\sigma_{ij}^{th} = -3B\beta\delta_{ij}\Delta T_L$. The Kronecker delta appears here because the thermal stress is equal in all directions. We include this term in the Navier equation as a source term [15]:

$$\rho\frac{\partial^2\vec{u}}{\partial t^2} = \mu\nabla^2\vec{u} + (\mu + \lambda)\nabla(\nabla\cdot\vec{u}) + \nabla\sigma^{th} \tag{2.11}$$

To solve this problem, it is easier to re-write this equation as a system of first-order coupled differential equations, after introducing the velocity components v_i and expanding Eq. (2.11)

$$v_x = \frac{\partial u_x}{\partial t} \quad , \tag{2.12a}$$

$$v_y = \frac{\partial u_y}{\partial t} \quad , \tag{2.12b}$$

$$\frac{\partial v_x}{\partial t} = -\frac{1}{\rho}\left(\frac{\partial \sigma_x^{re}}{\partial x} + \frac{\partial \sigma_{xy}^{re}}{\partial y} + \frac{\partial \sigma_x^{th}}{\partial x}\right) \quad , \tag{2.12c}$$

$$\frac{\partial v_y}{\partial t} = -\frac{1}{\rho}\left(\frac{\partial \sigma_y^{re}}{\partial y} + \frac{\partial \sigma_{xy}^{re}}{\partial x} + \frac{\partial \sigma_y{}^{th}}{\partial y}\right) \quad . \tag{2.12d}$$

in which we have defined the restoring forces as:

$$\sigma_x^{re} = -(\lambda+2\mu)s_x - \lambda s_y \;\; ; \;\; \sigma_y^{re} = -(\lambda+2\mu)s_y - \lambda s_x \;\; ; \;\; \sigma_{xy}^{re} = -\mu s_{xy} \tag{2.13}$$

The tensor s is related to the strain and therefore to the displacement according to:

$$s_x = \epsilon_{xx} = \frac{\partial u_x}{\partial x} \;\; ; \;\; s_y = \epsilon_{yy} = \frac{\partial u_y}{\partial y} \;\; ; \;\; s_{xy} = 2\epsilon_{xy} = \frac{\partial u_x}{\partial y} + \frac{\partial u_y}{\partial x} \tag{2.14}$$

Taking the time derivative of Eq. (2.14) is equivalent to:

$$\frac{\partial s_x}{\partial t} = \frac{\partial v_x}{\partial x} \;\; ; \;\; \frac{\partial s_y}{\partial t} = \frac{\partial v_y}{\partial y} \;\; ; \;\; \frac{\partial s_{xy}}{\partial t} = \frac{\partial v_x}{\partial y} + \frac{\partial v_y}{\partial x} \tag{2.15}$$

We can see that Eq. (2.12) and Eq. (2.15) are coupled through Eq. (2.13). This is in analogy to the Maxwell's equations where the E and B field are coupled through the time and spatial derivatives. This indicates that the system of equations Eq. (2.12) and Eq. (2.15) can be solved by the FDTD method [16], which was originally developed for solving the time-dependent Maxwell's equations [17].

We leave the introduction and the explanation of damping effects to Chapter 4, where they are necessary to explain the experimental results on gold free-standing membrane.

2.3.2. Polarization, Bulk, surface and Lamb waves

The vector form of the wave equation (Eq. 2.10) can be decoupled following the Helmholtz decomposition [18]. Accordingly, the displacement field can be written as

$$\vec{u} = \nabla\Phi + \nabla \times \vec{\Psi} \tag{2.16}$$

where Φ and $\vec{\Psi}$ are respectively a scalar potential and a vector potential. The potential $\vec{\Psi}$ needs to be divergence free. In this case the wave equation can be rewritten:

$$\nabla^2\Phi - \frac{1}{c_L}\frac{\partial^2\Phi}{\partial t^2} = 0, \tag{2.17a}$$

$$\nabla^2\vec{\Psi} - \frac{1}{c_S}\frac{\partial^2\vec{\Psi}}{\partial t^2} = 0 \quad . \tag{2.17b}$$

When applied to an unbound (infinite) medium the solutions to the Eq. (2.17) are *bulk* waves. These solutions are divided in longitudinal (or P-) waves and shear (or S-) waves. The longitudinal waves are solutions to Eq. (2.17a), while Eq. (2.17b) has two independent solutions known as shear waves. The difference between these waves is the direction of atomic displacement with respect to the direction of propagation of the wave. A longitudinal wave displaces the atoms in the same direction it propagates. Shear waves, instead, displace the atoms in two possible directions that are perpendicular to each other and to the direction in which they propagate.

The geometry of the experiment influences the type of waves that can be observed. In many photoacoustic experiments the pump beam is chosen to have transverse dimensions much bigger than the absorption depth of the sample [12, 19–21]. In these experimental conditions the propagation of the acoustic waves, inside the material, can be simplified to a 1-dimensional problem. The temperature gradient ΔT can be considered a function of only the depth, x, and the time, t, since the only component of the stress tensor different from zero is the one along the thickness direction σ_{xx} [22]. Assuming that the layer is isotropic, only longitudinal acoustic waves propagate along the thickness of the layer. Longitudinal bulk waves are of great use in thin film characterization due to the high frequencies at which they can be generated: up to hundreds of GHz for metals with high electron-phonon coupling constant, like aluminum.

Interfaces, or semi-infinite media, support solutions to the Helmholtz equations, Eq. (2.17) that propagate along the interface, or the surface of semi-infinite medium. These surface acoustic waves (SAWs) are waves that freely propagate along the surface of the material, while their displacement magnitude decays exponentially as a function of depth. SAWs are often called Rayleigh waves and the motion of the particles near the surface follows an elliptical trajectory. Also the SAWs are divided in longitudinal and shear waves according to the polarization of the wave. But, contrary to the bulk

waves, the phase velocity of a SAW depends on physical properties of the sample and on the frequency of the wave, in other words they are dispersive [18, 23]. In recent years, a strong effort has been dedicated to the study of the generation and control of the spectrum of SAWs. Using a focused pump beam [23, 24] on the surface of a metal generates broad-band SAWs. Transient grating or structured illumination are used, instead, for the generation of narrow-band SAWs [25].

As we mentioned, SAW's are confined near the surface. Their penetration depth is proportional to their wavelength. When the thickness of the layer is comparable to the wavelength of the SAW's, a new class of waves is generated: the Lamb waves [26]. These are actually guided modes and their dispersion curve strongly depends on the physical characteristics of the guiding structure: the thickness of the plate (or the film) and speed of sound of the material. In conventional ultrasound measurements, Lamb waves are used intensively because of their dispersion properties and high sensitivity to detect defects in the investigated sample [27, 28].

The confinement of the SAW in thin film is necessary for the generation of Lamb waves. However, bulk longitudinal waves can excite Lamb waves in thin film via a mode conversion mechanism. The mode conversion mechanism is illustrated in Figure 2.3(a). Part of the energy of a longitudinal wave incident at an interface is reflected as a shear wave. The opposite also happens, shear waves are partly reflected as longitudinal ones [29, 30]. In a free-standing layer multiple reflections occur because of the strong acoustic mismatch between the medium and air. The superposition of the generated P-waves and S-waves inside the medium causes the excitation of the Lamb waves (see Figure 2.3(b)) [26]. Mode conversion does not happen for normal incidence. Thus, to excite Lamb waves it is important that the acoustic wave wavevector has a component parallel to the surface. Fig. 2.3(d) shows how this condition is satisfied when we use a focused pump beam [31]. This effect occurs in our experiments on free standing layer and it is at the origin of a lateral propagation of strain components. As for the SAW's, transient gratings [5] are used to generate narrow band Lamb waves.

2.4. Detection

After the excitation of the metal via an ultrafast laser pulse its optical properties change. These changes can be measured in a pump-probe experiment

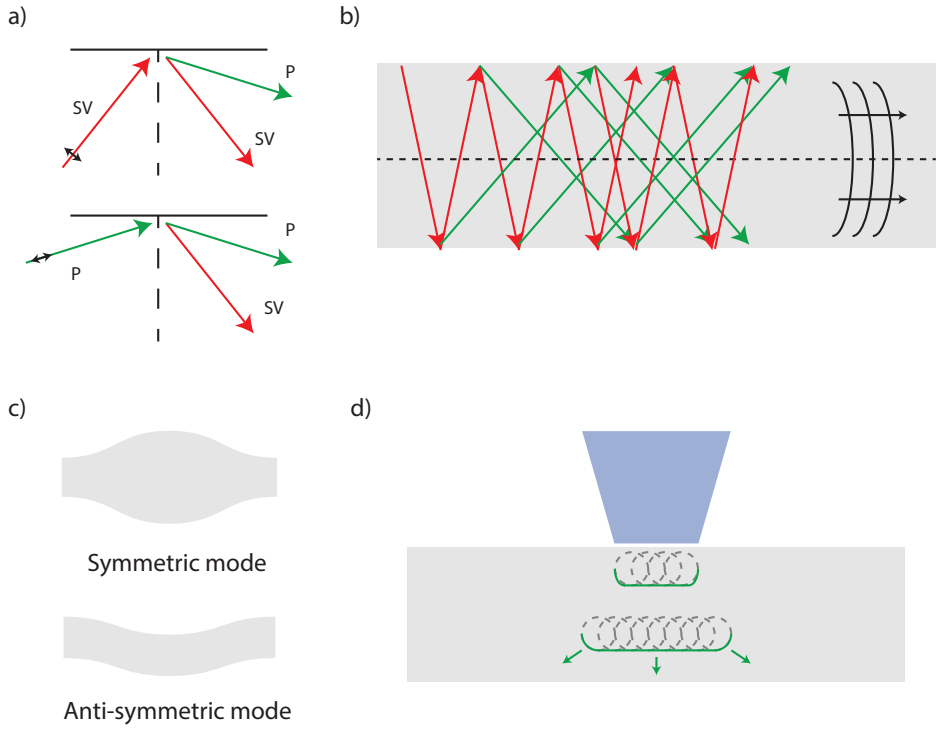

Figure 2.3: Lamb waves. a) The mode conversion occurs when a longitudinal (P) wave or shear vertical (SV) wave is incident on a free surface. One P-wave and one SV-wave bounce off the free surface. b) In an infinite plate where two free surfaces are parallel to each other, multiple mode conversions occur. The superposition of the P and SV waves generates guided modes known as Lamb waves. c) Lamb waves have infinite modes that can be categorized in symmetric and anti-symmetric with respect to the symmetry axis which divides the thickness of the plate. d) A way to generate Lamb waves is by using a focused pump beam on a free standing membrane. At the edge of the excitation region the k-vector of the acoustic waves has a non-zero component parallel to the surface. This is a condition for the generation of Lamb waves that propagate in the lateral direction away from the excitation area.

where the excitation pulse (the pump), is followed by another and less intense pulse (the probe). In a conventional pump-probe experiment we measure the reflectivity of the probe while scanning the time delay between pump and probe [32]. However, different configurations of pump-probe experiments can be implemented. For example, in a transient grating experiment two pump pulses are made to interfere at the sample surface. The excitation follows the periodic pattern of the pump and results in a transient grating [33–35]. We

can record the diffraction of the probe while scanning the delay to measure the decay of the transient grating.

In this last section of the chapter, we introduce the model that describes the changes of the optical properties as function of time. Whether we measure reflectivity or diffraction, from a modelling point of view we are in both cases interested in calculating the complex reflected field. In general, this field is affected by either the atomic displacement (which only influences the phase) or the local transient variation of the refractive index (which may influence both amplitude and phase) due to the presence of strain (strain-optic) or the temperature elevation (thermo-optic effect).

As we already discussed in the previous sections, the lattice temperature increases after the relaxation of the electrons. The thermoelastic effect causes a displacement of the surface. Furthermore, the temperature change induces a change in the refractive index according to the thermo-optic coefficient. The change of the complex refractive index as function of temperature is described by:

$$\Delta\tilde{n}_T(x,y,t) = \left(\frac{\partial n}{\partial T} + i\frac{\partial k}{\partial T}\right)\Delta T_L(x,y,t) \tag{2.18}$$

where $\frac{\partial n}{\partial T}$ and $\frac{\partial k}{\partial T}$ are respectively the real and the imaginary parts of the thermo-optic constants.

The changes induced by thermo-optic effects appear as a slowly decaying (or restoring, according to the sign of the thermo-optic constants) background in the signal of a photacoustic experiment. In contrast, faster changes in the photoacoustic signals results from to the strain carried by the acoustic waves, due to the photoelastic effect. The photoelastic effect can be described in a simplified tensor notation [12]:

$$\Delta\epsilon_i = P_{ij}s_j \tag{2.19}$$

where the indeces i and j can vary from 1 to 6 and indicate the tensor elements (1 = xx, 2=yy, 3=zz, 4=yz = zy, 5=zx = xz, 6 = xy = yx). $\Delta\epsilon$ is the change of the permittivity constant (ϵ is used as permittivity only in this section), P is the photoelastic tensor and s is the strain. We highlight the fact that the components of P are complex quantities. We can relate a change in the refractive index to a perturbation in the permittivity according:

$$\Delta\tilde{n}_s(x,y,t) = \left(\frac{\partial n}{\partial s_i} + i\frac{\partial k}{\partial s_i}\right) s_i(x,y,t) \tag{2.20}$$

where, $\frac{\partial n}{\partial s_i}$ and $\frac{\partial k}{\partial s_i}$ are the real and imaginary part of the strain optic coefficient and s_i is an element on the diagonal of the strain tensor.

Using the formulas for the refractive index changes it is possible to calculate the amplitude of the reflected field using a transfer matrix method or, if necessary, by numerically solving the Maxwell equations. The Maxwell equations are necessary when the problem includes structure of the surface with size comparable to the wavelength. In our experiments, we are not in this situation, and a transfer matrix is sufficient. Even in the transient grating experiments, where the grating period is much larger than the probe wavelength, we treat each point of the surface independently. Then we approximate the solution of the 2D problem with the combination of the independent 1D solutions. It is important to highlight that of the experiments presented in this thesis only the transient grating show a contribution from the surface displacement. This contribution is included in the 2D model assuming the "shallow grating approximation" for small displacement of the surface. The assumption allows to include the displacement in the calculation of the complex electric field:

$$\tilde{E}_p(y,t) = \tilde{E}_{p\delta\overline{n}}(y,t)e^{i\frac{4\pi n}{\lambda}u_{xx}}, \tag{2.21}$$

where $\tilde{E}_p$ is the total diffracted field, $\tilde{E}_{p\delta\overline{n}}$ the complex field diffracted by the perturbed refractive index that is obtained with the transfer matrix method and u_{xx} is the surface displacement.

2.5. Conclusion

The ability to calculate the reflectivity or the diffraction of the probe light in a pump-probe experiment as function of delay time is of critical importance for our study. In this chapter we have introduced the physical mechanisms underlying the generation, propagation and detection of the acoustic wave. The physical insights are presented together with the equations used to describe mathematically a photoacousitc experiment. These equations are solved using an FDTD scheme.

Despite of the complexity of the numerical model, it is still possible to use

it to run fitting routines on the experimental data, to obtain important parameters such as the thermo- and strain-optic coefficients. In the following part of the thesis, we present our experimental work.

The description of the complete model with the addition of damping and dispersion effects will be given in Chapter 4, together with the experimental work with which we could observe these effects.

3

Ultrafast electron dynamics in single and multi-layers structures

This chapter has been published as part of Opt. Express **26**, 23380-23396 (2018) [36]

3.1. Introduction

Many scientific fields benefit from the investigation of ultrafast dynamics in metals [6, 12, 37–43]. The processes following the illumination by an ultrafast pulse have been studied intensively, improving the understanding of the electron dynamics within a metal layer of few nanometer-scale thickness [7, 8, 44–60]. In this type of ultrafast laser-matter interaction, the first process that occurs is the partial absorption of the incident pulse energy by electrons in the metal. The depth range over which this occurs is given by the skin depth, which is typically a few tens of nm. After absorption of the pulse energy, the electrons are in a non-thermal equilibrium which evolves towards a Fermi-Dirac distribution via electron-electron collisions. Within this time, which usually is a few hundreds of femtoseconds [34, 61–64], the high-energy electrons undergo both ballistic and diffusive motion which contribute to the thermalization of the electron system. The electrons thermalize at temperatures of typically several thousand Kelvin, and will cool down by heating the lattice, a process that typically takes a few picoseconds.

Even though the literature contains a large number of studies on ultrafast optical excitation of single metal layers, only few experimental studies of metallic bilayers can be found. The composition of the sample is expected to influence not only how the electron dynamics occurs in the top layer [54–56, 65–67] but also where in a more complex sample the lattice temperature increases [68, 69]. As we have seen in the previous chapter the location and the extension of the lattice heat depends on the electron-phonon coupling constant. For example, when the electron-phonon coupling constant is low the heat is homogeneously distributed along the thickness of the sample, as in the case of gold.

In this chapter, we show the results of our study on the electron dynamics on gold in single layer and in bilayer systems where a metal with different electron-phonon coupling constants is used under the gold layer. In our pump-probe experiments, we we pump the sample using a light-induced grating [33] and we measure the transient probe diffraction. The experimental results are compared to the results of a two temperature model which allowed us to gain insights on the heat distribution after the relaxation of the electron gas.

3.2. Experimental setup

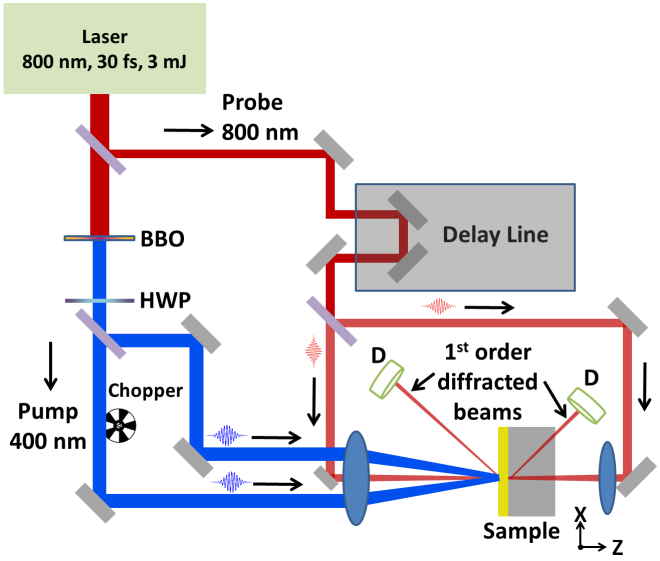

Figure 3.1: Schematic of the experimental setup: components include a non-linear optical crystal (BBO), Half Wave Plate (HWP) and a Photodiode (D). The two frequency-doubled 400 nm pump pulses are focused onto the sample at the same position, but under different angles to form a spatially periodic intensity pattern. The 800 nm probe pulse that diffracts off the resulting grating in the optical constants of the sample, is recorded by the detectors while the delay line is used to change the pump-probe delay.

A schematic of the experimental setup used for our experiments is shown in Figure 3.1. The laser system used is a Ti:Sapphire multi-pass amplifier (Femtopower, Spectra Physics) generating 30 fs pulses, with a wavelength centered at 800 nm and with a repetition rate of 1 kHz. The output from the laser is split into two using a 1% beam splitter. The stronger part is frequency doubled with a 100 µm BBO crystal to generate 400 nm pump pulses. A half wave plate (HWP) rotates the polarization of the 400 nm pump pulse by 90^o so that both the pump and the probe are p-polarized. For experiments on flat samples, the pump pulses are split into two by a 50% beamsplitter. One part passes through a 500 Hz mechanical chopper. Both beams are then weakly focused onto the sample at a different angle. On the sample, the two pump pulses overlap in space and time to create a spatially periodic interference pattern with a period determined by the angle between the beams. In our experiments, we have a grating period of 6 µm. The spatially periodic excitation of the metal leads to spatially periodic changes in the optical constants of the metal, that can be observed

by diffracting a delayed probe pulse off the transient grating. By measuring the diffracted signal as a function of the pump-probe delay, we can measure the decay of this transient grating, giving information on the electron dynamics. Using different wavelengths for pump and probe allows us to use optical filters to block scattered pump light from entering the probe detector. The diffracted pulse energy is recorded by a silicon photodiode placed at the position where we expect the first-order diffracted beam. The analog signal recorded from the photodiode is converted to a digital signal and averaged over 100 pulses. The diffracted probe signal recorded by the detector when the chopper blocks the pump beam is subtracted from the diffracted probe signal when the pump beam is transmitted by the chopper and plotted as a function of the pump-probe delay. The signal recorded by the detector in the absence of the pump pulse is from probe light scattered by the surface roughness of the sample. Depending on the experiment, we probe from the front surface or from the back surface. In the latter case, the probe pulse passes through the glass substrate and probes the metal near the glass-metal interface. The pump beam has a spot size of 1.5 mm on the sample and the pump pulse energy ranges from 3 µJ to 15 µJ depending on the experiment. The probe pulse energy was kept constant at 1 µJ. This is a significant fraction of the pump-pulse energy to maximize the possibility of detecting signals on samples demonstrating a low diffraction efficiency. However, in our experiments we mostly pump and probe Au in which about 60% of the 400 nm wavelength pump-pulse energy is absorbed and only about 2% of the 800 nm wavelength probe-pulse energy. No two-photon probe absorption was observed within the measurement accuracy of our setup. The typical diffraction efficiencies, recorded when the pump and probe overlap, range from 10^{-5} to 10^{-4}, depending on the pump pulse energy and the sample thickness. For the experiments on the physically buried metal grating, only *one* pump beam is used.

All samples used in the experiments are prepared by physical vapor deposition at a pressure below 10^{-6} mbar on a chemically cleaned glass substrate. The film thickness was determined using a quartz crystal thickness monitor with a $\pm$ 5% uncertainty. For experiments on bilayer thin films, the materials were evaporated one after the other without disturbing the vacuum of the evaporator. The metal gratings on the flat layer of gold were fabricated by UV lithography.

3.3. Numerical calculations

3.3.1. Pulse energy absorption

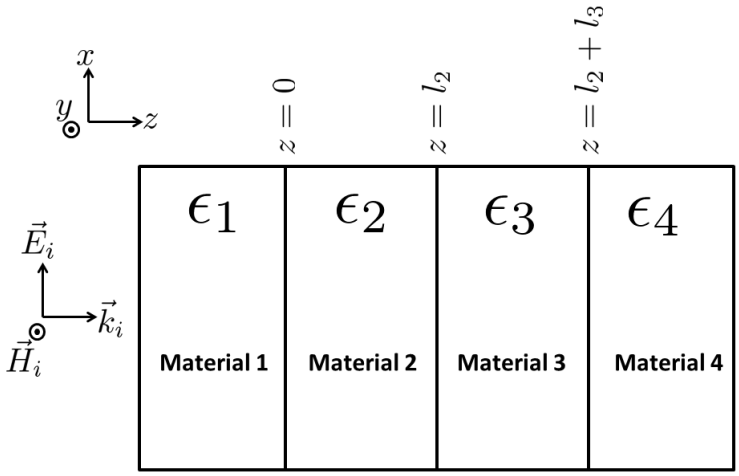

Figure 3.2: Geometry used for the calculation: Material 1 and 4 have an infinite extent to the left and right side respectively. Material 2 and 3 have a finite thickness of l_2 and l_3 respectively. The electromagnetic wave originating from material 1 propagates through all four materials after undergoing partial reflection and transmission at each interface.

For a proper understanding of our experiments on flat bilayer samples, it is important to calculate where the optical energy is deposited inside the material. To do so, we first solve the Maxwell's equations for an electromagnetic field in four different materials (see Figure 3.2) and then we multiply the result with a Gaussian envelope in time, which corresponds to the pulse temporal profile. This resembles the experiment in which, air, the first metal, the second metal and the substrate are the four different materials through which the laser pulse propagates. In a multilayer structure, it is important to calculate the intensity of the light directly hitting the second metal layer because this will also affect the electron-lattice dynamics at the surface of the first metal layer. In the calculation, we consider material 1 and 4 to be infinitely thick while materials 2 and 3 have a finite thickness. The first material represents air and material 4 represents glass. Material 2 and material 3 are the Au and Pt metal (or other metals used in the experiment) layers respectively. From the basic electromagnetic equations, we can understand that a wave incident on the interface between material 1 and material 2

will undergo partial reflection into the first material and partial transmission into the second material. The partially transmitted wave undergoes further partial reflection and transmission at the interface between material 2 and 3 and, material 3 and 4 . To calculate the spatial distribution of absorption in material 2 and material 3, we need to obtain the complete electric and magnetic field expressions describing the magnitude and direction of the fields. We assume that all fields propagate perpendicular to the interfaces.

Due to the non-magnetic nature of gold and platinum we can safely assume $\mu = \mu_0$ for all materials. In absence of any charged particles or currents, we can write the electric and magnetic fields inside each material as

$$\vec{E}(z,t) = E_0(t) \begin{cases} (e^{ik_1 z} + re^{-ik_1 z})\hat{x}, & z < 0 \\ (ae^{ik_2 z} + be^{-ik_2 z})\hat{x}, & 0 < z < l_2 \\ (ce^{ik_3(z-l_2)} + de^{-ik_3(z-l_2)})\hat{x}, & l_2 < z < (l_2 + l_3) \\ t(e^{ik_4(z-(l_2+l_3))})\hat{x}, & z > (l_2 + l_3) \end{cases} \tag{3.1}$$

$$\vec{H}(z,t) = \frac{E_0(t)}{\omega\mu} \begin{cases} k_1(e^{ik_1 z} - re^{-ik_1 z})\hat{y}, & z < 0 \\ k_2(ae^{ik_2 z} - be^{-ik_2 z})\hat{y}, & 0 < z < l_2 \\ k_3(ce^{ik_3(z-l_2)} - de^{-ik_3(z-l_2)})\hat{y}, & l_2 < z < (l_2 + l_3) \\ k_4(te^{ik_4(z-(l_2+l_3))})\hat{y}, & z > (l_2 + l_3) \end{cases} \tag{3.2}$$

where *a, b, c, d, t, r*, k_1 and k_4 are assumed to be real and $k_2 =$ and k_3 are complex. Here $k_2 = \omega\tilde{n}_2/c$ and $k_3 = \omega\tilde{n}_3/c$ with $\tilde{n}_{2,3} = n_{2,3} + i\kappa_{2,3}$ being the complex refractive index of material 2 and 3 respectively. The pulsed excitation is incorporated by our choice of electric field,

$$E_0(z,t) = Ae^{-4ln2(t/\tau_p)^2)} \times e^{(-i\omega t)},$$

where τ_p is the full width at half maximum pulse duration of the electric field envelope and A is the amplitude of the electric field.

We use the boundary condition that both the electric and magnetic field components parallel to the interface are continuous across each interface and solve the resulting set of equations to obtain expressions for *a, b, c, d, t* and *r*. This allows us to write the expression for the space and time-dependent fields in all four materials. From these we calculate the single oscillation time average of the Poynting vector, $\langle\vec{S}\rangle$. From $\langle\vec{S}\rangle$, the optical power absorbed per unit volume is expressed as,

$$\frac{\partial u}{\partial t} = -\vec{\nabla} \cdot \langle \vec{S} \rangle, \tag{3.3}$$

where u is the electromagnetic energy density. Knowing the distribution of the optical intensity inside all four materials, we use the refractive index n and extinction coefficient κ values of gold and platinum to calculate the optical intensity distribution inside the bilayer [68]. The result of this calculation is used as source in the two temperature model.

3.3.2. Two temperatures model

The two temperature model is a widely used phenomenological model that describes the electron-lattice dynamics after optical excitation with a laser pulse. In the model, the electron gas is assumed to be thermalized at all times during and after excitation with, and is described by a time-dependent temperature T_e, while the lattice is assumed to have a time-dependent temperature T_l. The time evolution of the temperature is modeled by two coupled differential equations, originally proposed by Anisimov et al. [70] and can, assuming a one-dimensional geometry, be written as [71],

$$C_e(T_e)\frac{\partial T_e}{\partial t} = \frac{\partial}{\partial z}\left(K_e \frac{\partial}{\partial z} T_e\right) - g(T_e - T_l) + \frac{\partial u}{\partial t} \tag{3.4}$$

$$C_l \frac{\partial T_l}{\partial t} = g(T_e - T_l). \tag{3.5}$$

Here, C_e and C_l are the respective heat capacities of the electron gas and the lattice, K_e is the thermal conductivity of the electron gas, g is the electron-phonon coupling constant and $\partial u/\partial t$ is the source term. The source term describes when and where energy is deposited in the system by the laser pulse. Note that in Eq. (3.4), the lattice heat diffusion can be neglected since this is typically slow on the time scales of our experiment. The relations $C_e = A_e T_e$ and $K_e = K_0 \times T_e/T_l$ [71] together with the TTM allow us to numerically calculate the time evolution of T_e and T_l, using the actual experimental parameters and using material properties obtained from literature and shown in Table 3.1. We highlight the fact that by assuming instantaneous local thermalization of the electron gas we ignore ballistic transport of the electrons. The ballistic transport is known to occur in gold in the first $\approx$ 100 fs [48].

As we will show in the following sections, we find a remarkable correspondence between the measured, time-dependent, diffracted signal, and the cal-

Table 3.1: Material constants used in our two temperature model calculations. Listed are the electron-phonon coupling constant g, electron specific heat constant A_e, thermal conductivity K_0 at $T = 273$ K and lattice heat capacity C_l. [11, 71–73]. We have used the relations $C_e = A_e T_e$ and $K_e = K_0 \times T_e/T_l$ [71].

Metals	g (10^{16} $Wm^{-3}K^{-1}$)	A_e ($Jm^{-3}K^{-2}$)	K_0 ($Wm^{-1}K^{-1}$)	C_l (10^5 $Jm^{-3}K^{-1}$)
Gold	1.6	71	318	24.3
Platinum	100	740	73	27.0
Copper	8.0	98	401	35.0
Silver	1.9	63	428	25.0

culated time-dependent electron temperature. However we point out that, there is no a priori reason to assume that the diffraction efficiency η should linearly depend on the change in the electron temperature ΔT_e. Being $\Delta\epsilon$ the change in the complex dielectric function [33], it can be shown that the diffraction efficiency η scales as $\eta \propto (\Delta\epsilon)^2$. From the assumption that the dielectric function changes because of the changes in the electron gas temperature ΔT_e, we conclude that this linear relation must imply $\Delta\epsilon \propto \sqrt{\Delta T_e}$. In contrast with the often made assumption that $\Delta\epsilon \propto \Delta T_e$ [56, 60, 64] or $\Delta\epsilon \propto \Delta(T_e)^2$ [57, 74]. We currently do not know what the origin is of the different temperature dependencies of the dielectric function extracted from the experiments. A full theoretical analysis of the time-dependent complex dielectric function after optical excitation requires detailed calculations of the contribution of inter- and intraband transitions to the changes in the complex dielectric function. Hohlfeld et. al. [49] showed that this can give satisfactory results, but such an effort is beyond the scope of this chapter. It is interesting, though, that our calculations of the electron temperature use only material parameters known from the literature. Only the electron-phonon coupling constant of gold is on the low side of the range of values found in the literature. Using experimental values for the excitation parameter, we make no use of adjustable parameter in our model. The calculations of the time-dependent electron temperature are placed alongside some of the measurements to provide important physical insight into the electron and lattice dynamics occurring after excitation.

3.4. Results and discussion

We performed pump-probe experiments with interfering pump pulses forming a spatially periodic, grating-like excitation pattern, on single layers of gold (section 3.4.1) and gold-metal bilayers (section 3.4.2 and 3.4.3). This was done to obtain a better understanding of the electron dynamics and, in a few cases, to compare with results known from literature.

3.4.1. Electron dynamics in gold

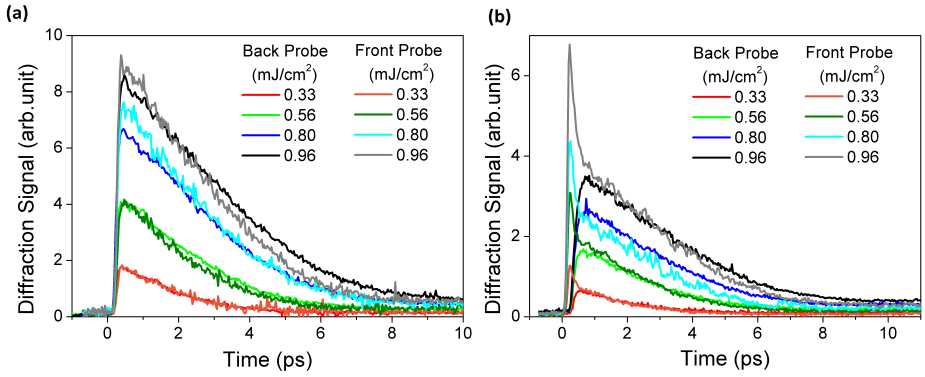

Figure 3.3: Diffracted front-probe and back-probe signal as a function of pump-probe delay at various pump fluences for (a) 45 nm gold layer and (b) 100 nm gold layer. The samples were pumped from the air-gold side and probed from the air-Au side (front probe) and the glass-Au side (back probe).

In Figure 3.3, we plot the probe signal diffracted from both the air-Au interface (front) and the glass-Au interface (back), for two different thicknesses of Au, 45 nm in Figure 3.3(a) and 100 nm in Figure 3.3(b), for various pump powers. In all cases, the 400 nm pump beams illuminate the Au from the front-side. As it is difficult to compare the absolute diffraction efficiencies for the front and back-probe cases, we applied a scaling factor to the back-probe signal such, that for a single pump intensity, both the front-probe signal and the back-probe signal overlap as much as possible for time delays larger than 0.5 ps. We then use the *same* scaling factor for the curves at different intensities. Different scaling factors were used for the 45 nm Au and 100 nm Au back probe signals and the signal strengths shown in Figure 3.3(a) cannot be compared with those in Figure 3.3(b). In both figures, the front probe diffraction efficiency is seen to rise on a rapid time scale of $\approx$ 100 fs. For the 45 nm sample in Figure 3.3(a)„ this then gradually decays towards zero for

increasing time delays. For the 100 nm sample in Figure 3.3(b), the decay is initially rapid, and then slows down. In both measurements, excitation with two spatially and temporally overlapping pump pulses results in a spatially periodic electron gas temperature $T_e(x,t)$ along the surface, in a direction perpendicular to the grating lines. This temperature grating is formed when in the bright fringes of the interference pattern the electron gas is rapidly heated whereas in the dark fringes, where the electron gas is not excited, the temperature remains 297 K. The amplitude of this electron-gas temperature grating, $\Delta T_e(t)$, is thus determined by the difference between the temperatures in the bright and the dark fringes. Heating of the electron gas leads to changes in the complex dielectric function of the metal. A grating in the electron-gas temperature thus leads to a grating in the dielectric function. From this grating, a probe pulse can be diffracted. As such, the diffracted signals observed in Figure 3.3 are correlated with the dynamics of $\Delta T_e(t)$. The rapid decay, observed during the first 0.5 ps for the 100 nm thick sample, was not observed by Hohlfeld et. al. [48], presumably because they used longer pulses in their experiments which may have given rise to a smearing out of the sharp peak. Interestingly, the results show that for the 45 nm gold film the signal shapes for the front and back-probe signals are very similar. This observation agrees with the assumption that for thin layers, after optical excitation, the electron energy is quickly redistributed relatively homogeneously throughout the layer [48]. This redistribution causes the measured dynamics, now dominated by electron cooling through lattice heating, to be the same everywhere. However, for the 100 nm gold layer, the front- and back-probe signals are different. There, we find that the front probe signal shows a rapid rise and decay, but that the back-probe signal rises more slowly. For pump-probe time delays larger than about 0.5 ps, the signals look similar and, again only one vertical scaling factor is applied to the back-probe signals to overlap all the front- and back-probe signals for this sample. The sharp rise/fall time of the front-probe signal and the slower rise of the back-probe signal are the result of ballistic transport and diffusion of electron energy out of the front-surface front-probe interaction region towards and into the back-probe interaction region near the Au/glass interface [48]. For 100 nm Au this process takes a few hundred femtoseconds which explains the slower rise of the back-probe diffracted signal. This also means that after this time the electron energy distribution should be relatively homogeneous again, explaining why for delays larger than about 0.5 ps the front-and back-probe signals look similar.

3.4.2. Electron dynamics in gold-platinum bilayers

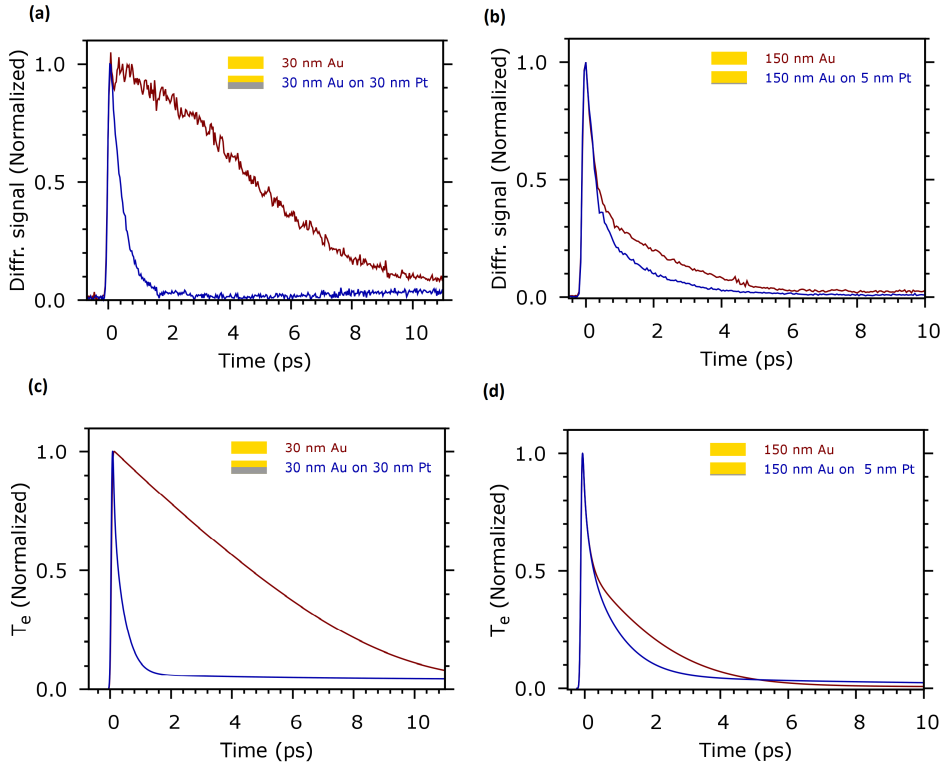

Figure 3.4: (a) The measured front-probe diffracted signal vs. pump-probe delay for a pump fluence of 0.80 mJ/cm^2 on a sample with 30 nm Pt under 30 nm Au. (b) The experimentally measured front-probe diffracted signal vs. pump-probe delay on a sample with 5 nm Pt under 150 nm Au. (c) The numerically calculated electron temperature T_e vs. time for the sample with 30 nm Pt under 30 nm Au. (d) The numerically calculated T_e vs. time for the sample with 5 nm Pt under 150 nm Au.

To better understand the measurements on buried gratings discussed later in this paper, we also studied the effect that a buried metal layer has on the electron dynamics observed at the gold surface. Initially, we chose platinum as the buried metal layer due to its very high electron-phonon coupling strength when compared to gold. In Figure 3.4(a) we plot the measured diffracted front-probe diffraction efficiency versus pump-probe time delay for a bilayer consisting of 30 nm of Au deposited on 30 nm of Pt. In the same figure, we also plot the time-dependent front-probe diffraction efficiency for a single 30 nm thick layer of Au. The figure shows that the presence of the Pt layer underneath the gold dramatically accelerates the decay of the diffracted

probe signal. Note that, although no signal for a Au thickness of 60 nm was measured, the results shown in Figure 3.3 for 45 and 100 nm thick single Au layers suggest that for 60 nm of gold, the decay would be in between these two cases and would still be significantly slower than for 30 nm of Au on Pt. To determine the limits of the effect that Pt has on the decay of the measured diffracted signal, we plot in Figure 3.4(b) the front-probe diffraction efficiency versus pump-probe delay for a sample consisting of 150 nm of Au on 5 nm of Pt and for a sample consisting of 150 nm Au only. This gold layer thickness was chosen to eliminate the possibility of the 400 nm pump beam directly exciting the Pt since the 400 nm light has a penetration depth of about 16 nm in Au. Remarkably, the results show that for this particular bilayer, even the effect of a buried Pt layer as thin as 5 nm on the shape of the diffracted signal versus pump-probe delay, is still measurable. The tell-tale sign of the effect of the buried Pt layer is that the transition from an initial fast decay to a slower decay, as observed in the gold-only sample, is absent. This means that the difference between the single Au layer and the bilayer manifests itself most strongly for longer time delays, as shown in Figure 3.4(b).

This difference in decay due to the presence of a platinum layer can be simulated using TTM calculations. In Figure 3.4(c) and Figure 3.4(d), we plot the calculated electron temperature at a depth of 8 nm from the top surface of the gold layer as a function of time, using the same parameters as in the experiments. For the sample with 30 nm Au on top of 30 nm Pt, the electron temperature decreases rapidly due to the presence of the platinum layer. For the sample with 5 nm Pt under 150 nm Au, the electron temperature decreases at a slightly slower rate than in 150 nm Au. We note that the calculation of the time-dependent electron temperature closely resembles the measurements of the diffraction efficiency versus pump-probe time delay.

We can explain this behavior by looking at the electron-lattice dynamics occurring in the buried platinum layer. After optical excitation, the electron energy diffuses deeper into the gold layer and beyond into the platinum layer. The electron-phonon coupling constant of platinum, however, is about two orders of magnitude higher than that of gold. This means that thermalized electrons that diffuse into the platinum, immediately lose energy to the Pt lattice and quickly cool. Thus, a strong electron-temperature gradient between the gold and platinum layer is maintained, which in turn drives the rate of electron gas energy diffusion out of the probe interaction region near the surface of gold into the deeper regions of the gold and into the platinum layer. These results are interesting, because they show that even a Pt layer

as thin as 5 nm has a measurable effect on the decay observed near the surface of a 150 nm thick Au layer. This suggests that a pump-probe technique may be used for sub-surface metrology, in particular the localization and inspection of buried structures underneath optically opaque metal layers.

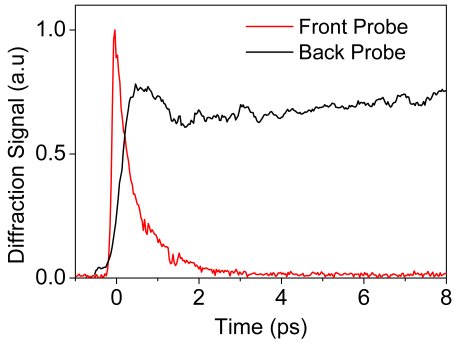

Figure 3.5: The measured diffracted signal from the front-probe (red) and back-probe (black) for a pump fluence of 0.80 mJ/cm^2 on a sample with 30 nm Pt under 30 nm Au.

To confirm that the energy is deposited in the Pt layer, we performed experiments on a sample with 30 nm platinum on 30 nm gold in which we pump from the gold side and probe from the platinum side (back probe) as well as the gold side (front probe). In Figure 3.5, we plot the diffracted front-probe and back-probe signal as a function of the pump-probe delay. As it is difficult to compare the absolute diffraction efficiencies for the front and back-probe cases, we instead applied a scaling factor to the back-probe signal so that both the front-probe signal and the back-probe signal can be plotted in the same graph. The back probe signal was smoothed by nearest neighbor averaging. For the front probe, the signal rises rapidly and then decays in 1-2 ps, indicating a rapid drop in electron temperature. This plot is similar to Figure 3.4(a) and the physics has been discussed earlier in this section. In contrast, the signal from the back probe shows a gradual increase for about 0.7 ps followed by a small decrease to a lower value and then continues to increase very slightly.

This different behavior of the back probe signal vs. pump-probe time delay can be explained by including the lattice dynamics of the Pt-Au layer. The initial rise of the back-probe signal seen in Figure 3.5 is interpreted as resulting from the diffusion of electron energy into the Pt layer and simultaneous

heating of the Pt lattice by the electron gas. The small decay is the result of the cooling of the electron gas, but it is superimposed on the growing signal caused by the heating of the lattice. The slow and weak increase of the signal after 2 ps is real. The TTM calculations (not shown here) indicate that, at a time delay of about 1 ps, the Pt lattice temperature has a strong gradient, being higher near the Pt/Au interface and lower near the back of the Pt, where the probe pulse interacts with the Pt. Equilibration of the difference occurs through electron energy diffusion, where electrons pick up the lattice energy from the hotter regions, and deposit this in the cooler regions. The latter gives rise to a slowly increasing lattice temperature in the regions where the probe pulse interacts with the Pt and thus an increasing diffraction signal. Our measurements are consistent with observations made in the context of ultra-high frequency sound-wave generation by indirect heating of Ti underneath Cu on a Cu-Ti bilayer, where indirect heating of a Ti layer underneath a Cu layer was shown to generate ultra-high frequency sound-wave packets [12].

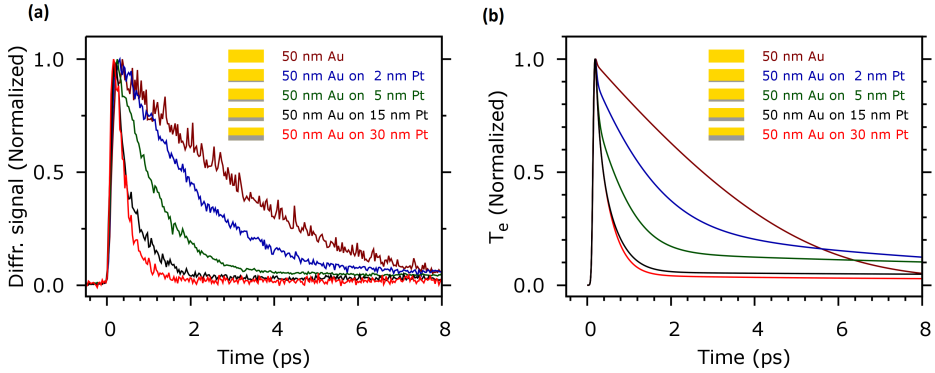

Figure 3.6: (a) The measured front-probe diffracted signal vs. pump-probe delay for a pump fluence of 0.96 mJ/cm^2 on bilayer samples with different thicknesses of platinum (0, 2, 5, 15, 30 nm) buried under 50 nm gold, (b) The numerically calculated electron temperature T_e vs. time for these samples using the same pump fluence as used in the experiment.

To more systematically study the effect of the thickness of the Pt layer on the probe-diffraction decay curves, we fabricated samples in which we kept the Au layer thickness fixed while varying the Pt layer thickness. In Figure 3.6(a), we plot the measured front-probe diffraction signal as a function of pump-probe delay from bilayer samples having a buried Pt layer thickness of 0, 2, 5, 15, and 30 nm underneath a 50 nm layer of Au. The pump fluence

in these experiments is 0.96 mJ/cm^2. The results clearly show that thicker Pt layers lead to a more rapid decay of the probe diffraction efficiency versus pump-probe time delay. Remarkably, even a Pt layer as thin as 2 nm is capable of speeding up the measured decay significantly.

In Figure 3.6(b), we plot the calculated electron temperature at a depth of 8 nm from the top surface of gold as a function of time for these samples. In the simulation, the same parameters were used as in the experiment. The calculations show that the electron temperature decays faster for samples with a thicker layer of platinum buried underneath and are in good agreement with the experimental results. However, the constant level to which the curves decay, seen in the calculation, is somewhat higher compared to what is observed in the experiments.

We can intuitively understand this behavior as a thicker layer of platinum acts as a more effective electron energy heat sink. This results in a higher rate of diffusion of electron energy out of the optical probe interaction region near the Au surface, and a subsequently more rapid drop in electron temperature. This measurement thus shows that some measure of control of the rate of diffusion of electron gas energy between the two metal layers is possible by varying the buried metal thickness. In fact, changing the thickness of the buried platinum also affects the maximum Pt lattice temperature reached, after optical excitation.

3.4.3. Electron dynamics in bilayers with other metals

To confirm that it is the strength of the electron-phonon coupling constant that is responsible for the increase in the observed probe diffraction decay rate, we also fabricated bilayers in which we varied the type of metal underneath the gold layer. In Figure 3.7(a) we plot the front-probe diffracted signal as a function of pump-probe time-delay, for bilayers consisting of 50 nm of Au on top of 30 nm of four different metals, being: Pt, Cu, Ag and Au, (the last case thus consisting of 80 nm of Au in total). For completeness, we also show the results for a 50 nm single layer of gold. The pump fluence in these measurements was 0.80 mJ/cm^2.

The Figure 3.7(a) shows that the decay of the diffraction efficiency versus time for 50 nm of Au on Pt, also shown in Figure 3.6(a), is the fastest, followed by Au on Cu, which is also faster than 50 nm + 30 nm of Au only,

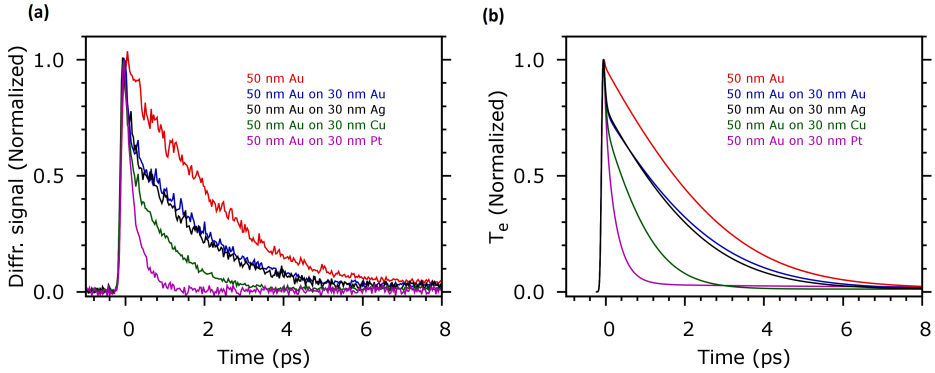

Figure 3.7: (a) The measured front-probe diffracted signal vs. time for a pump fluence 0.80 mJ/cm^2 for bilayer samples with different materials buried under 50 nm Au. (b) The numerically calculated electron temperature T_e vs. time for the same pump fluence as used in the experiments.

but slower than the signal for Au on Pt. The decay for 50 nm Au on 30 nm Ag is about as fast as that for 50 nm Au + 30 nm Au.

In Figure 3.7(b), we plot the calculated electron temperature at a depth of 8 nm from the surface of Au as a function of time for these samples. The decay of the electron temperature is fastest for the sample with a buried layer of platinum. The decay gets slower as the buried layer is changed from platinum to copper to silver and finally to gold. This is in good agreement with the experimental results. The decay of the measured diffracted signal correlates with the strength of the electron-phonon coupling in the various metals listed in Table 3.1, with materials having a stronger electron-phonon coupling showing a faster decay. The electron-phonon coupling constants of Ag and Au are more or less the same and so are the measured decay rates.

3.5. Conclusion

We have shown pump-probe diffraction measurements of the thermalized electron gas dynamics in single metal layers and in metallic bilayers. Our measurements on Pt/Au samples show a rapid decay in the measured diffracted probe signal, after optical excitation with a pump pulse, indicating a rapid cooling of the electron gas at the gold surface due to the presence of the buried platinum layer. We find that this decay increases with increasing Pt layer thickness. Even for a sample with 5 nm Pt under 150 nm Au, we

observe a measurable effect on the shape of the time-dependent diffracted signal as compared to 150 nm Au only, illustrating the sensitivity of electron diffusion near the gold surface on the presence of a buried layer such as Pt. The decay of the diffracted signal is also found to be dependent on the type of buried metal layer and is correlated with the electron-phonon coupling strength of the buried metal. The TTM numerical calculation of the electron temperatures shows good agreement with our measurements. The experiments show a correlation between the diffraction signal after optical excitation and the lattice temperature dynamics. In the original paper [36], we have also demonstrated the use of the electrodynamics sensitivity to detect buried interfaces optically hidden by opaque layer.

4

Unraveling Phononic, Optoacoustic, and Mechanical Properties of Metals with Light-Driven Hypersound

In this chapter we present the results of transient grating experiments on metal layers. With these measurements we observe the effects of the induced dynamics at almost ≈1 ns after excitation of the metals. We compare the experiments with the numerical calculation, which capture all the aspect related to the propagation of ultrasound waves in a metal. Finally, fitting the model to the observed data we can retrieve important material properties.

This chapter has been published in Phys. Rev. Applied 13, 014010 (2020) [5].

4.1. Introduction

A thorough understanding of the electron-phonon, thermo-optic and acoustic properties of materials is of paramount importance for many applications in materials science and advanced applications adopting laser-induced sound waves. While ultrasound experiments have enabled measurements of sample geometry, the quantitative retrieval of bulk material properties in such experiments has remained an open challenge. Various results on model-based analysis of experimental measurements have been reported [29, 32, 34, 75–83], which yielded remarkable results about the acoustic wave generation mechanism itself. Nevertheless, most of the models are based on a one-dimensional description of the acoustic wave propagation and only incorporate a rather limited description of the various physical effects in laser-induced ultrasound. Due to this incompleteness in the existing models, to the best of our knowledge a rigorous, quantitative analysis of the experimental results through direct model fitting has not yet been achieved. Such a quantitative analysis is challenging yet demanding as it requires a comprehensive and yet accurate modelling of the complex interplay between all the different physical effects involved in the generation, propagation and detection of the ultrasound pulses, which occurs over timescales that span orders of magnitude. The detected signal is a coherent addition of signals resulting from atomic displacements, strain- and thermo-optic effects, and possibly multilayer interference effects such as Brillouin scattering, and these signals in turn result from a combination of electronic and thermal effects, surface and longitudinal acoustic waves, possibly including multiple reflections from sub-surface interfaces. To disentangle all these different possible contributions and elucidate their respective roles in the signal formation, a full theoretical treatment should accompany the experiments. Fitting the experimental results to the output of such a model then enables a detailed analysis of the different physical effects involved, but also allow the retrieval of fundamental material properties such as electron-phonon coupling strengths, acoustic parameters, as well as acousto-optic and thermo-optic couplings [34, 82]. In addition, models based on a 1D wave equation [32, 34, 79–81, 83, 84], do not capture dynamics of surface acoustic waves (SAWs) and diffraction. These effects become important especially for nanoscale materials [85, 86] and structured or small excitation volumes [29, 34, 83, 87]. To include phenomena such SAWs and acoustic diffraction, a two-dimensional model is a minimum requirement. Furthermore, acoustic damping is an important but complex phenomenon at ultrasound frequencies, as picosecond-timescale phonon dynamics can significantly influence microscopic viscosity and strain [88–91]. Yet, these effects

are usually not being considered.

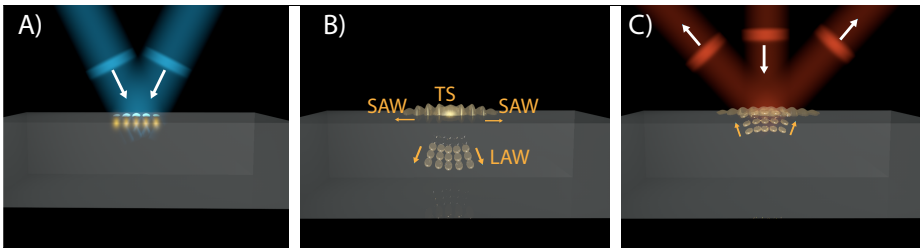

Figure 4.1: Schematic of laser-induced ultrasound in a transient grating configuration. A) Two ultrafast pulses interfere at the sample surface, heat the electrons in a thin layer at the surface of an opaque medium (here shown partially transparent for viewing purposes). B) The electron energy is transferred to the lattice, resulting in ultrahigh-frequency acoustic phonons that travel into the sample as longitudnal acoustic waves (LAWs) or along the surface as surface acoustic waves (SAWs). A local temperature increase at the surface also results in thermal stress (TS). C) The returning LAWs, as well as the SAWs and TS lead to surface displacement and refractive index changes at the surface, which are detected with a delayed probe pulse through diffraction.

In the experiments presented in this chapter we use a transient grating to pump the sample [34] and measure the diffraction of the probe as function of delay time. The concept of using a transient grating to measure laser-induced acoustic waves can be summarised as follows, also shown in Figure 4.1. Two ultrafast pump laser pulses arrives to the surface with opposite angle. The generated interference pattern first excites the sample surface, giving rise to an elevated temperature of the electron gas in the bright fringes of the periodic pattern. The energetic electrons thermalize with the lattice which is initially cold, until a common temperature is reached. The rapid increase of lattice temperature causes an abrupt expansion of the sample top layer, which leads to the generation of a strain pulse whose spatial extent and frequency are determined by both the electron-phonon coupling strength and the electron transport and thermal diffusion. For strongly absorbing metals with high electron-phonon coupling, the energy transfer to the lattice is confined to a depth of a few nanometers, leading to a high frequency, longitudinal acoustic pulse that propagates into the sample at the speed of sound. The spatial inhomogeneity of the excitation profile results in the excitation of shear waves and surface acoustic waves (SAWs) [29, 85, 87, 92, 93] or guided modes such as Lamb waves [28]. The generated acoustic pulse, when being reflected at a material interface inside a sample, appears as an echo propagating back to the sample surface. This echo, manifesting itself as atomic displacements and/or a local modification of the dielectric constant, can be

detected optically by a delayed probe pulse through diffraction [34, 87]. For sufficiently large excitation energy, nonlinear acoustic waves and even solitons have also been observed [77, 94, 95].

In this chapter we introduce a two-dimensional model that fully captures the above mentioned physics and nanoscale interactions of laser-driven ultrasound in solids. We use this model in combination with transient grating experiments to characterize the propagation of ultrasound in various thin films, and to retrieve information on a multitude of material properties that govern dynamics on timescales ranging from femto- to nanoseconds. The model equations are efficiently solved by a self-developed numerical code adopting 2-dimensional Finite-Difference Time-Domain (2D-FDTD) method, enabling least-squares fitting of the experimental data to the model simulations and thus a quantitative extraction of multiple electronic, thermo-optic and acoustic parameters of the investigated materials. In addition, we show that this combined approach enables disentanglement of various contributions to the signal formation, including longitudinal and shear waves, SAWs, Lamb waves, acoustic diffraction, thermo-optic effect, Brillouin scattering and frequency-dependent damping and dispersion of the ultrasound waves. The model has already found successful application in disentangling various physical effects and understanding signal formations in pump-probe sub-surface alignment metrology in photolithography [96].

4.2. Numerical and experimental approaches

4.2.1. Simulation of ultrafast photo-acoustics

The first step of the model is the absorption of the laser pulse and the generation of thermal stress due to the sudden heating of the lattice. The optical intensity inside the sample is calculated by solving the Maxwell's equations using the material permittivity and laser parameters as input. The energy transfer between the electrons and lattices is modeled via the two-temperature model, assuming separate temperatures for the electron and lattice subsystems [9, 10], and including energy transport through electron and phonon dynamics. The temperature dependence of electron heat capacity and thermal conductivity are also taken into account. More details on this first step can be found in section 2.2 in Chapter 2.

In metals, thermoelasticity is the dominant mechanism for picosecond acous-

tic pulse generation [75, 76]. The elevation of the lattice temperature causes an isotropic thermal stress σ^{th} whose two cartesian components are given by

$$\sigma_x^{th} = \sigma_y^{th} = -3B\beta\Delta T_l(x, y, t), \tag{4.1}$$

where B is the bulk modulus and β is the linear expansion coefficient. The temperature increase $\Delta T_l(x, y, t)$ is obtained by the solution of the two-temperature model. Throughout this chapter, the coordinate x represents the axis perpendicular to the sample surface while y is the axis along the surface. To model the propagation of the sound waves, Eq. (4.1) is used as a source term in the equation of motion for an isotropic, linear elastic wave [15, 97]. The acoustic attenuation is introduced (additional relaxation effects will be introduced later) by adding two extra viscous terms as it is done in the Navier-Stokes equation [14, 88], resulting in the following equation of motion:

$$\begin{aligned} \rho\frac{\partial^2\mathbf{u}}{\partial t^2} = \mu\nabla^2\mathbf{u} &+ (\mu+\lambda)\nabla(\nabla\cdot\mathbf{u}) + \nabla\sigma^{th} \\ &+ \xi\nabla^2\mathbf{v} + (\xi+\lambda_v)\nabla(\nabla\cdot\mathbf{v}), \end{aligned} \tag{4.2}$$

where $\mathbf{u}$ is the displacement vector, ρ the mass density, λ and μ are the two Lamé parameters, $\mathbf{v}$ is the velocity vector, ξ the coefficient of shear viscosity and λ_v is linked to the coefficient of bulk viscosity η as $\lambda_v = \eta - 2\xi/3$. Expanding Eq. 4.2 in two-dimensional cartesian coordinate leads to two coupled differential equations for the velocity $\mathbf{v}$ and the strain field $\mathbf{s}$,

$$\begin{aligned} \frac{\partial v_x}{\partial t} &= -\frac{1}{\rho}\left(\frac{\partial\sigma_x^{re}}{\partial x} + \frac{\partial\sigma_{xy}^{re}}{\partial y} + \frac{\partial\sigma_x^{v}}{\partial x} + \frac{\partial\sigma_{xy}^{v}}{\partial y} - \frac{\partial\sigma_x^{th}}{\partial x}\right), \\ \frac{\partial v_y}{\partial t} &= -\frac{1}{\rho}\left(\frac{\partial\sigma_y^{re}}{\partial y} + \frac{\partial\sigma_{xy}^{re}}{\partial x} + \frac{\partial\sigma_y^{v}}{\partial y} + \frac{\partial\sigma_{xy}^{v}}{\partial x} - \frac{\partial\sigma_y^{th}}{\partial y}\right), \end{aligned} \tag{4.3}$$

and,

$$\frac{\partial s_x}{\partial t} = \frac{\partial v_x}{\partial x}; \quad \frac{\partial s_y}{\partial t} = \frac{\partial v_y}{\partial y}; \quad \frac{\partial s_{xy}}{\partial t} = \frac{\partial v_x}{\partial y} + \frac{\partial v_y}{\partial x}. \tag{4.4}$$

In the above equations, s_x and s_y are the components of normal strain and s_{xy} the shear strain, σ_x^{re} and σ_y^{re} are the normal stresses and σ_{xy}^{re} is the shear stress. The superscript "re" stands for "restoring" as they originate from the restoring force. The strain field and the stress field are linked through the strain-stress relation, which can be obtained in the expansion of Eq. 4.2 as well:

$$\begin{aligned} \sigma_x^{re} &= -(\lambda+2\mu)s_x - \lambda s_y; \quad \sigma_y^{re} = -(\lambda+2\mu)s_y - \lambda s_x, \\ \sigma_{xy}^{re} &= -\mu s_{xy}. \end{aligned} \tag{4.5}$$

The expansion of the attenuation terms in Eq. 4.2 leads to relations which link the viscous stresses to the strain rates:

$$\begin{aligned} \sigma_x^v &= -(\lambda_v+2\xi)\frac{\partial s_x}{\partial t} - \lambda_v \frac{\partial s_y}{\partial t}, \\ \sigma_y^v &= -(\lambda_v+2\xi)\frac{\partial s_y}{\partial t} - \lambda_v \frac{\partial s_x}{\partial t}, \\ \sigma_{xy}^v &= -\xi \frac{\partial s_{xy}}{\partial t}. \end{aligned} \tag{4.6}$$

As pointed out in Chapter 2, there is an analogy between the system of Eq. (4.3) and Eq. (4.4) coupled via Eq. (4.5) and Eq. (4.6), and the Maxwell equations coupled via the consitutive equations. Because of this analogy, Eq. (4.2) can be solved by the FDTD method [98], which was originally developed for solving the time-dependent Maxwell's equations [17].

The third step of the model is to calculate the optical response of the material. In picosecond ultrasonics experiments, a delayed (probe) pulse is used to detect the response of the sample due to the pump pulse. This is usually realized by measuring the changes in sample reflectivity [32], diffraction efficiency in the case of transient grating experiments [34, 87], or interferometric measurements [77, 80] where the electric field amplitude and phase of the probe pulse are both measured. From a modelling point of view, all these quantities require a calculation of the (reflected) complex electric field of the probe pulse in the presence of pump excitation. In general, the reflected electric field of the probe is affected by either surface displacement (which only influence the phase) or a local transient variation of the refractive index (which may influence both amplitude and phase) due to the presence of strain (strain-optic effect) or temperature elevation (thermo-optic effect). Using the outputs of the model in the previous steps, i.e., the lattice temperature, the strain field and the displacement field as a function of space and time, the reflected complex electric field can be calculated by numerically solving the Maxwell's equations for the probe pulse, providing that the strain-optic and thermo-optic coefficients are known. In this work we use the transfer-matrix method [99] to calculate the reflected field details.

4.2.2. Setup for ultrasound generation and detection

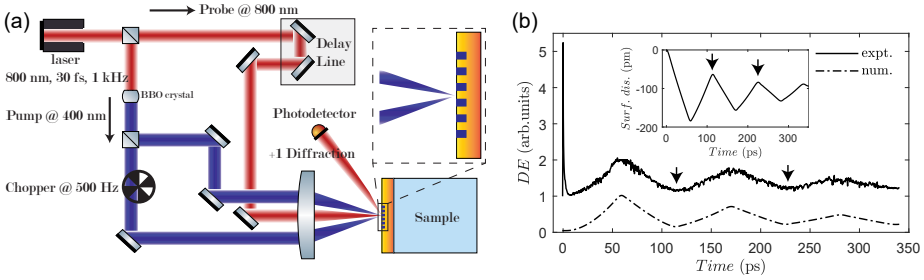

Figure 4.2: (a) Schematic of the experimental setup. Two crossed pump beams are used to create interference fringes on the sample surface. (b) Typical diffraction efficiency (DE) measurement on a 200 nm Au film deposited on glass substrate and model calculation which well reproduces the measured acoustic response. The inset shows calculated surface displacement (in the direction perpendicular to the surface) at the center of the grating line. The arrows mark the returning of echoes. Note the experimental curve has been given an offset for clarity.

A schematic of the experimental setup is shown in Figure 4.2(a). Pulses from an amplified Ti:Sapphire system (Femtopower, Spectra Physics, duration 30 fs, central wavelength 800 nm, repetition rate 1 kHz) are split into pump and probe pulses by a 1% beam splitter. The stronger part is frequency doubled in a BBO crystal to 400 nm wavelength to be used as pump beam. This beam is subsequently split into two beams by a 50% beam splitter. The two pump beams are then loosely focused onto the sample at a slightly oblique angle ($\sim 2^{\circ}$). The pump beam diameter on sample is estimated as 1 mm. The pump pulse energy ranges from 3 µJ to 15 µJ depending on the sample used. Special care was taken to ensure overlap of the two pump pulses in space and time, creating interference fringes with a period of 6 µm. The interference pattern excites the sample, leading to a spatially periodic heating of the sample surface and thus generating a spatially periodic array of acoustic pulses. This periodic array acts as a transient grating, propagates through the sample and internally reflects at material interfaces. A probe beam (800 nm) then illuminates the pumped surface, and its time delay with respect to the arrival of pump pulse is controlled via an optical delay line. This probe beam is then diffracted by the pump-induced change to the sample. The energy contained in the first-order diffraction is measured by a photodetector and the signals are subsequently sent through a box-car integrator and collected by a data acquisition card as a function of pump-probe delay. To improve detection accuracy, one of the pump beams passes through a 500 Hz mechanical chopper, so that the signal without pump ex-

citation is also measured. This allows us to subtract the background level from the signal with pump excitation to ensure that only the pump induced change is measured. The data belonging to the same pump-probe delay is averaged over 100-500 pulses to further increase signal-to-noise level.

Experimental data were obtained through measurements on either metal-film-on-substrate samples or free-standing metal membranes. Metals with a large difference in electron-phonon coupling strength (Au, Al and Ni) are chosen as electron-phonon coupling is the dominant factor determining the frequency of the excited sound waves. The use of free-standing membranes ensures that more acoustic echoes can be measured as reflection loss at interfaces is minimized, and metal-film-on-substrate samples are measured for comparison. Figure 4.2(b) shows a typical transient diffraction efficiency signal measured on a 200-nm-Au-layer on glass substrate sample. The fast signal around zero time delay originates from the generation of hot electrons, which give rise to a change in the local dielectric function. This contribution vanishes after a few picoseconds as the energy is transferred to the lattice due to electron-phonon coupling. This abrupt heating of the lattice sets up a thermal stress which generates acoustic pulses at material boundaries. In fact, the temperature distribution obtained during the calculation shows that the whole layer is heated up almost homogenously thanks to the relative weak electron-phonon coupling of Au combined with fast electron diffusion and ballistic range, compared with the relative thin film thickness. This near-homogenous heating generates two acoustic pulses launched almost at the same time, one starting at the Air/Au interface and the other starting at the Au/glass interface. The two acoustic pulses propagate in the opposite direction and reflect back and forth inside the Au layer, forming a "breathing-like" mode with a period determined by one round trip time of the acoustic pulses. These are recovered in the model calculation using electronic and mechanical properties of Au.

4.2.3. Fitting experimental data

To quantitatively extract the material properties, measured signal (data of $t >$5–10 ps after the electron-phonon coupling) as a function of pump-probe delay is then normalized by the maximum value and least-squares fitted using the model described in section 4.2.1. Important electronic and acoustic properties of the metal layers such as electron-phonon coupling, speed of sound, acoustic attenuation, thermal-optic coefficient etc. and some exper-

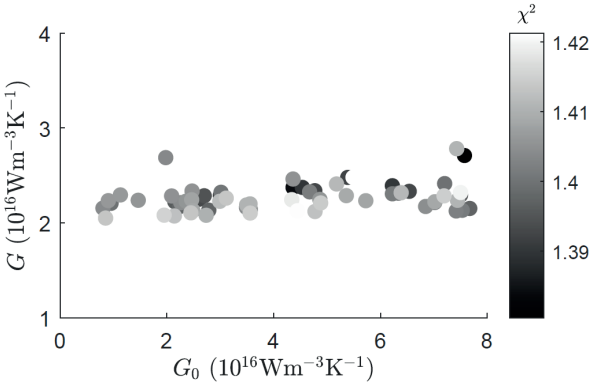

Figure 4.3: Fitted values (G) of electron-phonon coupling constant of Au, versus initial guessing values (G_0) randomly generated within predetermined interval $[0.78, 7.8] \times 10^{16}$. The color scale represents normalized residual (χ^2) foor each fit. Those fits within 3% variation to the smallest χ^2 are plotted and used for determining parameter bounds. The lower and upper bounds of G are defined as the minimum and the maximum values ($2.05 \times 10^{16} \leq G \leq 2.78 \times^{16}$).

imental conditions with small uncertainties such as the transient grating period are treated as fitting parameters while other parameters are either taken from known literature values or estimated from experimental conditions. Least-squares fitting with multiple fitting parameters can be hindered by multiple local minima in the fitting residual. In order to obtain a solution as close as possible to the true global minima, we use a so called "multi-start" fitting procedure. We first randomly generate some 200–500 parameter values for each of the fitting parameters within predetermined intervals, forming 200-500 initial parameter sets. Least-squares fitting routines are then carried out separately using each of the parameter sets as initial guess values. This procedure generates 200-500 optimized parameter sets. Those parameter sets are then sorted by their normalized fitting residual, χ^2. The best-fit values are determined as being the set of parameters which yields the lowest residual, χ^2_{min}. The upper and lower bounds of fitted parameters are also determined from those optimized parameter sets using a predefined $\Delta\chi^2 = (\chi^2 - \chi^2_{min})/\chi^2_{min}$ criterion. Figure 4.3 shows fitted electron-phonon coupling constants of Au using the "multi-start" fitting procedure as an example. In this fit, 200 initial values are randomly generated for each of the fitting parameter including the electron-phonon coupling constant. The predetermined interval is used as both the bounds for the generation of guess parameters and the final fitted values. Two hundred fitting routines are then carried out separately, and the one with the smallest normalized residual (χ^2

= 1.38) is selected as the best-fit (G = 2.71×10^{16} $Wm^{-3}K^{-1}$). The bounds of each fitted parameter can also be determined from the "multi-start" procedure using a predefined $\Delta\chi^2$ criterion. For example, the lower and upper bounds of G are defined to be the minimum and maximum values of those fits with a χ^2 within 3% of the lowest value.

4.3. Results and Discussion

4.3.1. Ultrasound characterization of a free-standing aluminium membrane

Experiments on Al were performed on a 400 nm free-standing membrane. In Figure 4.4(a) we plot the measured data, along with the best-fit model calculation, and the resulting diffraction efficiencies calculated by only the total surface displacement and by only the thermo-optic effect. The measured signal is a coherent sum of the electric fields of the individual contributions, rather than a direct sum of diffraction efficiencies. The surface displacement contribution acts as a pure phase grating while the thermo-optic contribution acts as both amplitude and phase grating. The signal of the first 50 ps is dominated by the thermo-optic effect which manifests as a decaying background caused by heat diffusion, and therefore we also treat the thermal conductivity as a fitting parameter to better recover the background. The calculated temperature evolution is shown in Figure 4.4(b). The contribution from surface displacement itself can be divided further into 3 sub-contributions, namely, from the thermal surface expansion (TSE, Figure 4.4(f)), the longitudinal acoustic waves (LAWs), Figure 4.4(f-h)), and the surface acoustic waves or more specifically, Lamb waves in free membranes(Figure 4.4(i)). The TSE is caused by the temperature increase and decays slowly as the surface cools down, while the longitudinal acoustic wave is generated because of the rapid surface expansion. The longitudinal wave which reflects off at the other side of the membrane, when it returns to the surface region, contracts the TSE and therefore reduces the diffraction signal. This event happens every acoustic round-trip time, thus appearing as equally spaced dips in Figure 4.4(a). These two contributions will be discussed further later in the discussion of the gold results: the difference is that we see a better separation of these two effects in the aluminum data because of a much shorter spatial extent of the excited acoustic pulse. This high frequency content results from aluminum's much higher electron-phonon coupling strength and slow electron thermal diffusion without ballistic transport. Another noteworthy observation is the overall increase of diffraction efficiency after $\sim$ 400 ps, which we believe is

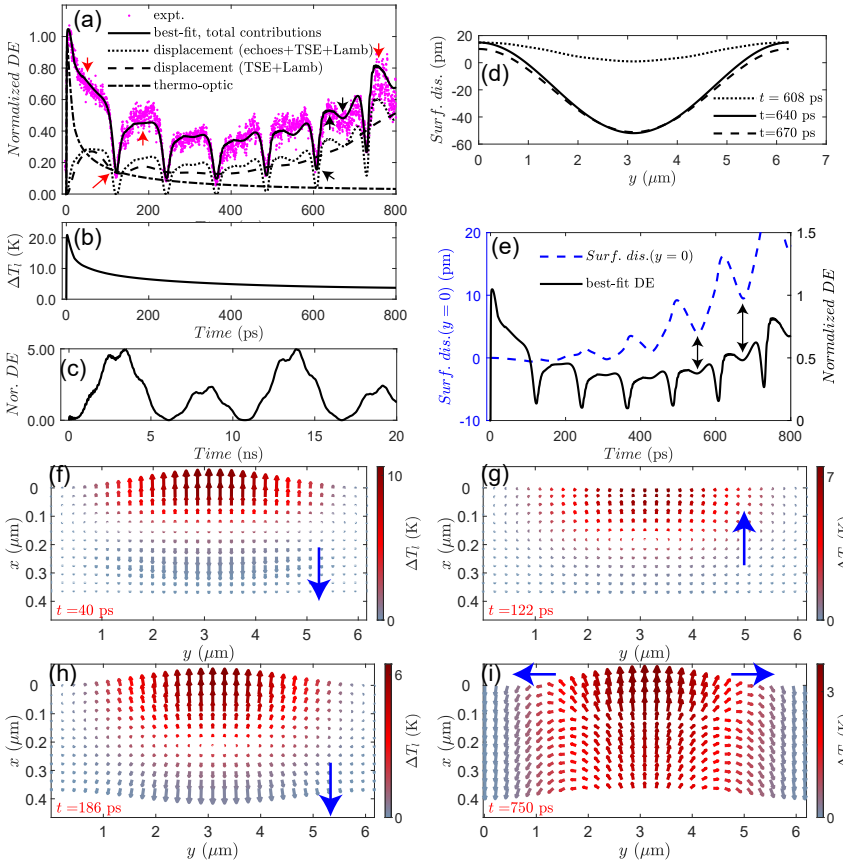

Figure 4.4: (a) Measured diffraction efficiency (dots) and corresponding model fit (solid line) on a 400 nm Al free-standing membrane. The dotted line, dashed line, and dash-dotted line are diffraction efficiencies from each contributions: the total surface displacement, surface displacement of TSE and Lamb waves, and the thermo-optic effect. The increase of surface temperature at the center of grating line is shown in (b). Calculated diffraction efficiency (normalized) due to the interference of Lamb waves is shown in (c) for an extended period of time, illustrating its periodic nature. The normal component of the displacement vector along the sample surface is shown in (d) for 3 time instants which are marked by black arrows in (a). (e) Normal component of the surface displacement vector (blue dashed line) at the periodic boundary ($y = 0$). The double-side arrows mark the timing of the extra dips. The displacement vector distribution at 4 time instants (marked by red arrows in (a)) which illustrate (f) the generation of TSE and longitudinal acoustic wave, (g) contraction of the surface due to the returning of the longitudinal wave, (h) the recovery of the TSE, and (i) the appearance of Lamb waves at longer time delays. The color represents the increase in the lattice temperature. The blue arrows indicate the propagation direction of the longitudinal wave and Lamb waves. Note that the displacement vectors are highly exaggerated to be visible for solely illustrative purpose.

caused by an excitation of Lamb waves. This is further substantiated by running a simulation with a very high attenuation coefficient set for the longitudinal waves, so that the longitudinal echoes are damped out in the first few round-trips, leaving only the contributions from TSE and Lamb waves at longer time delays. The resulting model signal is shown by the dashed line in Figure 4.4(a), in which we see the same increase in diffraction efficiency after 400 ps as the experimental measurement. In Figure 4.4(c) we plot an extended calculation from only the TSE and Lamb waves, up to 20 ns. The result shows a periodic oscillation with a period of $\sim$ 10.6 ns. On top of this slow oscillation we also observe a smaller but faster oscillation with a period of $\sim$ 1 ns. This oscillatory signal is due to the interference of excited Lamb waves at the periodical boundary. These two frequencies ($\sim$ 0.59 GHz and $\sim$ 6.3 GHz) correspond to the two lowest Lamb modes of the membrane. A 2D Fourier transform (1D spatial and 1D temporal) of the calculated displacement along the surface $u_x(0, y, t)$ reveals the dispersion relation of Lamb waves in the Al free-standing membrane. The result is shown in Figure 4.5 and compared with the analytical solution of the Lamb wave dispersion relations [18, 100]. In the simulation, a source with small lateral dimension ($\sim$ 500 nm) is chosen to cover a wider k space. The model faithfully reproduces the analytical results. The expected frequencies of the first two lowest branches (at the transient grating wavenumber) are ω_{A_0} =0.61 GHz and ω_{S_0} =5.5 GHz.

Another intriguing aspect is the appearance of additional dips between the echoes, such as the one marked by the arrow at $t = 670$ ps in Figure 4.4(a). Our model calculation suggests these dips are not longitudinal echoes, but actually result from mode conversion from longitudinal mode to higher order Lamb mode. Figure 4.4(d) shows calculated surface displacement profiles at 3 time instants corresponding to the appearance of a longitudinal echo at $t = 608$ ps, the recovery of the echo event at $t = 640$ ps, and the appearance of the additional dip at $t = 670$ ps. As discussed before, the longitudinal echo is caused by a compensation of the TSE, therefore Figure 4.4(d) shows a large difference between the dotted line and the solid line in the center of the grating line where the local optical intensity is maximal. However, as shown by the difference between the dashed line and the solid line, the additional dip is caused by a change of surface displacement in a region close to the periodic boundary where the optical intensity is minimal. In Figure 4.4(e) we show the calculated surface displacement (in the direction of surface normal) at the periodic boundary (y=0) as a function of pump-probe delay. The timings of the additional dips are perfectly aligned with the dips in the surface displacement at y=0. This indicates that the origin

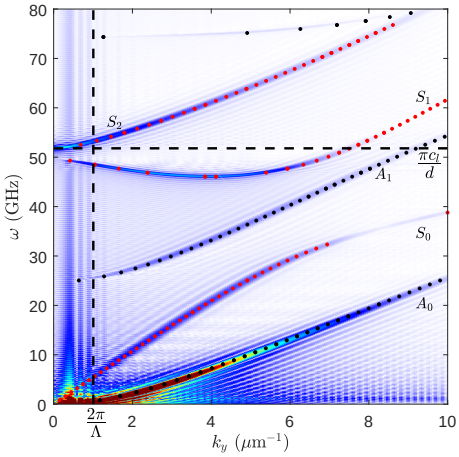

Figure 4.5: Dispersion relation of Lamb waves in the Aluminium membrane retrieved from the simulation (color map). The black and red dots are the solution of the analytical expression of Lamb wave dispersion relations. Black dots correspond to asymmetric modes, and red dots to the symmetric modes. The vertical dashed line indicates the wave number of the transient grating used in the experiment, the horizontal dashed line indicates the round-trip frequency of longitudinal echoes.

of the additional dips is due to waves that are travelling along the surface, which results in constructive interference at the periodic boundaries. In thin free-standing membranes, these waves are a specific case of surface-guided waves called Lamb waves [18, 100]. The free boundary condition of membranes imposes that specific combinations of frequencies and wave numbers are allowed propagating waves while other combinations are evanescent. The dispersion relation shows a branch (S_2) starting at the round-trip frequency $\omega = \frac{\pi c_l}{d}$ of the longitudinal echoes, irrespective of the film thickness. This corresponds to the fundamental longitudinal vibration mode of the membrane. The longitudinal echo has a central frequency of $\frac{\pi c_l}{d}$, which naturally overlaps with this branch. Our present transient grating experiment can be seen as an effective excitation around the wave vector $k_y = \frac{2\pi}{\Lambda} = 1 \ \text{m}^{-1}$, where $\Lambda = 6.24 \ \text{m}$ is the transient grating period. Therefore, the longitudinal echoes effectively excite the S_2 branch at $k_y = 1 \ \text{m}^{-1}$. Due to the diffraction of the longitudinal waves, part of the longitudinal echo arrives at the free boundary at an oblique angle, causing particle movement along the surface direction and converting some of its energy to the S_2 Lamb wave mode every time it reaches the metal-air interface. From the dispersion relation, we calculate the phase velocity of the S_2 Lamb wave at $k_y = 1 \ \text{m}^{-1}$ as $v_{S_2} = 5.23 \times 10^4$ m/s. The time for the excited S_2 Lamb wave to travel across

one period of the transient grating then is $\frac{\Lambda}{v_{S_2}} = 119.4$ ps, very close to the round-trip time of the longitudinal echoes $\frac{2d}{c_l} = 121$ ps. This agrees with the experimental observation that the period of the additional echoes appears the same as the longitudinal echoes. Thus the additional echoes can be explained as interference of S_2 Lamb waves at the periodic boundary which themselves are excited by mode conversion (longitudinal to Lamb mode). For small values of k_y, the slope of the S_2 branch on the determination of its phase velocity can be neglected, giving an approximation of $v_{S_2} = \frac{\pi c_l}{d} / \frac{2\pi}{\Lambda} = \frac{c_l \Lambda}{2d}$. Thus the predicted period of the additional echoes is $\frac{\Lambda}{v_{S_2}} = \frac{2d}{c_l}$, exactly the same as the round-trip time of the longitudinal echoes. This means that for small transient grating wavenumbers, the period of additional echoes is always the same (approximately) as the longitudinal echoes, irrespective with film thickness. This is also confirmed by simulations. The above analysis can also be used to understand the timing of the additional echoes to be in the middle of the longitudinal echoes. Since the above S_2 Lamb waves are excited at the moment when longitudinal echoes return to the surface, the time delay between the longitudinal echo and the time when the excited Lamb waves reaches the periodic boundary (and therefore interference maxima occurs) is $\Delta t = \frac{0.5\Lambda}{v_{S_2}}$, which is half of the longitudinal round-trip time. This means that there is a constant π phase delay between the appearance of the additional echoes and the longitudinal echoes. The growing amplitude of the additional echoes over time can be understood as an increasing mode conversion to the Lamb mode as more longitudinal reflections occur at the surface.

The fitting of model calculations to the experimental data was done with a "multi-start" procedure with 500 randomly generated initial parameter sets. The best-fit parameters and their comparison with reference values are summarized in Table 4.1 at the end of the chapter. By comparing different model fits, we found that acoustic attenuation was not significant for the present parameter range in aluminum, and conclude that the attenuation length far exceeds the measured acoustic propagation distance of ~ 5 m. The electron-phonon coupling strength of aluminium is about an order of magnitude larger than for gold [11]. This property of Al is correctly captured in the fitting result and the obtained value is somewhat lower than the reported DFT calculations [11]. Regarding the layer thickness, the sample specification gives an uncertainty smaller than 1 nm (d=391.1 nm), thus the thickness was fixed to this value during the fitting. As a result, the best-fit speed of sound has a very small uncertainty. Different from the case of gold as will be shown later, in which the measured data can be well-explained by contribution

from only the surface displacement, the data of aluminum suggests a large contribution from the thermo-optic effect. This is to be expected, as the 800 nm probe wavelength coincides with the peak of the thermoreflectance spectrum of aluminum [101]. To determine the complex thermo-optic coefficient, we treat its real and imaginary parts as two extra fitting parameters. Their best-fit values are shown in Table 4.1. From this thermo-optic coefficient, we then calculate the thermoreflectance using the Fresnel equation, resulting in a value of $\frac{dR}{RdT} = 1.58 \times 10^{-4}$ K^{-1}, which lies well-within the range of other reported thermoreflectance data [101–103]. To the best of our knowledge, there is no direct report of the complex thermo-optic coefficient of aluminum in the literature, although the optical conductivity of Al measured at various temperatures is reported in [104]. From this conductivity data together with the reported thermoreflectance data we then deduce the real and imaginary parts of the thermo-optic coefficient as reference values by inverting the Fresnel equation. Our best-fit coefficients are consistent with those deduced values. This demonstrates the ability to extract not only the thermoreflectance, but also the real and imaginary parts of the thermo-optic coefficient.

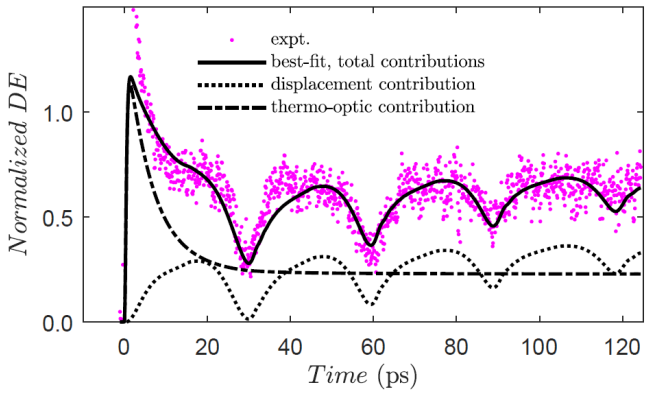

Figure 4.6: Measured diffraction efficiency (dots) as a function of pump-probe delay and corresponding best model fit (solid line) on a 100 nm Ni layer on glass substrate. The other two lines show the contribution from surface displacement (dotted line) and thermo-optic contribution (dash-dotted line), respectively

In Figure 4.6 we show the measurement and the fit done on a 100 nm Ni sample on a glass substrate. The results of the fit are include in Table 4.2 at the end of the chapter. It is worth noting that the detected signal on Ni contains comparable contributions from surface displacement and the

thermo-optic effect. The thermo-optic coefficient of Ni at 800 nm is of the opposite sign to that of Al [103], and this is again correctly captured in the material parameters retrieved from the Ni data presented in Table 4.2.
In a short summary for Al, the signal we measured at 800 nm probing wavelength is a result of coherent sum of multiple physical effects, including surface displacement caused by thermal surface expansion and propagating longitudinal acoustic waves, mode conversion from longitudinal modes to higher order Lamb modes, interference of Lamb waves, and refractive index variation by the thermo-optic effect.

4.3.2. Measurements on gold films: complex ultrasound attenuation behaviour

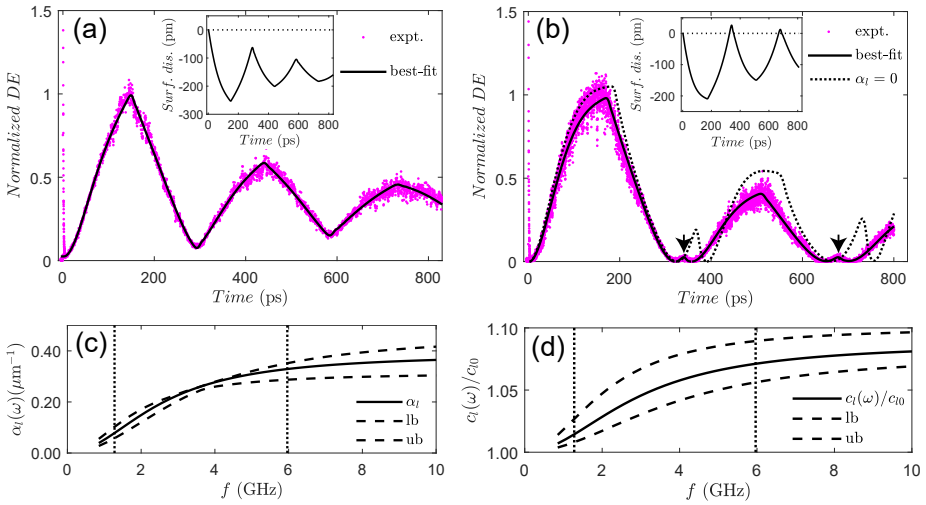

Figure 4.7: Measured diffraction efficiency (dots) as a function of pump-probe delay and corresponding model fits (solid lines) on (a) 500 nm Au on glass substrate sample and (b) 500 nm Au free-standing membrane. The dotted-line in (b) is a calculation with no acoustic attenuation ($\alpha_l(\omega) = 0$). The insets are the calculated surface displacement at the center of the grating line. The dash-lines mark the level of zero surface displacement. (c) Frequency-dependent acoustic attenuation and (d) phase-velocity dispersion calculated by Eq. 4.11 and Eq. 4.12 using the best-fit parameters (solid lines). The dashed-lines are lower and upper bounds obtained from those fits with a 3% $\Delta\chi^2$ criterion. The vertical dotted-lines indicate the FWHM of the acoustic pulse bandwidth.

Transient grating experiments on gold were performed on two types of samples: a 500 nm Au layer deposited on a glass substrate and a 500 nm Au free-standing membrane. The measured data for both types of samples, along

with the best-fit model results, are shown in Figure 4.7(a-b). Strikingly different from the results of Al, fitting of the data of both gold samples reveals large contributions from acoustic attenuation. This behaviour requires an extension of the model to include the influence of microscopic damping mechanisms, as discussed below. At room temperature, the dominant mechanism for acoustic attenuation results from the interaction of acoustic phonons with thermal phonons [89–91], a relaxational damping process that was first proposed by Akhiezer [105]. In this process, the sound waves disturb the distribution function of the thermal phonons, and the return of the system to equilibrium through phonon collisions removes the energy from the sound wave. The acoustic wave described by Eq. 4.6 exhibits viscous losses with quadratic power dependence on frequency, as it is the case in the Navier-Stokes equation. However, the Akhiezer damping mechanism can exhibit deviations from the quadratic power law, which has been observed in ultrafast laser induced ultrasound waves [89–91]. Macroscopically, the Akhiezer damping manifests itself as a relaxation process originating from a noninstantaneous response of the medium to the change of the strain. An analogous effect in optics is the electromagnetic wave propagation in a lossy and dispersive medium, where the electric polarization density does not only depend on the electric field at the current time, but also on its values at all earlier times [98, 99]. To incorporate the relaxational Akhiezer damping into our model, we rewrite Eq. 4.6 as a convolution,

$$\begin{aligned}\sigma_x^v &= -G_l(t) * [(\lambda_v + 2\xi)\frac{\partial s_x}{\partial t} + \lambda_v \frac{\partial s_y}{\partial t}],\\ \sigma_y^v &= -G_l(t) * [(\lambda_v + 2\xi)\frac{\partial s_y}{\partial t} + \lambda_v \frac{\partial s_x}{\partial t}],\\ \sigma_{xy}^v &= -G_s(t) * \xi \frac{\partial s_{xy}}{\partial t},\end{aligned} \tag{4.7}$$

where $G_l(t)$ and $G_s(t)$ describe the relaxation process for the normal and shear waves, respectively. Both $G_l(t)$ and $G_s(t)$ follow a functional form of the type

$$G_l = \frac{1}{\tau_l} e^{\frac{t}{\tau_l}} H(t); \quad G_s = \frac{1}{\tau_s} e^{\frac{t}{\tau_s}} H(t) \tag{4.8}$$

where H(t) is the Heaviside step function, τ_l and τ_s are the characteristic time of the relaxation process involving longitudinal and shear phonons, respectively. As $\lim_{\tau \to 0} \omega_0 \, \mathrm{G(t)} = \delta(\mathrm{t})$, Eq. 4.7 becomes Eq. 4.6 for the limiting case. For a nonzero relaxation time, the viscous stress is determined by the history of the strain rate but with its contribution decreasing exponentially

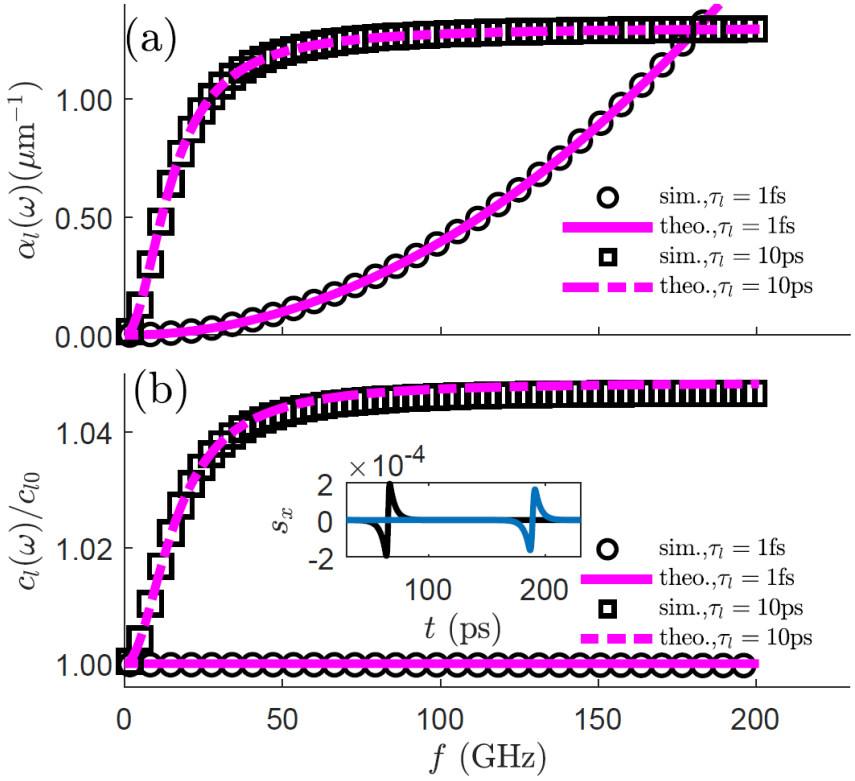

Figure 4.8: Frequency-dependent (a) attenuation and (b) phase velocity (normalized) of the longitudinal wave extracted from FDTD simulations, for τ_l = 1 fs, α_{l0} = 1 GHz^{-2}m^{-1} (black circle) and τ_l = 10 ps, α_{l0} = 150 GHz^{-2}m^{-1} (black square). The corresponding curves by using Equations 4.11 and Equations 4.12 are shown as dashed lines and solid lines. The inset shows the calculated strain profile at the two recording positions, for τ_l = 1 fs, α_{l0} = 1 GHz^{-2}m^{-1}. Other parameters used in the calculations are taken from the data of Au.

over the course of the history.

The method for solving the convolutions involved in Eq 4.7 is explained in the appendix to the chapter. In order to find the attenuation and dispersion behavior of the model with the implementation of Eq. 4.7, the one dimensional version of Eq. 4.4 and Eq. 4.3 together with Eq. 4.1, Eq. 4.5, and Eq. 4.7 are solved by the FDTD method. An artificial lattice temperature function T_l(x; t) with a skin depth of 15 nm and a rise time of 1 ps is used

as an excitation source for the simulation. The 1 ps rise time is chosen to ensure a frequency spectrum in the GHz to THz range. The resulting strain temporal profile $s_x(t)$ is then retrieved at two different locations x_1 and x_2 separated by a distance d. The ratio of Fourier transforms of the strain at these two locations reveals the frequency-dependent attenuation $\alpha_l(\omega)$ of the longitudinal waves manifested by the model. Similarly, the frequency-dependent phase velocity $c_l(\omega)$ can be retrieved by computing the phase shift upon propagation over d, i.e.,

$$\alpha_l(\omega) = -\frac{1}{d}\ln|\frac{\hat{s_x}(\omega, x_2)}{\hat{s_x}(\omega, x_1)}|; \quad c_l(\omega) = \frac{\omega d}{arg(\frac{\hat{s_x}(\omega,x_2)}{\hat{s_x}(\omega,x_1)})}, \tag{4.9}$$

where $\hat{s_x}$ is the Fourier transform of $s_x(t)$. Eq. 4.9 can be obtained by writing a strain field with frequency ω_0 as $\hat{s_x}(\omega; x) = s_0 exp(ikx)\delta(\omega - \omega_0)$, where $k = \omega/c_l(\omega) + i\alpha_l(\omega)$ is the complex wave number, and taking their ratio at the two locations. We plot in Figure 4.8 the numerical calculations of Eq. 4.9 for two different values of τ_l: 1 fs (black circle) and 10 ps (black square). In the plot the results of our numerical implementation are compared with the expected results according to Akhiezer model. The attenuation $\alpha_l(\omega)$ for the Akhiezer damping is [89, 90]

$$\alpha_l(\omega) = \frac{C_l T_l}{2\rho c_l(\omega)^3}\frac{\omega^2\tau_l}{1+\omega^2\tau_l^2}(\langle\gamma^2\rangle - \langle\gamma\rangle^2), \tag{4.10}$$

where $c_l(\omega)$ the frequency-dependent longitudinal speed of sound, γ is the Grüneisen parameter of the thermal phonons, and τ_l is the longitudinal phonon relaxation time. The angular brackets stand for an average over the entire population of the thermal phonons. A similar expression also holds for the shear waves [106]. This expression can also be described by using a phenomenological parameter, the bulk viscosity $\eta = C_l T_l \tau_l(\langle\gamma^2\rangle - \langle\gamma\rangle^2)$ as

$$\begin{aligned}\alpha_l(\omega) &= \frac{\eta}{2\rho c_l(\omega)^3}\frac{\omega^2}{1+\omega^2\tau_l^2} \\ &= \alpha_{l0}(\frac{c_{l0}}{c_l})^3\frac{\omega^2}{1+\omega^2\tau_l^2},\end{aligned} \tag{4.11}$$

where we introduce the longitudinal speed of sound in the low frequency limit c_{l0} and $\alpha_{l0} = \eta/(2\rho c_{l0}^3)$. It is apparent that in the low frequency limit ($\omega\tau_l \ll 1$), $\alpha_l = \alpha_{l0}\omega^2$, Eq. 4.11 reduces to the quadratic power law.

Because of the delayed response in Eq. 4.7, there must be associated acoustic dispersion, a requirement implied by causality: we find that the frequency-dependent phase velocity $c_l(\omega)$ exhibited by the model with the incorporation of Eq. 4.7 can be exactly described by the following expression

$$c_l(\omega) = c_{l0}(1 + \alpha_{l0} c_{l0} \frac{\omega^2 \tau_l}{1 + \omega^2 \tau_l^2}). \tag{4.12}$$

The obtained diffraction efficiency data in gold samples was fitted using the model with the incorporation of Eq. 4.7, starting with 200 random initial parameter sets. Important fitting parameters include the electron-phonon coupling constant, sound velocity, bulk viscosity, and the phonon relaxation time. The retrieved best-fit values are given in the Table 4.3 for 500 nm Au on glass and Table 4.4 for 500 nm Au free-standing membrane.

A comparison of the calculated diffraction efficiency using the best-fit parameters to the measured data is given in Figure 4.7(a-b). As can be seen, the numerical calculations accurately reproduce the measurements. There are a few points worth mentioning in regards to these fits. Firstly, the electron response is not included in the model and therefore only the data points for $t > 10$ ps, when the electron gas has thermalized with the lattice, are used in the fits. Secondly, in contrast to the Al data, the contribution from surface displacement alone can explain the measured data very well. Thirdly, the sudden heating of the metal layer after electron-phonon thermalization gives rise to two effects: a thermal surface expansion (TSE) and the launch of an acoustic pulse. Both these effects lead to surface displacement and therefore both act as a phase grating seen by the probe pulse. For the 500 nm Au layer thickness, the spatial extent of the acoustic pulse is still too large to see a complete separation of the two contributions. The TSE manifests itself as a decaying background, because heat diffusion tends to reduce the surface-expansion. The traveling acoustic pulse, compensates the surface-expansion once every roundtrip time because of an opposite direction in the displacement vector: the reflected acoustic pulse arrives at the surface as a contraction instead of an expansion. For this reason, the acoustic echoes in Figure 4.7(a) appears as dips in the diffraction signal. The situation is a bit different in the membrane sample as can be seen in Figure 4.7(b), for which the echoes contain small bumps (marked by arrows) inside of large dips. This is because in the case of free-standing membrane, there is almost no reflection loss at material interfaces. As a results, the returning acoustic pulse is not only strong enough to fully compensate the (reduced) surface-expansion, but also change its direction (note the change of sign in

the surface displacement plot). The height of this bump is largely determined by the amount of acoustic attenuation. In the unrealistic case of zero acoustic attenuation ($\alpha_l = 0$ of Figure 4.7(b)), the bumps would be much more pronounced. We note that reflection losses at material interface due to scattering by roughness could be another mechanism for acoustic attenuation. Atomic force microscopy (AFM) was used to characterize the surface roughness of the gold films. While scattering is expected to be significant when the roughness size is comparable to the acoustic wavelength, the AFM data shows that the RMS roughness is only ~ 0.5 nm, well below the acoustic wavelength in the gold samples. In addition, the fit results of the 200 nm gold sample (Figure 4.2(b)) suggest a very similar acoustic attenuation per unit propagation length as the 500 nm gold films. Considering the more frequent interface reflections (per propagation length) in the thinner sample, if the scattering loss dominates, the extracted acoustic attenuation per unit length would have been much larger. Due to these considerations, the scattering of acoustic waves at material interface is not considered further in our analysis.

The effect of acoustic dispersion can already be seen in Figure 4.7(b) by the lower sound velocity (c_{l0}) in the dotted-line. The fitting yields the parameters α_{l0} and τ_l with which the frequency-dependent attenuation and phase-velocity dispersion can be obtained by evaluating Eq. 4.11 and Eq. 4.12. These quantities are plotted in Figure 4.7(c-d). Rather than an ω^2-dependence expected for the low-frequency limit, the observed attenuation is even slower than ω^1. Using the best-fit parameter $\tau_l = 55$ ps and the central frequency of excited acoustic wave $f_0 = 2.77$ GHz in Au, we obtain $\omega_0\tau_l = 0.96$, indicating an intermediate regime $\omega\tau_l \sim 1$. It is worth noting that we have also performed a fit with a fixed $\tau_l = 1$ fs (thus $\omega\tau_l \ll 1$), forcing it to be in the frequency squared regime. In this case, we got a worse fit with almost twice the residual ($\chi^2 = 2.4$). This means that acoustic attenuation in this high frequency regime is better explained by relaxation damping, and incorporating such damping behaviour into the model improves the ability to model high frequency ultrasound attenuation in picosecond ultrasonic experiments.

The observed diffraction signal when probing from the air side does not contain a detectable contribution from the strain-optic effect. However, when we probe from the substrate (glass) side, the signal shows high frequency oscillations in addition to the expected surface displacement contribution. We attribute these additional oscillations to the strain-optic effect resulting from the acoustic wave propagation in the glass substrate. The generated acoustic pulse from the metal layer is partially transmitted into the substrate,

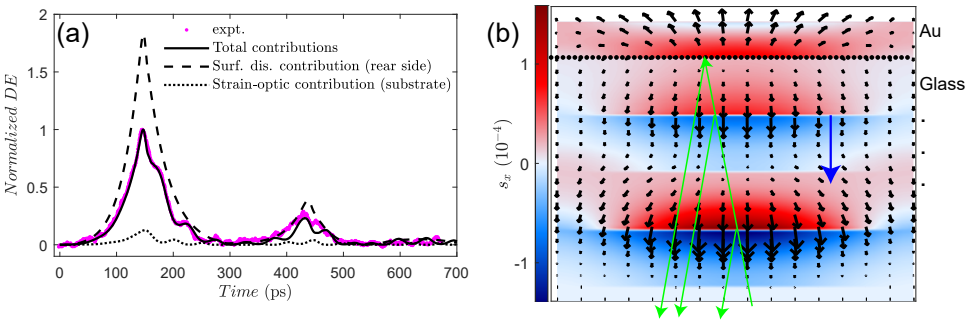

Figure 4.9: (a) Measured diffraction efficiency (magenta dots) and the corresponding model calculation (solid line) on the 500 nm Au on glass sample pumped from the Au-Air side and probed at the Au-Glass interface. The diffraction efficiency (normalized by the maximum of the total contributions) calculated by only the displacement at the Au-Glass interface and by only the strain-optic effect in the glass substrate are shown as dash and dotted lines. The total contributions are a coherence addition of these two effects. (b) Strain (s_x component, color scale) and displacement vector distribution (black arrows) at $t = 582$ ps. Positive strain represents expansion while negative strain means compression. The filled-circles indicate the location of the Au-Glass interface. The blue arrow shows the propagation direction of the strain wave in glass. The green arrows illustrate the reflection of the probe pulse from the propagating strain pulses and the gold rear surface.

resulting in a local expansion and compression of the glass, thus altering its refractive index. This strain wave forms additional gratings in the substrate, propagating at the speed of sound. The probe pulse then diffracts from both this moving strain wave and the substrate-metal interface, and these diffracted fields interfere constructively or destructively depending on the changing optical path difference. The overall effect is an oscillatory signal with a periodic given by $T = \frac{\lambda}{2nc_l cos(\theta)}$, where λ is the probe wavelength, n is the refractive index, c_l is the speed of sound in glass and θ is the angle of incidence. This effect known as Brillouin scattering is usually observed when performing reflectivity measurements [107–110]. In the present diffraction geometry, we observe a unique coherent addition of the Brillouin scattering and the surface displacement signal. Figure 4.9(a) shows the measured diffraction efficiency and the model calculations when probing through the glass substrate side. In the calculations, we use the extracted parameters from the signal obtained when probing from the air side (Figure 4.7(a)) and adjust the strain-optic coefficient of glass and the speed of sound in glass until a good match is found. The obtained values are $\frac{\partial n}{\partial s_x} = -0.35$ and $c_{gl} = 5.56$ km/s. In the experiments we use linearly polarized beam at normal incidence. Because the electric field vector of the probe beam is per-

pendicular to the propagation direction of the longitudinal acoustic wave, when the longitudinal strain is the only nonzero component, only the contribution from P_{12} of the photoelastic tensor is measured. Using the relation $P_{12} = -2\frac{\partial n}{\partial s_x}/n^3$ we obtain $P_{12} = 0.23$, in very good agreement with the reported value $P_{12} = 0.252$ [111].

As shown in Figure 4.9(a), the signal shape and the detailed high frequency oscillations are well-reproduced, especially at early time delays. The strain-optic contribution here is calculated by using the simulated strain $s_x(x, y, t)$ and the transfer matrix method. The measured signal is a coherent addition of the displacement at the gold rear surface and the strain-optic effect caused by the acoustic wave propagation in the glass substrate. The slight mismatch after 400 ps may be due to the excitation of off-axis components (s_y and s_{xy}) as a result of acoustic diffraction. The off-axis components can introduce optical anisotropy and the probe may sample other elements of the photoelastic tensor. The displacement vectors at $t = 582$ ps as shown in Figure 4.9(b) exhibit off-axis components in the region close to the periodic boundary. An extension of the probe calculation to include anisotropic media can further improve the results at longer time delays.

4.4. Summary

In this chapter we have introduced a new approach to picosecond ultrasonics, which enables quantitative material characterization and the non-invasive study of optically opaque nanoscale materials using light-driven ultrasound. We achieve this by introducing an advanced 2D numerical model that captures the generation, propagation and detection of these ultrasound waves in full detail, and subsequently combining this model with measured data from picosecond ultrasonic experiments. By fitting the model to the experimental results, a detailed interpretation of the results in terms of the underlying physics is obtained, and a wide range of material properties is retrieved. To demonstrate this ability, we have demonstrated an simultaneous extraction of electron-phonon coupling constant, speed of sound, frequency-dependent acoustic attenuation and dispersion, and thermo-optic coefficients of several different materials as well as strain-optic constant with retrieved parameters that are consistent with literature values to the extent at which they were known. The extracted acoustic attenuation in gold films shows a frequency-dependency that deviates significantly from the quadratic power dependence, owing to enhanced relaxation damping in this high frequency

range. In addition, we separate different contributions to the measured signal by simulations with the best-fit parameters. The results show large contributions of thermo-optic effects in Al and Ni and negligible contribution in Au at 800 nm probing wavelength. For aluminium, we identify the contributions of Lamb waves and mode conversion from longitudinal to Lamb waves, which are found to cause a gradual increase of the background level and additional dips at longer time delays. Furthermore, when probing from the glass side, we observe a unique coherent addition of the Brillouin scattering on top of the surface displacement signal which is well reproduced by simulations. Our model therefore holds great promise for disentangling various physical effects and interpreting signal formations in samples with complex geometries and advanced applications with surface nanotopographies and highly focused beams.

Table 4.1: Best-fit parameter values on 400 nm Al free-standing membrane

Parameter	Explanation	Unit	Best-fit-value	lb [1]	ub[1]	Reference-value
G	electron-phonon coupling strength	$10^{16}\mathrm{Wm^{-3}K^{-1}}$	14	13.5	18.1	24.6 [11]
c_{l0}	longitudinal sound velocity	km/s	6.447	6.445	6.447	6.42 [112]
k_l	thermal conductivity	$\mathrm{Wm^{-1}K^{-1}}$	110	106	118	237 [112]
$\frac{\partial n}{\partial T}$	thermo-optic coefficient, real part	$-1\times10^{-3}\mathrm{K^{-1}}$	1.89	1.83	2.03	2.96–4.08[2]
$\frac{\partial \kappa}{\partial T}$	thermo-optic coefficient, imaginary part	$10^{-3}\mathrm{K^{-1}}$	2.62	2.16	2.8	0.4–4.4[2]
$\frac{dR}{RdT}$ [3]	thermoreflectance @ 800 nm	$10^{-4}\mathrm{K^{-1}}$	1.58	1.49	1.61	1.14–2.4 [101–103]

[a]The lower and upper bounds are determined by using a 5% $\Delta\chi^2$ criterion.
[b]The reference value on thermo-optic coefficient are determined by the optical conductivity data at varies temperatures in Ref. [104] together with available thermoreflectance data in Ref. [101–103].
[c]It is not a parameter used in the fit but is determined from the best-fit thermo-optic coefficient. Acoustic pulse central frequency $f_0 = 29.2$ GHz, FWHM bandwidth: $[8.6, 51.6]$ GHz.

Table 4.2: Best-fit parameter values on 100 nm Ni on glass

Parameter	Explanation	Unit	Best-fit-value	lb^1	ub^1	Reference-value
G	electron-phonon coupling strength	$10^{16}\mathrm{Wm^{-3}K^{-1}}$	98	94	176	106 [11]
c_{l0}	longitudinal sound velocity	km/s	6.643	6.093	6.643	6.04 [112]
d	metal layer thickness	nm	98	90	98	100±10
k_l	thermal conductivity	$\mathrm{Wm^{-1}K^{-1}}$	156	92	198	90.9 [112]
$\frac{\partial n}{\partial T}$	thermo-optic coefficient, real part	$-1\times10^{-3}\mathrm{K^{-1}}$	2.5	1.3	3.4	no data
$\frac{\partial \kappa}{\partial T}$	thermo-optic coefficient, imaginary part	$10^{-3}\mathrm{K^{-1}}$	1.8	2.5	0.73	no data
$\frac{dR}{RdT}$ [2]	thermoreflectance @ 800 nm	$10^{-5}\mathrm{K^{-1}}$	4.1	4.5	3.5	$\sim$ 2 [103]
c_{gl} [3]	speed of sound in glass	km/s	5.16			

[a] The lower and upper bounds are determined by using a 5% $\Delta\chi^2$ criterion.
[b] It is not a parameter used in the fit but is determined from the best-fit parameters.
[c] This value , taken from Table 4.3, is fixed during the fitting. Acoustic pulse central frequency f_0 = 40.3 GHz, FWHM bandwidth: [15.7, 105.2] GHz.

Table 4.3: Best-fit parameter values on 500 nm Au on glass

Parameter	Explanation	Unit	Best-fit-value	lb^1	ub^1	Reference-value
G	electron-phonon coupling strength	$10^{16}\mathrm{Wm}^{-3}\mathrm{K}^{-1}$	2.71	2.05	2.78	2.1-4.0 [7, 11, 51, 113]
c_{l0}	longitudinal sound velocity	km/s	3.09	3.04	3.24	3.24 [112]
α_{l0}	attenuation prefactor	$\mathrm{GHz}^{-2}m^{-1}$ 2413	1828	4259	no data	
τ_l	phonon relaxation time	ps	74	58	109	no data
d	metal layer thickness	nm	491	488	528	500±50
c_{gl}	longitudinal speed of sound in glass	km/s	5.16	4.99	5.8	4-6 [112]
$\mathrm{P}_{12}{}^2$	photoelastic constant of glass		0.23			0.252 [111]
$\alpha_l(f_0)^3$	attenuation at central frequency	10^{-1} µm^{-1}	2.2	2	2.6	no data

[a]The lower and upper bounds are determined by using a 3% $\Delta\chi^2$ criterion.
[b]The value is determined from probing through the substrate side
[c]It is not a parameter used in the fit but is determined from the best-fit parameters α_0, $_0$ and f_0= 2.68 GHz. Acoustic pulse FWHM bandwidth: $[1.2, 6]$ GHz.

Table 4.4: Best-fit parameter values on 500 nm Au free-standing membrane

Parameter	Explanation	Unit	Best-fit-value	lb^1	ub^1	Reference-value
G	electron-phonon coupling strength	$10^{16}\mathrm{Wm^{-3}K^{-1}}$	2.49	2.25	2.5	2.1-4.0 [7, 11, 51, 113]
c_{l0}	longitudinal sound velocity	km/s	3.19	3.19	3.25	3.24 [112]
α_{l0}	attenuation prefactor	$\mathrm{GHz^{-2}}m^{-1}$ 1515	1024	2337	no data	
τ_l	phonon relaxation time	ps	55	42	75	no data
d	metal layer thickness	nm	491	488	528	500^2
$\alpha_l(f_0)^3$	attenuation at central frequency	10^{-1} µm^{-1}	2.2	2	2.6	no data

[a]The lower and upper bounds are determined by using a 3% $\Delta\chi^2$ criterion.
[b]The specified thickness may have a large uncertainty
[c]It is not a parameter used in the fit but is determined from the best-fit thermo-optic coefficient. Acoustic pulse central frequency $f_0 = 2.77$ GHz, FWHM bandwidth: $[1.3, 6]$ GHz.

Appendix

Solving the convolution

The solution to 4.7 in the main text, requires solving equations of the form

$$\sigma = -G(t) * \zeta \frac{\partial s}{\partial t}, \quad \text{with} \quad G(t) = \frac{1}{\tau} e^{-\frac{t}{\tau}} H(t) \tag{A.1}$$

To avoid a direct evaluation of the convolution, we define an auxiliary variable S satisfying

$$S = G(t) * s \tag{A.2}$$

Taking the time derivative on both sides of Equation (A.2) and using the relation $dH(t)/dt = \delta(t)$, one finds

$$\frac{\partial S}{\partial t} = \frac{1}{\tau}[-\frac{1}{\tau} e^{-\frac{t}{\tau}} H(t) * s + e^{-\frac{t}{\tau}} \delta(t) * s] = -\frac{S}{\tau} + \frac{s}{\tau} \tag{A.3}$$

With Equation (A.3), Equation (A.1) is equivalent to

$$\sigma = \zeta \frac{\partial (G * s)}{\partial t} = \zeta (\frac{S}{\tau} - \frac{s}{\tau}). \tag{A.4}$$

We can use Equation (A.4) for finding σ with S satisfying Equation (A.3). Therefore the convolution by solving an extra differential equation Equation (A.3) instead. This equation can be easily solved using finite different alongside the other equations of the model.

5

Ultrafast laser-induced guided elastic waves in a freestanding aluminum membrane

This chapter has been published in Phys. Rev. B 103, 064303 (2021) [31].

5.1. Introduction

Laser-induced high frequency (GHz-THz range) elastic waves (also referred to as acoustic waves or hypersound) in solids are extensively used in both industrial and academic research. In contrast to light, almost all solids are transparent to sound, including many optically opaque media. For this reason, many non-invasive methods for evaluating bulk materials based on laser-induced elastic excitations are established. Recent advanced applications include using elastic excitation for communicating with quantum systems [114–116], imaging buried nanostructures [117, 118], quantitative retrieval of phononic and mechanical properties [5, 86] and subsurface detection of alignment gratings for photolithography [96], and more.

Earlier studies on laser-induced elastic waves were mostly focused on the investigation of one dimensional propagation of excited longitudinal phonons [32, 34, 75–77, 80], which have yielded remarkable results about the phonon generation mechanism itself. Further progress in the field enables the generation and detection of shear phonons [29, 81, 119] and surface acoustic waves [29, 85, 87]. Among these more complex types of waves, Lamb waves are attracting increasing attention owing to their unique properties and potential for specialized applications. Lamb waves are guided acoustic wave modes existing in thin and freely suspended films [100]. The propagation behaviour of Lamb waves can be used for nondestructive characterization of thin films. One example is the zero-group-velocity modes where the group velocity of the Lamb wave vanishes, resulting in acoustic energy localization in the source region [28], offering reduced acoustic losses and enabling local material sensing and testing applications [120, 121].

The excitation of Lamb waves requires a component of the particle movement in the direction parallel to the free surface. In laser-ultrasonics, this is usually realized by either tightly focusing the excitation laser pulse [28, 122] or by employing nanostructured surfaces [123]. The dynamics of phonon evolution is then detected by a delayed probe pulse in a pump-probe configuration. Despite of the already established progress on laser generation and detection of Lamb waves, there is still a need for a comprehensive and detailed comparison between the measured signal and an advanced model describing dynamics over time scales spanning orders of magnitude. Furthermore, the role of thermal and acoustic contributions as well as different acoustic field components in the evolution of the signal shape and the evolution of the Lamb waves over propagation distance have not yet been fully

investigated. Acoustic attenuation of the Lamb waves is another important factor that is of practical importance, as it limits the interaction distance in various applications.

Here, we present a combined experimental and theoretical study on ultrafast laser-induced elastic waves in a thin, free-standing aluminum membrane. In our experiments we use tightly focused laser pulse to generate high-frequency Lamb waves. The optical response is probed at various locations with respect to the focused pump pulse. The measured signals are shown to be in excellent agreement with an advanced model we have developed earlier [5]. This combined experimental and theoretical approach allows us to address several key aspects of Lamb wave evolution: the separation of signal contribution due to different strain components, the thermo-optical effects, as well as quantitative determinations of acoustic propagation losses and the complex photoelastic coefficients. In addition, we present evidence of nonlinear propagation of the excited high-amplitude Lamb waves and show that acoustic nonlinearity can alter the measured signal shape.

The chapter is organized as follows: In Sec. 5.2 we discuss the experimental setup and the probe position-dependent measurements. In Sec. 5.3 we briefly discuss the model we developed earlier and its adaptation to the current experiment, as well as the fitting approach. In Sec. 5.4 we present the results and interpretations.

5.2. Position-dependent pump-probe measurements

A schematic of the experimental setup is shown in Fig. 5.1(a). The output of a Ti:Sapphire oscillator (Femtolasers XL500: wavelength centered at 800 nm, pulse duration 70 fs, repetition rate 5.1 MHz) is split in two beams with a 90:10 beam splitter. The beam with higher intensity is used to generate second harmonic (400 nm) of the fundamental wavelength using a β-barium borate (BBO) crystal. This converted 400 nm beam is used as the pump beam with a variable optical path length by using a mechanical translation stage (PI) as the optical delay line. This beam is focused by a microscope objective (Olympus LCPLN20XIR, x20, N.A. 0.45) onto the sample surface. The pump power after the objective is measured to be 5.5 mW. The beam with the fundamental wavelength (800 nm) is used as the probe beam. The probe beam is sent through a telescope system consisting of two lenses: L1 with a focal length of 100 mm and L2 with a focal length of 200 mm. The

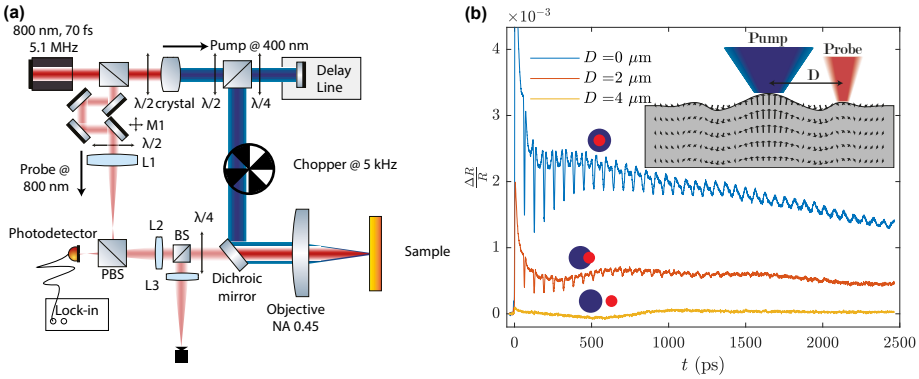

Figure 5.1: (a) Schematic of the experimental setup. The pump beam is tightly focused on the sample surface using a microscope objective. The probe beam is positioned at different distances D with respect to the pump beam. (b) Reflectivity changes measured on a 200 nm aluminum free-standing membrane, for different values of probe shift. The reflectivity changes are measured through a modulation of the dielectric constant via the photoelastic effect (Eq. 6.2). The inset in (b) illustrates the excitation of Lamb waves by the tightly focused pump beam, and its detection using a spatially shifted probe beam. The black arrows are the displacement vector of the excited Lamb waves (not to scale, only for illustrative purpose). The color circles illustrate the relative position of the focused pump (blue) and probe (red) beams for each measurement.

telescope system expands the beam such that it fills the entire objective aperture to form a diffraction limited probe spot. The mirror M1 in front of L1 is mounted on a two axes mirror mount, and is imaged onto the back-focal plane of the objective. By changing the angle of incidence of the beam on the lens L1, an area on the sample surface can be scanned by the probe beam, while leaving the pump beam position fixed [124]. We monitor the position of the probe spot on the sample using an imaging system composed by the objective and the L3 (f=200 mm) lens which projects an image of the sample plane into a CCD camera. With the camera we also measure the focal waist of the probe beam as $w_{probe} = 1.2\ \mu m$ at $1/e^2$ intensity. The physical pixel size of the camera is 2.2 μm, and with a magnification of 20x, we can determine probe center position with an accuracy close to 100 nm. With the CCD camera, we also measure the focused probe spot size versus the probe displacement. The probe spot size slightly increases as it is moved away from the pump spot. By fitting the probe spot image to a 2D Gaussian function, the maximum increase in spot radius is about 100 nm at the largest probing distance (5.5 μm). The size variations at shorter displacements are even smaller. Such small variations of the probe size are far below the spot size itself and estimated lateral acoustic wavelength. Therefore, its effect on

the measured signals is negligible. The probe light reflected by the sample is focused on a silicon photodiode (Thorlabs PDA100A2). The photodiode signal is sent to a lock-in amplifier referenced by the chopping wheel which modulates the pump beam at a frequency of 5 kHz. A calibration of the lock-in output signal allows to record the absolute reflectivity change.

The reflectivity changes are measured for a range of probing distances ($0 - 5.5\ \mu m$) on an aluminum free-standing membrane of 200 nm thickness. The maximum probing distance enables the detection of Lamb waves propagating away from the pumped region. Fig. 5.1(b) shows typical pump-probe traces measured at 3 different probing positions. For the zero probing position, a large and sharp peak is observed immediately after the pump excitation which is caused by an abrupt heating of the free electrons and lattices. This initial peak is not fully shown in the graph, to better visualize the acoustic signals that are more important for this work. Repetitive dips are observed after, which corresponds to an acoustic pulse bouncing back and forth in the free-standing membrane. Differences in the background shape are also observed for different probing positions. Detailed discussions and interpretation will be presented in the following sections.

5.3. Theory

5.3.1. The numerical model

In order to understand the signal formation and to interpret the measured data, we use the numerical model developed earlier in our group [5]. In the model we incorporate the physics of all the steps involved in a typical picosecond ultrasonics experiment, i.e., the generation, propagation and detection of the ultrasound waves. For the generation, we treat thermoelasticity as the dominant mechanism in metals [75, 76]. The evolution of the lattice temperature is modeled by the two-temperature model [70] with actual laser irradiation conditions as model inputs. For the sound propagation, we numerically solve the equation of motion for an isotropic elastic wave, with further incorporation of sound attenuation terms [5, 15, 97]:

$$\begin{aligned} \rho\frac{\partial^2\mathbf{u}}{\partial t^2} = \mu\nabla^2\mathbf{u} &+ (\mu+\lambda)\nabla(\nabla\cdot\mathbf{u}) + \nabla\sigma_{th} \\ &+ \xi\nabla^2\mathbf{v} + (\xi+\lambda_v)\nabla(\nabla\cdot\mathbf{v}), \end{aligned} \tag{5.1}$$

where σ_{th} is the thermal stress generated by the laser pulse, $\mathbf{u}$ is the displacement vector, ρ the mass density, λ and μ are the two Lamé parameters, $\mathbf{v}$ is the velocity vector, ξ the coefficient of shear viscosity and λ_v is linked to the coefficient of bulk viscosity η as $\lambda_v = \eta - 2\xi/3$. The thermal stress σ_{th} is coupled to the generation step of the model through thermoelasticity.

Eq. 6.1 is solved by the finite-difference time-domain (FDTD) method [17] in a two-dimensional (2D) geometry with the incorporation of proper boundary conditions. For the front and back surfaces of the membrane, a free boundary condition is implemented which requires the total stress at the air-metal interface to vanish. For the two lateral boundaries, perfectly matched layers (PMLs) [98] are implemented to absorb nonphysical reflections from the edges of the numerical grid. By solving Eq. 6.1, the two strain components s_x and s_y as well as the shear strain s_{xy} can be obtained [5]. Here, x refers to the axis perpendicular to the sample surface while y refers to the axis parallel to it. Having those strain components, the change in the electric permittivity tensor can be evaluated, provided that the photoelastic tensor is known. Here we assume the material is isotropic, thus the photoelastic tensor has only two unknowns, P_{11}, P_{12} and $P_{44} = (P_{11} - P_{12})/2$ [81]. The probe beam at our photodetector position is linearly polarized, thus we only have to consider the y component of the electric field of the probe beam. Under these assumptions the change in the permittivity tensor elements are:

$$\Delta\epsilon_{yy} = -\epsilon_r^2(P_{11}s_y + P_{12}s_x); \Delta\epsilon_{xy} = -\epsilon_r^2 P_{44}s_{xy}, \tag{5.2}$$

where ϵ_r is the dielectric constant of aluminum in the unperturbed state. In our data analysis we have found that including $\Delta\epsilon_{xy}$ does not result in a better model fit through the measured data, indicating its negligible contribution. Thus, in the following analysis, $\Delta\epsilon_{xy} = 0$.

Having the value of the permittivity change, the reflectivity change can be calculated by solving the Maxwell's equations for the probe pulse. In this work, the transform matrix method [99] is used, which also takes into account the permittivity gradient along the propagation direction of the probe pulse.

5.3.2. Least-squares fitting the measured data

The model described in the previous section is used to fit the measured data using the least-squares algorithm. Material properties such as the electron-

phonon coupling constant, thermo-optic coefficient, photoelastic coefficients P_{11} and P_{12}, acoustic attenuation coefficient, as well as membrane thickness are treated as fitting parameters. The longitudinal speed of sound in aluminum is fixed as $c_l = 6420$ m/s [112] during the fitting. The focal beam waist of the probe beam is measured as $w_{probe} = 1.2\ \mu m$. The measured signal at different probing positions can be seen as a convolution of the probe beam with the response function induced by the pump beam, which already contains information about the size of the focused pump beam. Therefore, the focal beam waist of the pump beam is treated as an extra fitting parameter. Other parameters used in the model are either taken from known literature values or estimated from experimental conditions.

5.4. Results and Discussion

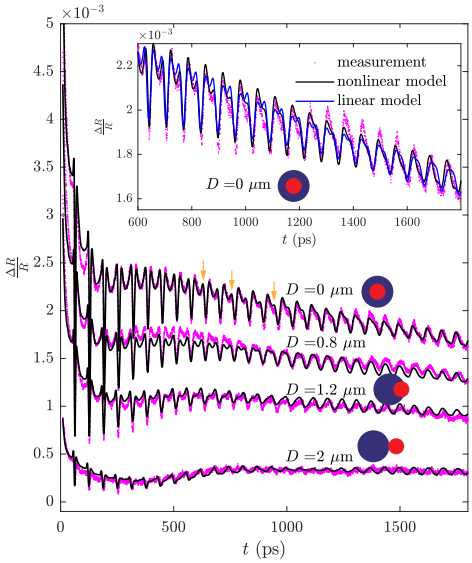

Figure 5.2: Measured reflectivity change at four probe positions (magenta dots) and corresponding model fit (black lines) on an aluminum free-standing membrane of 200 nm thickness. The inset shows the comparison between a linear acoustic model (blue line) and a nonlinear acoustic model (black line).

Measurements were performed on a 200 nm thick aluminum free-standing membrane for probing distances from 0 m to 5.5 m in 0.5 m steps. These values refer to the distances from the center of the focused probe beam to the center of the focused pump beam. The values are determined from the

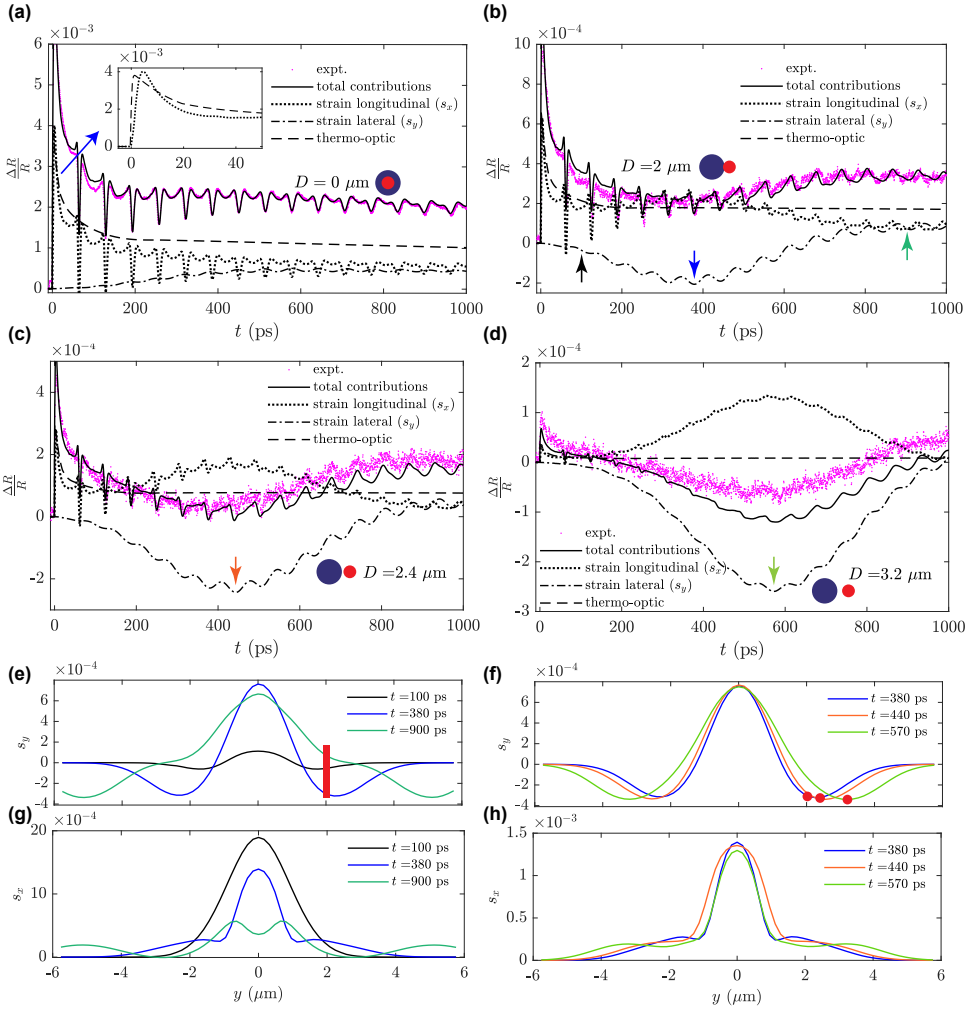

Figure 5.3: Measured reflectivity change (magenta dots) and model calculated reflectivity change (black solid lines) at (a) 0 μm, (b) 2 μm, (c) 2.4 μm and (d) 3.2 μm probing positions. The dotted lines, dash-dotted lines and dashed lines are reflectivity changes from each contribution: the longitudinal strain (s_x) contribution, the lateral strain (s_y) contribution and the lattice temperature contribution (thermo-optic). The strain profiles along the membrane surface at multiple time delays are shown in (e-h), separated in the strain components s_y (e,f) and s_x (g,h). The displayed time delays correspond to the colored arrows in (b-d). The red bar in (e) illustrates the probing position of 2 m. The red filled circles in (f) illustrate the three probing positions. See also Video 1 in the Supplemental Material of [31].

recorded probe spot images during the measurement. In the data analysis we found that the best match between the measured data and simulations, especially the determined lateral propagation speed of the Lamb waves, were found when a scaling factor of 0.8 was applied to these values of probing distance. This is likely due to the uncertainty in the determination of the magnification factor of our imaging system, limiting the accuracy of the determination of the probing positions. We therefore applied this scaling to the probing distances to use as both model inputs for fitting the data and the presentation of the final results. We note that the scaling does not change the interpretation of the results. We use the model to fit the measured data at 0 μm, 0.8 μm, 1.2 μm and 2 μm probe positions (after applying the scaling factor). The best-fit results are shown in Fig. 5.2. The agreement with the measured data is excellent. In the fit we minimize the combined residual of the measurements at these four probing positions. The calculated signals at all probe positions share the same group of best-fit parameters except for the probing position used for that calculation. The best-fit parameters are shown in Table. 5.1 at the end of the chapter. It is worth noting that in Ref. [30] only the ratio between the real part and the imaginary part of the photoelastic constants are given, while our result yields not only the ratio but also the amplitudes of the two photoelastic constants P_{11} and P_{12}. This is achieved by calibrating the absolute reflectivity change and by separating different contributions to the measured signals. The measured signals can be well-explained by the combined effects of three contributions: the refractive index change induced by the two strain components s_x, s_y and the thermo-optic effect. In Fig. 5.3(a)-5.3(d) we plot the resulting reflectivity changes calculated by each of those contributions alone. The total signal is a coherent sum of the electric field variations due to the individual contributions, rather than a direct sum of the reflectivities. The signal during the first 50 ps (inset of Fig. 5.3(a)) is dominated by the combined effects due to the mass density change and the lattice temperature change. The thermal stress introduced by the laser pulse produces a non-propagating part of the strain component, leading to a rapid increase of the density in the vicinity of the illuminated surface, followed by its slowly recovery towards the room temperature value. This density change is accompanied by the temperature change which shows the rapid increase and the slowly recovery as well. Although these two effects always accompany each other, they contribute to the measured signal by a different amount through the difference between the photoelastic constant and the thermo-optic coefficient. For probing at 800 nm wavelength on aluminum, the thermo-optic effect is expected to be large as the probe wavelength coincides with the peak of its thermoreflectance spectrum [101].

The magnitude of these two contributions are quite similar, yet their signal shapes show slight differences: the increase of the thermo-optic contribution is more abrupt while the strain contribution takes more time to develop. This is to be expected as the strain develops after the temperature increase and requires coherent motion of the lattice. The difference in their signal shapes indicates that separating these two contributions by fitting their combined effect is possible. In fact, excluding the thermo-optic effect in the fit significantly increases the fitting residual. The best-fit thermoreflectance is smaller than the reference value. This may be caused by an overestimation of the incident pump fluence, but another possibility for this discrepancy is cumulative heating due to the high repetition rate of the laser system. This heating increases the steady-state sample temperature, which causes us to extract a thermoreflectance that deviates from its room-temperature value. The effect of this steady-state temperature rise on our signals can be seen at the negative delay-times, which is around 1.2×10^{-3}. We note that this steady-state signal only introduces a constant offset to our data, which does not affect the acoustic dynamics. To compare with the model, this offset is subtracted from the total signal.

The signal after 50 ps is dominated by acoustic dynamics. The thermo-optic effect and the non-propagating strain contribution are still present, but they contribute to the measured signal in the form of a quasi-DC background. The slope of this background is determined by long-term heat dissipation and relaxation of the surface strain. The repetitive dips with a period of ~ 64 ps are caused by the propagation and internal reflection of the longitudinal strain component s_x. The period of these longitudinal echoes equals to one round-trip time of the acoustic pulse. In Fig. 5.3(a) we see the broadening and damping of the longitudinal echoes. This is caused by the combined effect of acoustic attenuation and diffraction. In the model we assume a frequency-dependent acoustic attenuation which is proportional to the square of the acoustic frequency [5]: $\alpha_l(\omega) = \alpha_{l0}\omega^2$. The attenuation coefficient α_{l0} is treated as a fitting parameter which yields the value $\alpha_{l0} = 3.51$ GHz^{-2}m^{-1}. The quadratic dependence indicates more attenuation for higher frequencies, effectively broadening the acoustic pulse. At this stage we can not completely rule out the possibility of interface scattering loss to the attenuation of the acoustic pulse. However, the microscopic roughness at the metal/air interface is expected to be much finer than the acoustic wavelength, thus scattering loss at our frequency range is expected to be small. The diffraction of the longitudinal acoustic wave also broadens the echo. The acoustic diffraction produces off-axis propagation with a slight angle which effectively dissipates

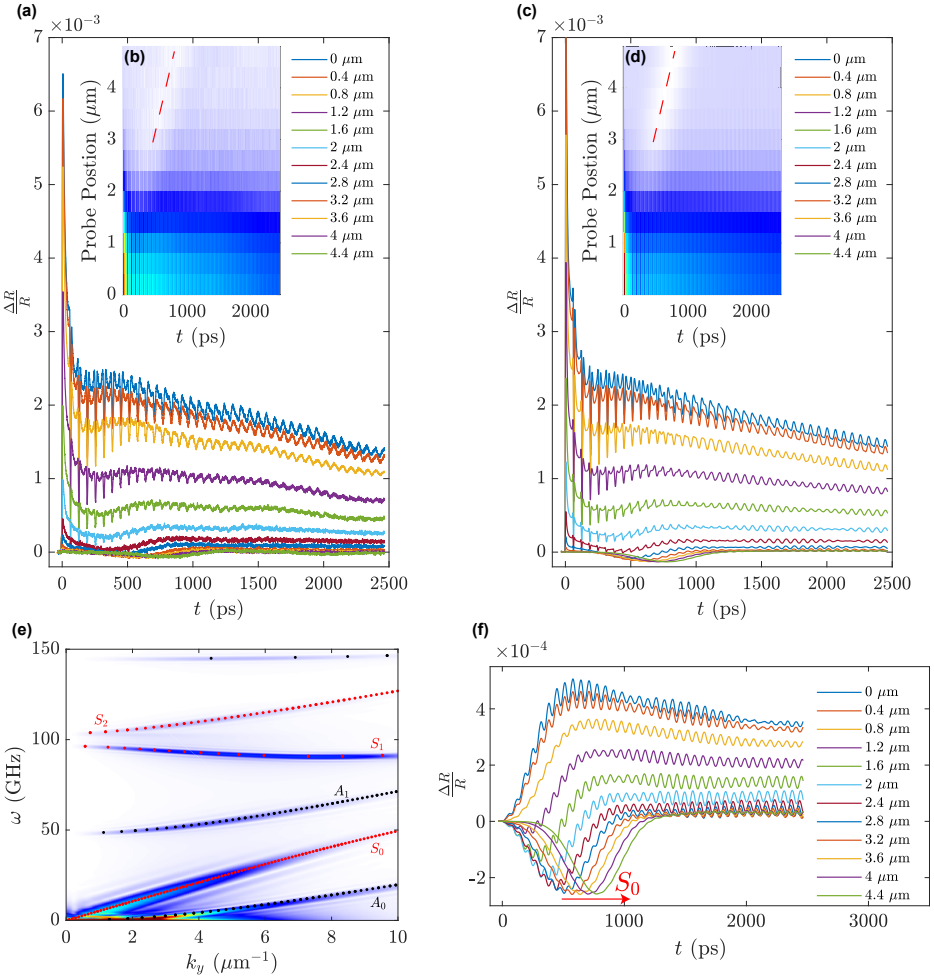

Figure 5.4: Measured (a,b) and calculated (c,d) reflectivity changes at all probing positions. The red dashed lines in (b,d) highlight the contribution from the lateral propagation of the Lamb waves. In (b,d), red and green represent higher values while blue and white represent lower values. The Lamb wave dispersion relation retrieved from the simulation is shown in (e) as a colored plot. The black and red dots in (e) are solutions of the analytical expression of Lamb wave dispersion relations. The black dots correspond to the asymmetric modes and the red dots to the symmetric modes. The calculated reflectivity contribution from the s_y component is shown in (f), where the red arrow illustrates the propagation of the S_0 Lamb mode.

the energy and elongates the echo.

A striking aspect is the increase in the contribution of the lateral strain component (s_y), which, at zero probing position, gradually reaches its maximum at ~ 600 ps. The tightly focused pump beam means that the effect of acoustic diffraction and the redistribution of acoustic energy from longitudinal strain (s_x) to lateral strain (s_y) significantly changes the signal shape and thus can be measured. If the contribution of s_y only slightly changes the signal shape measured at zero probing position, its contribution becomes increasingly important and dominates the overall background shape at large off-center probing positions. In Fig. 5.3(b)-5.3(d) we plot the measured signal at three off-center probing positions and the separation of contributions by the model calculations. One interesting observation is the initial decrease and the follow-up increase of the background signal, forming broad dips for these off-center positions. By looking at the s_x contribution, such a broad dip is absent for $D = 2\ \mu m$. For $D = 2.4\ \mu m$ and $D = 3.2\ \mu m$, the s_x contribution does show a broad peak at the correct timing, however, it is of the opposite sign to the measurements. On the contrary, the s_y contribution remarkably reproduces both the timing and the sign of these broad dips. The s_y contribution goes even to negative and back to positive again. The off-center probe measures the 'passing-by' of the Lamb waves traveling in the lateral direction. In Figs. 5.3(e) and 5.3(f) we show the lateral strain (s_y) profiles along the surface of the membrane at selected time instants corresponding to the center of these broad dips. At $t = 100$ ps, the surface wave is just generated at the edges of the pump spot. At later times, the surface wave is fully formed and starts to propagate outward from the pumped region. The leading part of this wave is negative in s_y, while positive in its trailing part. The off-center probing positions therefore undergo relatively slow compressions followed by expansions caused by the 'passing-by' of the lateral strain component. In Figs. 5.3(g) and 5.3(h) we show the longitudinal strain (s_x) profiles at the same time instants. The s_x at these timings are all positive, partially cancel out the reflectivity changes from the s_y component. The slight disagreement in the amplitude of the broad dip in Fig. 5.3(d) is expected to be caused by geometrical diverging effect. For a diverging guided (propagating) acoustic wave spreading from a point source in a two dimensional space as in the experiment, the wave energy is spread out over the cylindrical surface area $2\pi rh$, where r is the distance from the wave front to the point source, and h is the membrane thickness. Because of energy conservation, this leads to a $1/r$ decay rate for the wave intensity. Since for a propagating acoustic wave, the intensity is proportional

to the wave amplitude squared [125, 126], it translates to a $1/\sqrt{r}$ law for the wave amplitude. This geometrical diverging effect is absent in the 2D simulations. The diverging effect can be ignored inside the source region, the size of which can be estimated as equal to our focused pump beam size ($\approx 2w_{pump} = 3.6\ \mu m$). For probing positions within this range, especially for Figs. 5.3 (a)-5.3(c), the diverging effect is minimum and can be neglected.

Figs. 5.4(a) and 5.4(c) show the measured and the calculated reflectivity changes at all probing positions. These calculations are obtained by using the same best-fit parameters that are determined earlier. The magnitude, evolution of the acoustic echoes, as well as changes in the background signal are well-reproduced by the simulations. In Figs. 5.4(b) and 5.4(d), the reflectivity changes at all probing positions and time-delays are plotted as two dimensional color plots. In both measured and calculated data, a white band with oblique orientation is clearly observed (marked by red dashed lines). This white band is a result of lateral propagation of one of the Lamb wave modes, which, owing to the s_y strain component, decreases the reflectivity as the Lamb wave passes by the probing position. This is illustrated in Fig. 5.4(f), where the contribution to the reflectivity due to s_y component is separated. Its negative contribution to the reflectivity and its lateral propagation are clearly seen. From the slopes of the white band in Fig. 5.4(b) and 5.4(d), a very similar lateral propagation speed of ~ 5600 m/s is determined. To determine the Lamb wave modes, we retrieve the dispersion relation by a spatiotemporal Fourier transform of the simulated strain field. The results is shown in Fig. 5.4(e) and compared with the analytical solution of Lamb wave dispersion relations [100, 125]. From the dispersion relation we determine the phase velocity of the S_0 symmetric mode to be ~ 5300 m/s, in good agreement with the retrieved lateral propagation speed from Figs. 5.4(b) and 5.4(d). We can also observe that the group velocity of the S_0 mode is very similar to its phase velocity, suggesting small dispersions for this mode. The agreement on the propagation speed indicates that the broad dips in the signal probed at large off-center positions, and thus the white bands observed in Figs. 5.4(b) and 5.4(d) are caused primarily by an excitation of the S_0 symmetric Lamb mode. The excitation of Lamb waves requires a component of particle movement in the direction parallel to the surface. In our case this is primarily caused by acoustic diffraction and mode conversion: The tight focusing condition in our experiment results in the generation of a localized acoustic field directly after the excitation. The localization gives rise to a nonzero gradient parallel to the surface in the acoustic field, causing particle movements parallel to the surface because of acoustic diffraction. Another

cause of the Lamb wave generation is mode conversion (longitudinal to Lamb modes): due to acoustic diffraction, part of the longitudinal wave arrives at the surface at an oblique angle, causing particle movement along the surface and converting some of its energy into Lamb waves [5]. A secondary cause is the nonzero gradient in the thermal stress along the surface direction, which can directly facilitate parallel particle movements. In pump-probe experiments using a conventional geometry, i.e., a large pump spot and a small probe spot, the lateral dynamics or Lamb waves are expected to have negligible or minor contributions to the signals. The gradient in the temperature and the acoustic field in the forward direction is usually quite large in metals due to a shallow light-penetration depth and limited thermal energy diffusion because of high electron-phonon coupling strength. For the lateral dynamics to significantly change the measured signals, the pump beam needs to be tightly focused. Our simulations with a variety of pump spot sizes show that the lateral dynamics only significantly influences the signal shape when the pump spot radius is smaller than 1 or 2 micrometers.

Several aspects of the data analysis need to be further addressed. First, in the calculations, two aluminum oxide (Al_2O_3) layers with a thickness of 6 nm on both sides of the free membrane are included. Ellipsometry measurement on the sample confirms the present of 6 nm thick oxide layers. Second, the heat dissipation is expected to be caused by heat diffusion in all lateral directions. However, our 2D simulation results in a slower decay than what is observed in the experiment. To correct for this, we introduced an extra heat loss term in the lattice temperature equation of the two-temperature model. This term is in the form of $-(1/\tau)[C_l(T_l - T_0)]$, where C_l is the lattice heat capacity, T_l is the lattice temperature and $T_0 = 300$ K is the environmental temperature. The parameter τ determines the rate of heat dissipation away from the pumped area, and it is treated as a fitting parameter. The best-fit τ is 5.2 ns. We note that this term does not change the simulated acoustic dynamics. Third, we find that adding acoustic nonlinearity in the calculations significantly improves the agreement between the measured and calculated signals. A comparison between the best-fit results using a linear acoustic model and a nonlinear acoustic model at zero probing position is shown in the inset of Fig. 5.2. The nonlinear model reproduces better the sawtooth signal shape especially observed at longer time delays. Acoustic nonlinearity is incorporated into the model by adding a second-order term in the strain-stress relation [5]: $\sigma_x = -(\lambda + 2\mu)s_x - \lambda s_y + (\gamma/4)s_x^2$. The best-fit nonlinearity constant γ is found to be 1.2×10^{13} Pa.

Our 2D nonlinear model shows the formation of sawtooth-like temporal shapes. However, due to the complexity of the model, the point-source excitation, and the combined influence of several physical effects, an intuitive picture explaining the formation of such signal shapes is not readily obtained. To better show the influence of nonlinear effects, we study a simpler system which qualitatively shows the same nonlinear dynamics. Here we simulate the nonlinear propagation of a 1D strain in a 200 nm aluminium free-standing membrane. The strain pulse is launched in the simulation by a hypothetical source: we assume that the temperature of the surface layer of the membrane is increased by 40 K, with a rising time of 5 ps. The surface expansion caused by this swift temperature increase generates a strain pulse propagating into the interior of the membrane. A schematic of the simulation scheme is shown in the inset of Fig. 5.5(a). The temperature in the heated layer follows an exponential decay with a characteristic length of 20 nm. This heat source is much more localized to the membrane surface than that in the experiment. This strongly localized heating ensures a narrow spatial extent of the resulting strain pulse. This gives rise to well-separated echoes, and facilitates the observation of propagation-related effects. In Fig. 5.5(a), we plot the strain s_x at 5 nm below the excitation surface, as a function of time, for both linear and nonlinear propagations. These traces show the time evolutions of the generated strain as it undergoes multiple round-trips in the membrane. For the simulation of nonlinear propagation, as mentioned before, an additional second order term is added to the strain-stress relation: $\sigma_x = -(\lambda + 2\mu)s_x + (\gamma/4)s_x^2$. This relation implies that the atoms in the lattice experience a nonlinear restoring force upon displacement from equilibrium. While symmetric echoes are observed for the linear case, the nonlinear propagation gives rise to increasing asymmetry. As marked by the yellow arrows, the first crest of the echo gradually diminishes, while the second crest seems to grow, as more propagation distance and internal reflections are accumulated. Despite the simplicity of this 1D nonlinear propagation model, the reduction of the first crest can be seen in the experimental data as well, as marked by the yellow arrows in Fig. 5.2. Because the echoes are not well separated in the actual experiment, the changing heights of these first and second crests give rise to the observed sawtooth-like signals. The asymmetry in the nonlinear echo originates from the asymmetry in the nonlinear strain-stress relation. The sign of the nonlinearity constant determines the direction of this asymmetry, i.e. whether the first or the second crest would become stronger.

These changes in echo shapes result from a strain-dependent propagation

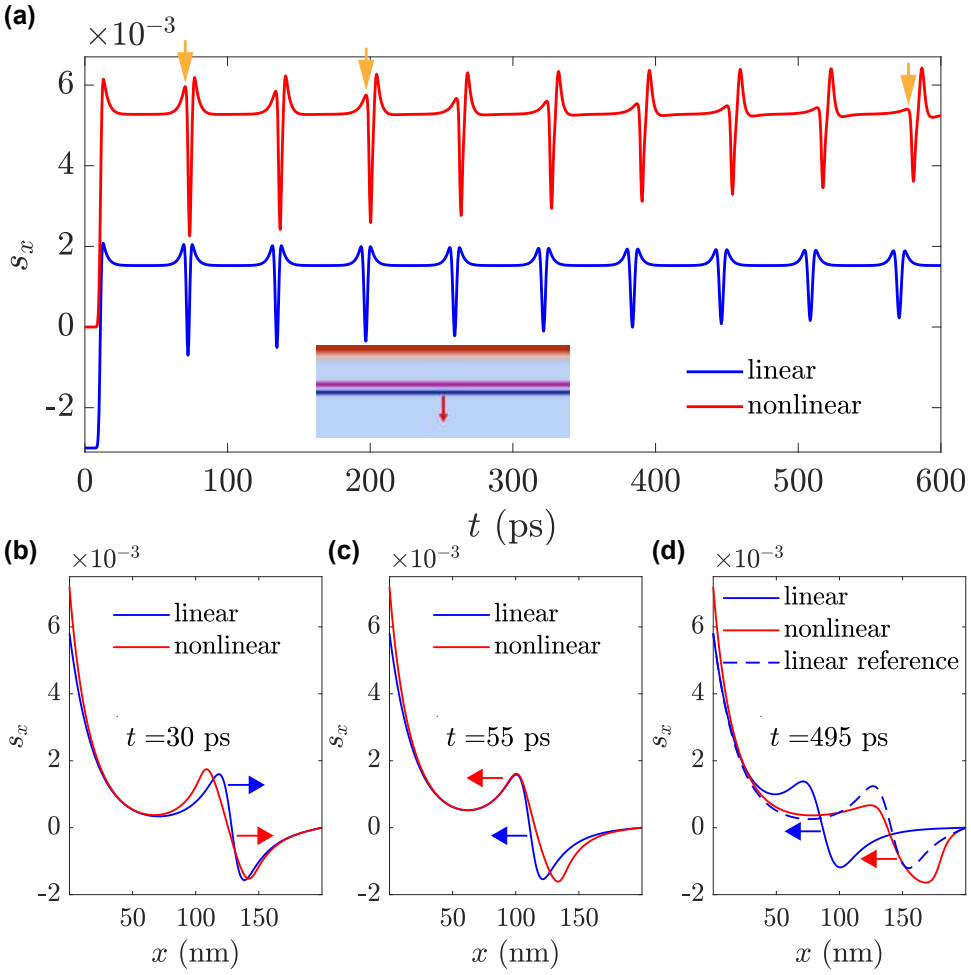

Figure 5.5: Nonlinear propagation of a 1D strain pulse. (a) The returned strain at the location close to the membrane front surface (5 nm beneath the surface), as a function of time, for linear (blue line) and nonlinear (red line) propagations. The blue line has a vertical offset of -3×10^{-3} for clarity. The yellow arrows in (a) shows the diminishing of the first crest of the echoes in the nonlinear case. The inset in (a) shows a schematic of the simulation scheme, in which the topmost layers of the membrane are heated and a strain pulse is launched into the interior. The red layer illustrates the temperature distribution, while the pink and blue area illustrate the positive and negative parts of the generated strain. (b-d) The strain profiles inside the membrane, at different time instants, for linear (blue lines) and nonlinear (red lines) propagations. The red and blue arrows indicate the propagation directions of the strain pulse. The blue dashed line in (d) is the linear strain offset in position to overlap with the nonlinear strain profile for reference. See also Video 2 in the Supplemental Material of [31].

velocity combined with the phase reversal upon reflection at the free surface. From the nonlinear strain-stress relation we can define an effective speed of sound through $-\rho_0 c_{eff}^2 s_x = -\rho_0 c_l^2 s_x + (\gamma/4) s_x^2$, which gives

$$c_{eff}^2 = c_l^2 - \frac{\gamma}{4\rho_0} s_x, \tag{5.3}$$

where c_l is the speed of sound in the absent of nonlinearity. The effect of this strain-dependent velocity upon propagation is shown in Figs. 5(b-d). An additional complicating factor is the reflection at free surfaces: Fig. 5(c) shows a strain pulse after reflection at the back surface, where a sign reversal has occurred due to the impedance mismatch between aluminum and air. As a result, the velocity of the leading and trailing parts of the strain profile will have changed after such a reflection, further complicating the profile distortion. The calculation shows a significant reshaping of the propagating strain pulse after several round-trips, as shown in Fig. 5.5(d) by the red trace.

The above analysis of the nonlinear effects is based on a simplified 1D picture. In our experiment, the signal change due to the nonlinear effect may be affected by other factors, such as a larger spatial extent of the generated strain, acoustic diffraction due to the localized excitation volume, the contribution of different acoustic field components, etc. Although it is difficult to separate the effect of each of these contributions on the nonlinear strain propagation, these effects are included in our 2D simulations.

5.5. Summary

Lamb waves are excited in a thin, free-standing aluminum membrane by a tightly focused fs laser beam. The optical response caused by the excitation is measured at a range of probing positions around the excitation region by delayed probe pulses. The measured reflectivity changes at all positions and time-delays are compared with the calculations by using a 2D numerical model. Excellent agreements between measurements and calculations were found. This combined approach allows the separation of contributions to the measured signals, as well as the role of different strain components on the signal formations, which have not been clearly elaborated in previous studies. It has been shown that the measured signal is a combination of several contributions: the thermo-optic contribution, the strain-optic contribution due to longitudinal and lateral strains. The off-center probe registers the lateral propagation of the excited Lamb waves, which is identified as the S_0 sym-

metric Lamb mode by comparing with simulations. Besides, the excellent model fit to the measured signals allows to retrieve quantitative information on several parameters, such as the two complex photoelastic coefficients and the acoustic attenuation coefficient. Furthermore, evidence of acoustic nonlinearity in the excited Lamb waves was found and a nonlinearity constant is extracted.

Table 5.1: Best-fit parameters on 200 nm Al free-standing membrane

Parameter	Explanation	Unit	Best-fit-value	Reference-value
d	membrane thickness (exclude oxide layers)	nm	183	200
G	electron-phonon coupling constant	$10^{17}\mathrm{Wm^{-3}K^{-1}}$	2.92	2.46 [11]
α_{l0}	longitudinal acoustic attenuation coefficient	$\mathrm{GHz^{-2}m^{-1}}$	3.51	not available
$\frac{\partial n}{\partial T}$	thermo-optic coefficient, real part	$-1\times10^{-3}\mathrm{K^{-1}}$	0.59	2.96–4.08[1]
$\frac{\partial \kappa}{\partial T}$	thermo-optic coefficient, imaginary part	$10^{-3}\mathrm{K^{-1}}$	0.81	0.4–4.4[1]
P_{11}	complex photoelastic constant	dimensionless	-0.060+0.031i	-10+5i [30][2]
P_{12}	complex photoelastic constant	dimensionless	-0.17-0.012i	-10-1i [30][2]
w_{pump}	pump radius ($1/e^2$)	μm	1.8	not applicable
$\frac{dR}{RdT}$ [3]	thermoreflectance @ 800 nm	$10^{-4}\mathrm{K^{-1}}$	0.49	1.14–2.4 [101–103]

[a]The reference value on thermo-optic coefficient are determined by the optical conductivity data at varies temperatures in Ref. [104] together with available thermoreflectance data in Ref. [101–103].
[b]In Ref. [30],the amplitude is arbitrary, only the ratio is relevant.
[c]Calculated from the best-fit thermo-optic coefficient.

6

Amplifying detection of laser-excited strain waves via transparent nanolayers

This chapter has been published as part of Phys. Rev. B **104**, 205416 (2021) [127]

6.1. Introduction

Ultrafast laser generation and detection of acoustic waves in solids have attracted increasing attention in recent decades. Thomsen *et al.* have first shown that the absorption of a short light pulse by a solid can lead to the generation of an extremely short stress pulse [75]. The absorption of an ultrafast laser pulse by a solid can induce a material heating rate that is only limited by the fundamental electron-phonon coupling process. With this ultrafast heating rate, it is possible to generate acoustic frequencies of hundreds of gigahertz (hypersound). The frequencies of the sound waves are so high that this so-called picosecond ultrasonics technique is of great scientific value and shows great promise for a number of applications. Examples include nonlinear acoustics and solitons [77, 94, 117, 128], acoustic focusing and shock waves [119, 129], as well as laser-induced sound waves for imaging of buried nanostructures [117, 118, 130] and the detection of sub-surface alignment gratings in photolithography [96, 131].

Excitation and detection of strain waves in photoacoustics can be realized by pumping the solid with a pump pulse and detecting its optical response by a time-delayed probe pulse: the pump pulse excites a strain pulse propagating into the solid and where it can be scattered/reflected back to an interface where its disturbance to the optical properties of the solid is detected by the probe pulse. Such an interface is usually a free surface, forming the solid/air boundary. It is well known that the total stress vanishes at free surfaces [75, 132]. This implies a local variation in the acoustic field caused by a change of boundary condition, making the properties of acoustic waves and their interactions with the probing light near the free surface of prime importance for their detection. Although such free surfaces are routinely encountered in experiments adopting all-optical generation and detection of acoustic waves, the implications of a free surface on the detection of the acoustic waves, to the authors' knowledge, have never been examined either theoretically or experimentally. In this chapter, we present both experimental and theoretical evidence that the presence of a free surface has a profound influence on the detection of the strain waves. In our experiments, we use specially designed samples to separate the effect of the free surface on the strain detection. The discovered effect is further confirmed by comparing the measurements to an advanced numerical model that we have developed earlier [5] with the implementation of free-boundary conditions, showing excellent agreement to the measured data. This work elaborates a key aspect in the detection of strain waves at free surfaces by optical means and can

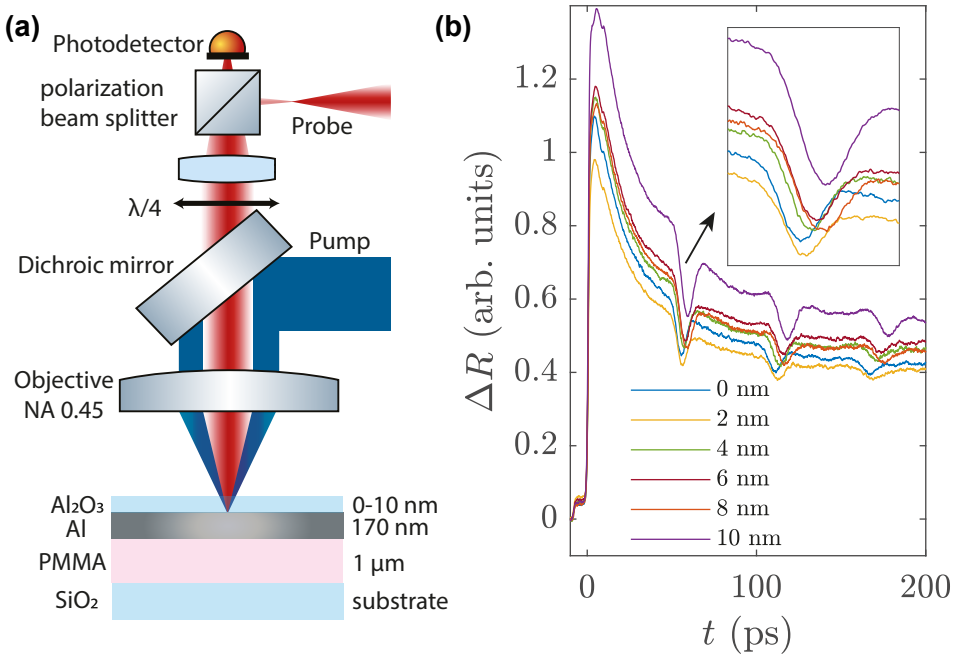

Figure 6.1: (a) Simplified schematic of the experimental setup. The pump and probe beams are focused on the surface of the aluminum layer through the Al_2O_3 layer by a microscope objective. The dichroic mirror ensures that only the reflected probe beam can reach the photodetector. Samples with Al_2O_3 layers of different thicknesses (nominal values of $0-10$ nm) are used for the experiment. The obtained signal is proportional to the reflectivity change. The measured signals (in arbitrary units) in these samples are shown in (b). The inset in (b) is a magnified plot around the first echo.

lead to new strategies for signal enhancing and quantitative characterization of multi-layer systems using laser-excited acoustic waves.

6.2. Experimental setup and samples

Our experiments are based on an ultrafast pump-probe setup originally developed for high resolution acoustic imaging [31, 130]. The experiments are performed on thin aluminum films with a transparent dielectric layer deposited on top of it with various thicknesses. The dielectric layer repositions the free surface from the metal/air interface to the dielectric/air in-

terface. Thanks to the transparency of the dielectric layer, the probe pulse measures the reflectivity variation always at the metal surface, irrespective of the dielectric layer thickness. By probing through different thicknesses of the transparent layer, the effect of the free surface on the strain detection can be isolated and systematically studied. A simplified schematic of the setup and the layered samples used in the experiments are shown in Fig. 6.1(a). The pump and probe beams are focused on the surface of the aluminum layer, through the transparent Al_2O_3 layer. The probe light reflected by the sample is focused on a silicon photodiode (Thorlabs PDA100A2). The generated signal is sent to a lock-in amplifier to increase the signal to noise ratio. The samples used in the experiments were fabricated on glass coverslips (borosilicate 170 μm). A 1 μm thick Poly(methyl methacrylate) (PMMA) layer was first deposited on the coverslip by spin-coating. The PMMA layer serves to increase the acoustic impedance mismatch at the rear side of the aluminum layer to increase the strength of the reflected strain wave for better detection. The PMMA layer is thick enough to ensure that no acoustic echo from the PMMA/substrate interface be detected in our time-window of interest. Both the aluminum layer and the Al_2O_3 layer were deposited last by electron beam physical vapor deposition (E-Flex, Polyteknik). The thickness of the aluminum layer is kept constant for all samples. Al_2O_3 layers of various thicknesses ($0, 2, 4, 6, 8, 10$ nm by nominal values) were deposited on top of the aluminum layers.

6.3. Theoretical modelling

In order to understand the echo amplification observed in our measured signals, we simulate the experiments by using an advanced numerical model we have developed [5]. The model includes all relevant physics of the generation, propagation and detection of strain waves in metals by ultrafast laser pulses, with the implementation of free boundary conditions.
In the generation part, we calculate the lattice temperature elevation by the absorption of the laser pulse, which is used as a source term in solving the following equation of motion for the acoustic wave [5, 15, 97]:

$$\begin{aligned} \rho\frac{\partial^2\mathbf{u}}{\partial t^2} = \mu\nabla^2\mathbf{u} &+ (\mu+\lambda)\nabla(\nabla\cdot\mathbf{u}) + \nabla\sigma_{th} \\ &+ \xi\nabla^2\mathbf{v} + (\xi+\lambda_v)\nabla(\nabla\cdot\mathbf{v}), \end{aligned} \tag{6.1}$$

where σ_{th} is the thermal stress generated by the laser pulse, $\mathbf{u}$ is the displacement vector, ρ the mass density, λ and μ are the two Lamé parameters,

$\mathbf{v}$ is the velocity vector, ξ the coefficient of shear viscosity and λ_v is linked to the coefficient of bulk viscosity η through $\lambda_v = \eta - 2\xi/3$. The thermal stress σ_{th} is modeled through thermoelasticity [75, 76] as $\sigma_{th} = -3B\beta\Delta T_l$, where B is the bulk modulus, β is the linear expansion coefficient, and ΔT_l is the increase of lattice temperature calculated in the generation step of the model. The third step is to calculate the reflectivity change. For this, we relate the change of dielectric constant to the generated strain by the photoelastic effect [81]:

$$\Delta\epsilon = -\epsilon_r^2 P_{12} s_x, \tag{6.2}$$

where ϵ_r is the dielectric constant of aluminum in the unperturbed state, P_{12} is the complex photoelastic constant for longitudinal waves, and s_x is the longitudinal volumetric strain. Throughout the chapter, x represents the axis perpendicular to the sample surface while y represents the axis parallel to it. Having determined the value of the dielectric constant change, the reflectivity change is calculated by solving Maxwell's equations for the probe pulse. More details on the model can be found in Refs. [5, 31]. In the calculation of the dielectric function (Eq. 6.2), we have neglected the contributions to the reflectivity change from the shear (s_{xy}) and the lateral (s_y) strains [31], leaving only the contribution of s_x to be included. This is justified by comparing the result to a calculation with those contributions included, which shows nearly identical ($< 1\%$ variation) reflectivity change, for the first two echoes.

Eq. 6.1 is solved by the Finite-Difference Time-Domain (FDTD) method with the incorporation of free-boundary conditions. We use the model to fit the measured data shown in Fig. 6.2(a). In the fit, we minimize the combined residual of the measurements on all samples. The electron-phonon coupling constant determines the rate of electron-phonon energy exchange, thus, it influences the frequencies of the generated strain pulse [5, 31]. It is known that for aluminum, the thermo-optic effect has a strong influence on the background signal [5, 31], as the 800 nm probe wavelength coincides with the peak of aluminum's thermoreflectance spectrum [101]. The value of photoelastic constant P_{12} influences the observed echo shape. Therefore, these parameters are treated as fitting parameters. For P_{12}, we use our determined value $P_{12} = -0.17 - 0.012i$ [31] from previous experiments on aluminum, keeping the ratio of the real and imaginary parts unchanged and only allowing its amplitude to slightly change in the fit. The longitudinal speed of sound in aluminum $c_l = 6420$ m/s [112] and experimental conditions such as the pump fluence (90 J/m^2) are fixed during the fit.

6.4. Observation of echo amplification

Fig. 6.1(b) shows the raw signals measured on these samples. A large and sharp peak is observed immediately after the arrival of the pump pulse which is caused by a swift heating of the free electrons and subsequent heating of the lattice via electron-phonon coupling. Repetitive acoustic echoes are observed, which results from the propagation and reflection of the excited strain pulse in the $Al_2O_3 - Al$ bilayer system. The diminishing of the echo signal after several acoustic roundtrips is mainly due to acoustic transmission to the PMMA layer and propagation losses.

The magnitude of the aforementioned electron peak and the overall signal strength vary among samples, with a tendency to be larger for samples with a thicker Al_2O_3 layer. This tendency can be explained by the difference in the pump beam reflectivities: the sample with a thicker Al_2O_3 layer has a smaller reflectivity, thus, an increased absorption of the pump beam. Other experimental uncertainties are likely to cause additional variations in the signal level, such as laser energy fluctuations. To enable a true and fair comparison of the echo strength among samples with different Al_2O_3 thicknesses, the data needs to be normalized by the actual absorbed pump energy. Measurements we performed at various pump powers indicate that the magnitude of the electron peak is proportional to the pump power. Therefore, we normalize the signal measured on each sample by its electron peak. The signals after such normalization are shown in Fig. 6.2(a). It is directly observed that the echo timings shift towards longer time delay as the Al_2O_3 thickness is increased, and that the magnitude of the echoes increases. To quantify these observations, we fit the normalized signal by the combination of an exponential decaying function and multiple Gaussian functions:

$$\begin{aligned} \Delta R &= C_B + A_B e^{(-t/\tau_B)} + A e^{-2((t-t_0)/w_0)^2} \\ &+ A_L e^{-2((t-t_L)/w_L)^2} + A_R e^{-2((t-t_R)/w_R)^2} \\ &+ \ldots \end{aligned} \tag{6.3}$$

In Eq. 6.3, the constant C_B and the exponential function with amplitude A_B describe the background signal. The first Gaussian with an amplitude $A(<0)$ describes the trough part of the echo. The other two Gaussian functions with amplitudes $A_L(>0)$ and $A_R(>0)$ account for the left and right

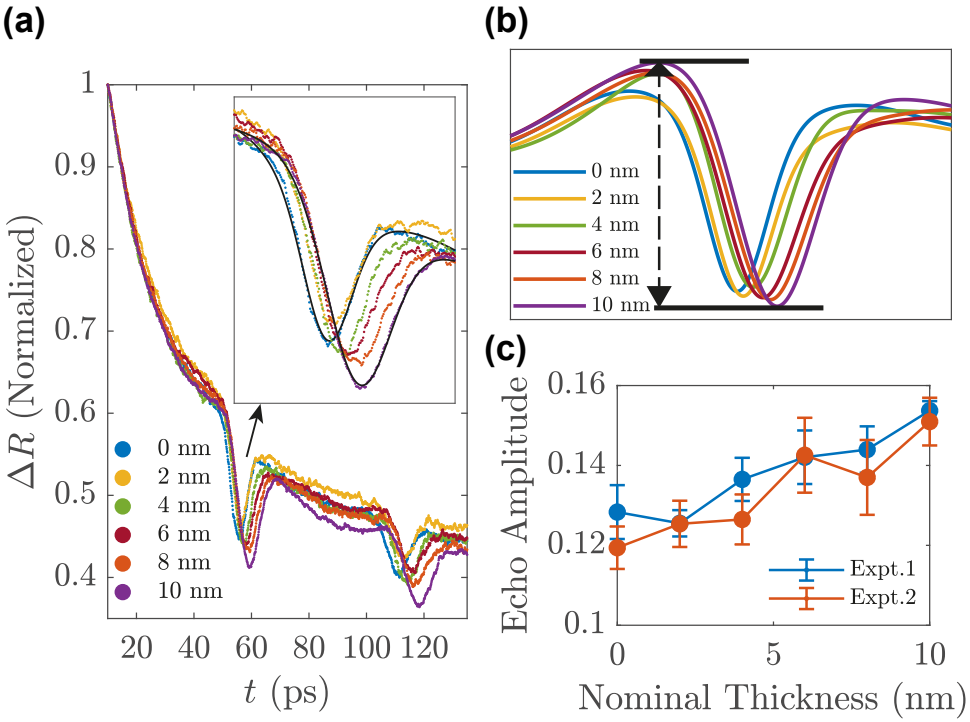

Figure 6.2: (a) The measured reflectivity changes after normalization. The data are shown for samples of different Al_2O_3 thicknesses, in which their nominal values are labeled. The inset of (a) shows a magnified view around the first echo. The black solid lines in the inset are fits to the measured signal by using Eq. 6.3. From the fits, the background signals are subtracted, leaving the echoes to be separated and shown in (b). In (b), the echo amplitude is defined, as the signal difference between the trough and the first crest in the fit. The extracted amplitudes of the first echo are shown in (c), as a function of nominal thickness of the Al_2O_3 layer. The resulting echo amplitudes of two independent experimental runs are shown in (c).

crests of the echo. Two examples of function fits to the measured signals by using Eq. 6.3 are shown as black solid lines in the inset of Fig. 6.2(a). From the fit we subtract the background signal, leaving only the contribution from the echo, as shown in Fig. 6.2(b). The echo amplitude is readily defined as the signal difference between the trough and the first crest in the function fit, as illustrated in Fig. 6.2(b). The resulting amplitudes of the first echo are plotted in Fig. 6.2(c), in which the total length of the errorbar is equal to two times the standard deviation of 5 experimental scans performed on the same sample spot. The results of another 5 experimental scans performed on a different sample spot are also shown (labeled as Expt.2). From this analysis, it is evident that the echo amplitude correlates with the Al_2O_3 thickness.

6.5. Signal interpretation

It is well known that aluminum easily oxidizes when exposed to air [133]. A thicker deposited Al_2O_3 layer acts as a protective layer, preventing further natural oxidation. However, for samples with very thin or absent deposited Al_2O_3 layers, we expect different degrees of natural oxidation to still occur, which will further increase the Al_2O_3 layer thickness and decrease the metal layer thickness. Therefore, the actual Al_2O_3 and metal layer thicknesses are expected to deviate from their nominal values in the actual experiments. To take those effects into account, individual Al_2O_3 layer thicknesses and metal layer thicknesses are also treated as fitting parameters. We expect that our model is able to independently extract both the aluminum and the Al_2O_3 layer thicknesses, as they contribute to the signal in different ways: the echo amplitude is primarily determined by the Al_2O_3 layer thickness, while both the Al_2O_3 and the aluminum layer thicknesses determine the echo timing.

Figs. 6.3(a) shows the measured data and corresponding model fits. The calculated reflectivity, shown as solid lines, reproduce well the measurements for all samples. The best-fit Al_2O_3 layer thicknesses are shown as legends in Figs. 6.3(a). To confirm the accuracy of the best-fit Al_2O_3 thicknesses, we performed independent measurements of the Al_2O_3 layer thicknesses by spectroscopic ellipsometry. The model-extracted values and the ellipsometry results are plotted in Figs. 6.3(c), in which the best-fit values obtained by fitting to the data of an additional experimental run is also shown (labeled by Expt.2). The model-extracted Al_2O_3 layer thicknesses are slightly different than the ellipsometry results. Their difference is about 1.2 nm on average, which demonstrates the accuracy in the determination of the Al_2O_3 layer

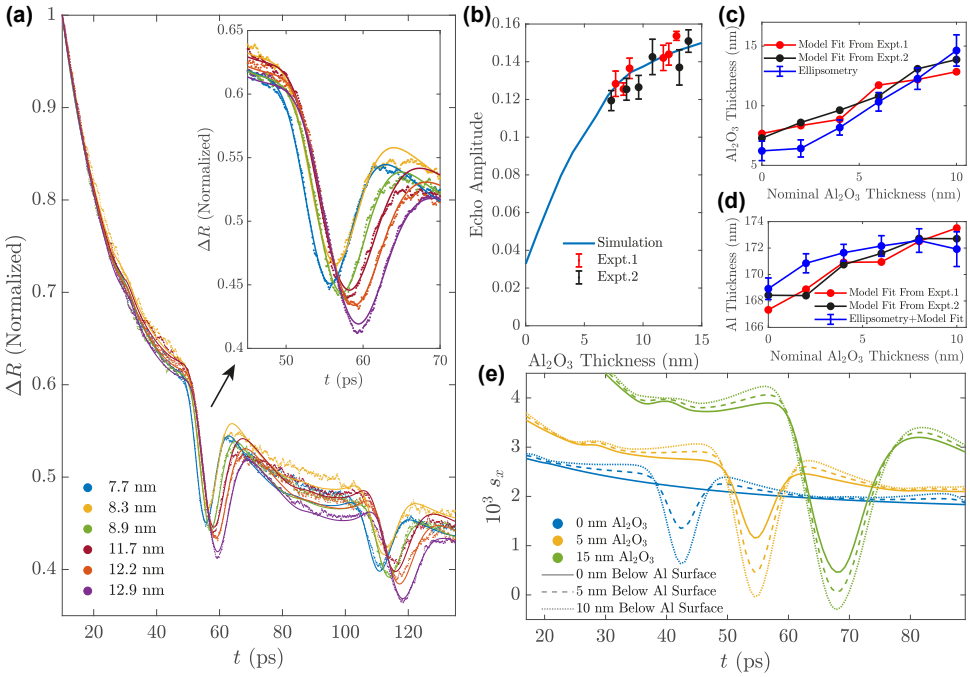

Figure 6.3: (a) Model fit to the measurements. The color represents results on samples with different Al_2O_3 layer thickness. The dots are the measured data, the solid lines with the same color are the data of the corresponding model fit. The legends in (a) are the best-fit Al_2O_3 layer thicknesses. The insets show magnified views around the first echoes. (b) Comparison of the (first) echo amplitude between simulations (solid line) and measurements (dots), versus Al_2O_3 layer thickness, in which the results of two independent experiments are shown. The best-fit Al_2O_3 layer thicknesses and Al layer thicknesses are plotted in (c) and (d), respectively, along with the thicknesses measured by ellipsometry. The dynamics of longitudinal strain (s_x) at and below the aluminum surface are shown in (e). The color represents the Al_2O_3 layer thickness, while the line style represents the depth where the strain data is shown. Note that the blue and green lines are horizontally shifted by $\mp$10 ps for clarity.

thickness by our model fit. In addition, the best-fit thicknesses to the two independent experimental runs are consistent within 1 nm.

Ellipsometry does not allow access to the aluminum layer thickness as aluminum is optically opaque. To have an independent measurement of the aluminum layer thickness, we take the ellipsometry results of the Al_2O_3 layer thickness to be used as model inputs and only fit the aluminum layer thickness to our measured data. In this way, the aluminum layer thickness is solely determined by the echo timing, which is expected to yield aluminum layer thickness in a comparable accuracy as the ellipsometry measurement. The thicknesses obtained in this way are labeled as 'Ellipsometry+Model Fit' in Figs. 6.3(d) and they are plotted along with the purely model-extracted values. The extracted thicknesses are consistent within 2 nm. This demonstrates that our acoustic approach can yield the thickness of both transparent and opaque layers, with close-to-ellipsometry accuracy. In addition, the determined aluminum layer thicknesses are consistent with our expectations from natural oxidation: For the samples with thinner pre-deposited Al_2O_3 layers, the aluminum layer thickness is smaller, indicating a larger degree of natural oxidation. While for the samples with thicker pre-deposited Al_2O_3 layers, the aluminum layer thicknesses saturate at the original value due to the protective effects of a thicker pre-deposited Al_2O_3 layer.

Figs. 6.3(b) shows a comparison between the echo amplitudes from the measured and simulated signals in those samples, which shows excellent agreement. Both of them indicate an amplification of echo amplitude for samples with a thicker Al_2O_3 layer. We note that due to natural oxidation, aluminum samples with very thin or no oxide layers are not accessible in our conditions. Yet, for other metals that are hard to be naturally oxidized, the echo amplification effect by depositing transparent layer on top is expected to be larger.

6.6. Discussion

The increase in the echo strength is an inevitable consequence of the boundary condition at free surfaces. The free boundary condition requires the total stress to vanish at free surfaces [75]: $\sigma_{total} = 0$. The total stress can be decomposed into two contributions: $\sigma_{total} = \sigma_{th} + \sigma_{str}$, where σ_{th} is the thermal stress due to lattice temperature increase, and σ_{str} is the stress associated with lattice deformation (i.e., strain). The latter can be decomposed further into two contributions: $\sigma_{str} = \sigma_{surf} + \sigma_{prop}$, where the σ_{surf} is a

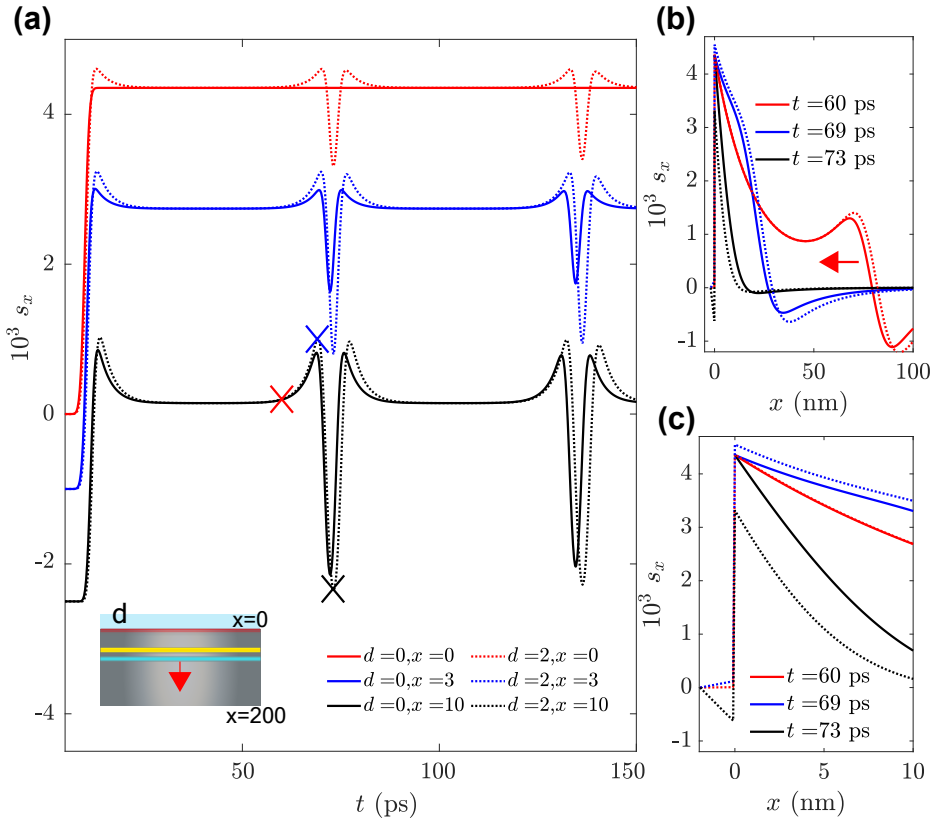

Figure 6.4: Propagation of a hypothetical 1D strain pulse subjected to the free boundary condition, in a 200 nm aluminum free-standing membrane with a Al_2O_3 layer of thickness d on top. (a) The strain dynamics at three specific positions ($x = 0$ nm, $x = 3$ nm and $x = 10$ nm) beneath the aluminum surface. The legends are all in the unit of nm. Note that the blue and black curves have vertical offsets for clarity. (b) The strain spatial profiles at different time instants. The time instants are marked by the three crosses in (a). (c) A zoom in of (b) in the surface region. A schematic of the sample used in calculations is plotted as an inset of (a), in which the topmost region of the aluminum is heated and a strain pulse is launched into the interior. The red region at the aluminum surface illustrates the heat source. The yellow and blue-green area illustrate the positive and negative parts of the generated strain. The red arrows indicate the propagation direction of the strain. In all figures, the solid lines represent calculations without the Al_2O_3 layer, the dotted lines represent calculations with a 2 nm Al_2O_3 layer on top.

non-propagating part that is stationary at the irradiated surface, the propagating part σ_{prop} is associated with the lattice deformation by propagating strain which composes the acoustic wave itself. Thus, the total stress is the sum of three contributions: $\sigma_{total} = \sigma_{th} + \sigma_{surf} + \sigma_{prop}$. The free boundary condition then requires that

$$\sigma_{th} + \sigma_{surf} + \sigma_{prop} = 0. \tag{6.4}$$

Eq. 6.4 describes the situation when the propagating strain has reached the free surface. When the propagating strain leaves the free surface, only the first two contributions remain, i.e.,

$$\sigma_{th} + \sigma_{surf} = 0. \tag{6.5}$$

Since Eq. 6.4 and Eq. 6.5 have to be both satisfied, at free surfaces, we must have $\sigma_{prop} = 0$. This means, the echo, manifested as the returned propagating strain, is zero at the free surface.

To better elaborate the effect of a free surface on strain dynamics, we show the propagation of a hypothetical 1D strain, subjected to the free boundary condition. The strain pulse is launched in the simulation by a hypothetical heat source localized at the surface region of a 200 nm aluminum free-standing membrane. The heat source is described by a swift temperature increase with a rise time of 5 ps, with a spatial profile following an exponential decay with a characteristic length of 20 nm, and a maximum temperature increase of 30 K. The heat source is more localized to the surface than that in the experiment, which ensures a narrow spatial extent of the resulting strain pulse. This results in well-separated echoes, and facilitates the observation of free surface effects on strain propagation. In Fig. 6.4(a), we plot the strain dynamics at three specific locations beneath the aluminum surface, for samples with a Al_2O_3 layer of two different thicknesses on top. For the sample without the Al_2O_3 layer ($d = 0$ nm), at the aluminum surface ($x = 0$ nm), as shown by the solid red trace, only the nonpropagating strain is nonzero. The acoustic echo, caused by the return of the propagating strain, is always zero at the surface. The amplitude of the propagating strain increases as it propagates away from the surface, as shown by the blue and black traces. In contrast, for the sample with a nonzero Al_2O_3 layer ($d = 2$ nm) on top, the propagating strain is nonzero even at the aluminum surface. In addition, the echoes beneath the aluminum surface are all amplified.

The effect of free surface on the spatial profile of the strain can be seen in Fig. 6.4(b) and 6.4(c), where we plot the strain profiles at three time in-

stants. In the solid red trace in the $d = 0$ nm sample, we see the separation of the propagating strain from the surface (nonpropagating) strain, the total surface stress at this time instant satisfies Eq. 6.5. In the solid blue and black traces, the propagating strain arrives at the free surface and overlaps with the surface strain, the total stress satisfies Eq. 6.4. Because of those boundary conditions, the strain at the aluminum surface remains the same and is not affected by the return of the propagating strain. This can be clearly seen in Fig. 6.4(c), where the strain at the aluminum surface ($x = 0$) remains the same at all time for the sample without the Al_2O_3 layer (solid lines). In contrast, the returning of the strain in the sample with a nonzero Al_2O_3 layer does alter the strain at the aluminum surface, and amplifies the echoes at all depths (dotted lines). In addition to our rigorous simulation of the experimental signals discussed earlier, these simulations of an idealized situation provide an intuitive picture and explains the increase of echo amplitude observed in our experiments.

The above conclusion has an important implication on the optical detection of strain waves by photoelastic effects. Since the optical penetration depth of metals is usually only a few nanometers, at the very surface of the metal where the optical intensity of the probe pulse is the highest, its contribution to the reflectivity change of the acoustic echo is zero. The reflectivity change measured in this case only results from the strain waves below the free surface (and within the optical penetration depth) where the probe pulse is attenuated. This prevents the probe pulse from detecting the full strength of the propagating strain, and thus lowers the detection efficiency. When a transparent layer is added on top of the free surface, it repositions the free boundary away from the detection surface. This enables the probe pulse to also sample the strain wave at the metal surface and it amplifies the echoes below the metal surface, which results in an enhanced detection of the strain waves.

7

High-resolution microscopy through optically opaque media using ultrafast photoacoustics

We present a high-resolution microscopy capable of imaging buried structures through optically opaque materials with micrometer transverse resolution and a nanometer-scale depth sensitivity. The ability to image through such materials is made possible by the use of laser ultrasonics techniques, where an ultrafast laser pulse launches acoustic waves inside an opaque layer, and subsequent acoustic echoes from buried interfaces are detected optically by a time-delayed probe pulse. We show that the high frequency of the generated ultrasound waves enables imaging with a transverse resolution only limited by the optical detection system. We present the imaging system and signal analysis, and demonstrate its imaging capability on complex microstructured objects through 200 nm thick metal layers, and gratings through 500 nm thickness. Furthermore, we characterize the obtained imaging performance, achieving a diffraction-limited transverse resolution of 1.2 μm, and a depth sensitivity better than 10 nm.

This chapter has been published as part of Opt. Express **28**, 33937-33947 (2020) [130].

7.1. Introduction

Optical imaging methods are essential in many areas of science and technology. In the semiconductor industry, optical metrology tools are employed for rapid positioning and accurate quantitative inspection of layer-to-layer placement in lithographic devices [3, 134]. This type of metrology requires high-numerical-aperture imaging systems to be sensitive to sub-micrometer-sized metrology markers. Semiconductor device architectures are becoming increasingly complex, leading to the use of sophisticated three-dimensional nanostructures for e.g. memory devices [96, 135, 136]. As such structures often contain materials that are optically opaque, imaging and metrology tools are needed that can detect metrology markers through layers of such opaque materials, while maintaining sufficient spatial resolution.

Acoustic waves have the capability to propagate through almost any material. While acoustic metrology is often associated with larger scales, ultrafast-laser-induced acoustic waves [5, 19, 25, 75, 76, 137, 138] can actually reach frequencies up to the THz range [6, 12, 20, 139], and therefore have remarkably short wavelengths. Photoacoustic methods can therefore provide contrast on micron-sized features commonly used in optical metrology, combined with the ability to detect such features through materials that are fully opaque to light. This combination of properties has already motivated the development of high-resolution photoacoustic imaging systems [24, 140, 141] using ultrafast-laser-induced ultrasound pulses. Daly et al. [140] demonstrated the possibility to detect and image sub-optical-wavelength features through acoustic diffraction.

In this paper, we present an optical microscope system that uses ultrafast laser driven ultrasound pulses for high-resolution imaging of complex microstructures through layers of opaque media. Both generation and probing of the ultrasound waves are performed from the same side, which is a fundamental requirement for substrate-based objects, enabling imaging of buried microscopic features to which no optical access is possible, in a non-invasive way. Both temporal and spatial scans are performed to obtain a spatially resolved map of the local layer thickness, from which a 3D map of the buried structures is obtained. We performed such experiments on both periodic and non-periodic objects with feature sizes down to 500 nm. We also describe the analysis procedure and how that provides quantitative information, to determine the spatial resolution in transverse and axial dimensions (thickness). In addition, we demonstrate a faster imaging approach, in which a

spatial scan is performed at fixed pump-probe time delay [141] to provide contrast in imaging buried objects.

7.2. Experimental methods

7.2.1. Pump-probe setup for time-dependent reflectivity measurements

Femtosecond lasers can generate high-frequency sound waves in metals through ultrafast and strongly localized absorption of radiation by the electron gas [25, 75, 76]. When a femtosecond pulse strikes a metal, the energy is initially mainly absorbed by the electrons, which subsequently equilibrate with the lattice on a timescale of picoseconds. This energy exchange leads to a rapid increase of the lattice temperature, generating a thermal stress that is the source for the acoustic waves. The resulting acoustic waves travel inside the metal and partially reflect off buried material interfaces. The returning reflected 'echo' is optically detectable at the surface, as the local lattice strain leads to changes in the complex refractive index. A measurement of the time-dependent metal reflectivity therefore reveals the presence of ultrasound-induced strain at the sample surface. To generate and detect laser-produced ultrasound pulses, a pump-probe scheme is implemented [6, 12]. A schematic of the experimental setup is shown in Fig. 7.1. The output of a long-cavity

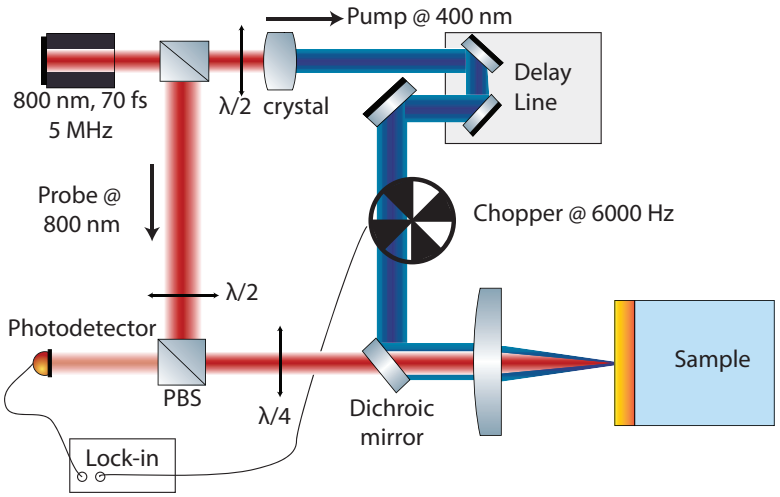

Figure 7.1: Schematic of the pump-probe setup used to measure time-dependent reflectivity changes. A 90-10 beam splitter at the output of the laser divides the beam in pump and probe. BBO: Beta-barium borate crystal for frequency doubling. $\lambda/2$: half-wave plate. $\lambda/4$: quarter-wave plate. PBS: polarising beamsplitter. See text for details.

Ti-sapphire oscillator (Femtolasers XL500: wavelength centered at 800 nm, pulse duration 70 fs, repetition rate 5.1 MHz) is split into separate pump and probe paths by a beamsplitter ($R = 10\%$). In the more powerful arm the beam is frequency-doubled to 400 nm using a β-barium borate (BBO) crystal. The energy of the 400 nm pulses is controlled through polarisation rotation with a half-wave plate ($\lambda/2$) before the BBO crystal, as the up-conversion efficiency is polarisation-dependent. The 400 nm beam is used as pump beam in the experiment, while the remaining infrared light in this path is blocked using colour filter. The arrival time of the pump pulses at the sample is controlled using a mechanical delay line (Physik Instrumente). We used the less powerful output of the first beamsplitter as the probe beam. The wavelength of this arm is kept at 800 nm. The pump and probe beams are recombined using a dichroic mirror and sent into the focusing objective (Olympus LCPLN20XIR, x20, numerical aperture (NA) 0.45). The beam diameter in the sample plane is approximately 1 µm for both pump and probe. The pump and probe beams are collinear and illuminate the sample at normal incidence. The pump power incident on the sample is 1.2 mW, which corresponds to a fluence of 0.06 J/cm^2. We detect the reflectivity changes as function of time delay by directing the reflected probe beam onto a silicon photodiode. The photodiode signal is sent to a lock-in amplifier (LIA) after being low-pass filtered ($f_{cut-off} = 12.5$ kHz). The LIA is referenced by the driving signal of the chopper wheel used to modulate the pump excitation. The LIA then acts as a band-pass filter, selectively amplifying the modulated pump-induced signal above the broadband white noise background.

7.2.2. Spatially resolved layer thickness determination

Figure 7.2(a) shows the relative reflectivity change $\Delta R/R$ as function of time delay between pump and probe, for gold layers with two different thicknesses. The sharp feature near zero time delay reveals the excitation of the free electrons [7, 36, 142]. At longer delay the signal becomes oscillatory, which is a sign of the propagation of the acoustic wave packets inside the metal layer. These signals are a complex superposition of multiple contributions to the local strain, also including effects of local surface heating and surface waves. From a detailed analysis [5], we find that for gold surfaces the dips in the reflectivity correspond to the returning acoustic echo. The period that characterizes these oscillations depends on the speed of sound in the material and the layer thickness. Therefore, a Fourier transform of the measured reflectivity curve (Fig. 7.2(b)) provides a measurement of the local layer thickness.

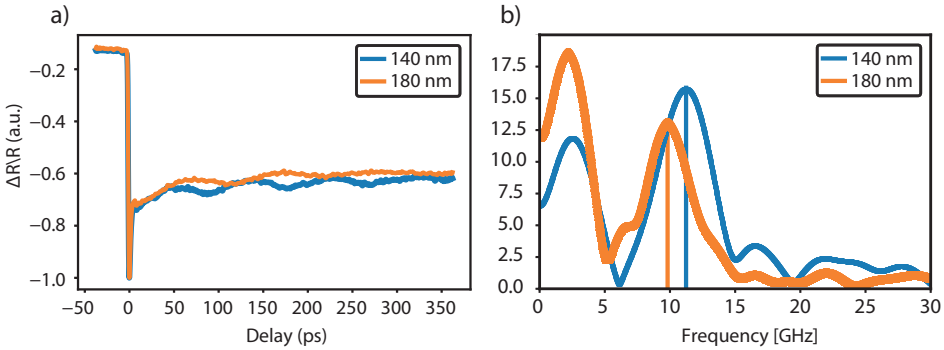

Figure 7.2: a) Typical pump-probe delay scan for a single gold layer with two different thicknesses, 140 nm (blue line) and 180 nm (orange). After the sharp response at zero delay, the signals oscillate with a period that depends on the thickness and speed of sound. b) The Fourier transform of the delay scans after removing the contribution of the strong zero-time-delay spike. The vertical lines intersect the x-axis at the frequency that corresponds to a round trip of an echo through the thickness of the layer. The frequency value is used to calculate the period of the oscillation and subsequently the thickness of the layer.

With acoustic frequencies in the range of 10 GHz as shown in this example, the corresponding acoustic wavelength is actually only around 320 nm, which is below the optical diffraction limit. Therefore, even with tightly focused beams, a thickness determination can be performed at a transverse spatial resolution limited by the optical spot size rather than the acoustic wavelength. This feature enables high-resolution microscopic imaging through metal layers, using the laser-induced acoustic waves as an intermediary, without loss of spatial resolution compared to conventional light-based microscopy. To record a spatial map of layer thickness, we mount the sample on a 3D piezo-driven translation stage (Smaract GmbH). We define the optical axis as 'z', with the transverse plane containing the 'x'- and 'y'-axis. We raster-scan the surface of the sample and perform a pump-probe delay scan at each point.

In the measured signal in Fig. 7.2(a), an offset at negative time delays is visible (as $\Delta R/R = 0$ is the calibrated reflectivity without pump light). We find that this background level depends on layer thickness and pump power, suggesting that it is due to a cumulative heating effect caused by the relatively high repetition rate of the laser. In particular for thinner layers, the energy deposited by consecutive pulses cannot diffuse out of the excitation region completely, increasing the temperature of the sample and resulting in

a refractive index change. This effect does not affect the thickness determination as it does not change the measured oscillation frequency.

7.2.3. Sample fabrication

To characterize our imaging system and test its capabilities, we fabricated several samples. The sample fabrication consisted of depositing metal layers of controllable thickness onto a glass substrate (SiO_2, 170 µm thick), and subsequently printing patterns on the metal-air interface using two different nano-lithographic procedures: UV lithography and focused ion beam (FIB) milling. The UV lithography has been used for gratings with a pitch of 6 µm and 50% duty cycle on a thick metal layer. Finally, the FIB has been used to fabricate samples with non-periodic patterns.

In order to make the patterns appear as buried structures, we performed the measurements illuminating the samples from the glass side, generating acoustic waves at the glass-metal interface. This approach was chosen as it ensures a flat interface without any residual topography that might resemble the underlying object structure.

7.3. Results

7.3.1. Imaging buried periodic structures

We first performed pump-probe experiments on the grating sample to determine the accuracy with which the thickness is measured as function of position in the transverse direction.
Figure 7.3(a) shows a schematic of the sample fabricated using the UV lithography. The gold (Au) gratings with an amplitude of 10 nm and a pitch of 6 µm are fabricated on top of a 500 nm thick uniform Au layer. On this sample we perform spatially resolved pump-probe measurements as explained in the previous section. The change in reflectivity as function of delay time is shown in Fig.7.3(b). The two measurements have been taken from the glass side at two different points in correspondence of the top and the valley of the grating. Similar curves are recorded for a larger area. We move the sample stage with steps of 1 µm in the x direction and 1 µm in y, covering a 4 x 31 µm ^{2} area.

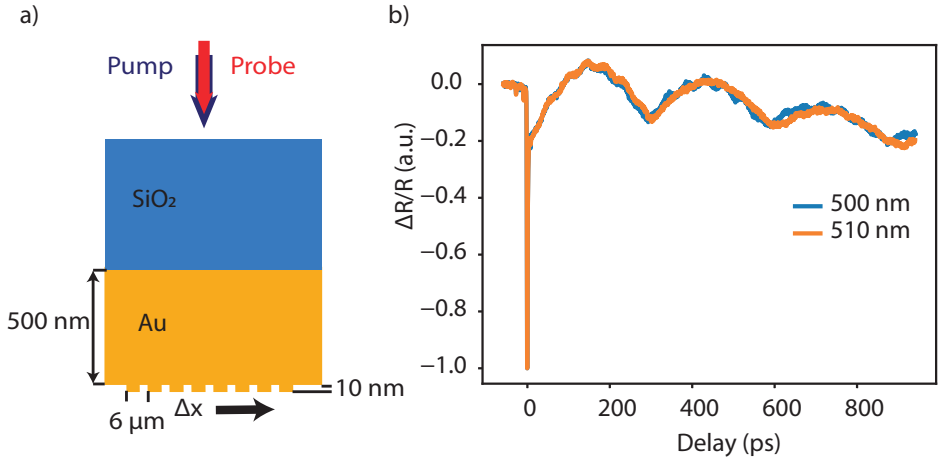

Figure 7.3: a) Schematic of the buried grating samples. The pump-probe experiments are done from the glass side of the sample, which consists of a uniform gold layer with a patterned grating on the metal-air interface. b) Photoacoustic measurements at two different positions on the sample corresponding to the top and bottom of the grating. The thickness at these two positions is 500 nm (blue line) and 510 nm (orange), respectively.

The time traces recorded at each spatial position have an oscillatory part caused by the acoustic waves travelling along the longitudinal direction. The accuracy with which this temporal periodicity is estimated determines the measurement accuracy of the layer thickness. In time domain, the maximum achievable accuracy is limited by the probe pulse duration of 70 fs, but the sampling of the temporal scan and the accuracy of the frequency determination also need to be considered.

The temporal sampling time is linked to the integration time of the LIA, which was set to 3 ms. The delay line scans the pump-probe delay at 40 ps per second, leading to a temporal averaging over 120 fs for every data acquisition. The digital acquisition card (DAQ) records data at 1 kHz. For a speed of sound in Au of 3240 m/s, a time resolution 120 fs corresponds to a height sensitivity of 0.39 nm.

A standard approach to obtain the periodicity of an oscillatory signal is to look at its Fourier transform and localize the frequency component that has the highest contribution to the signal. In practice, the achievable accuracy in thickness is therefore mainly limited by the accuracy of the acoustic frequency determination. For the grating in Fig. 7.3(a) the expected difference in time delay for one round-trip of the acoustic wave at the peaks and valleys of the gratings is 6 ps, on a total delay time of 310 ps, which is round trip period of

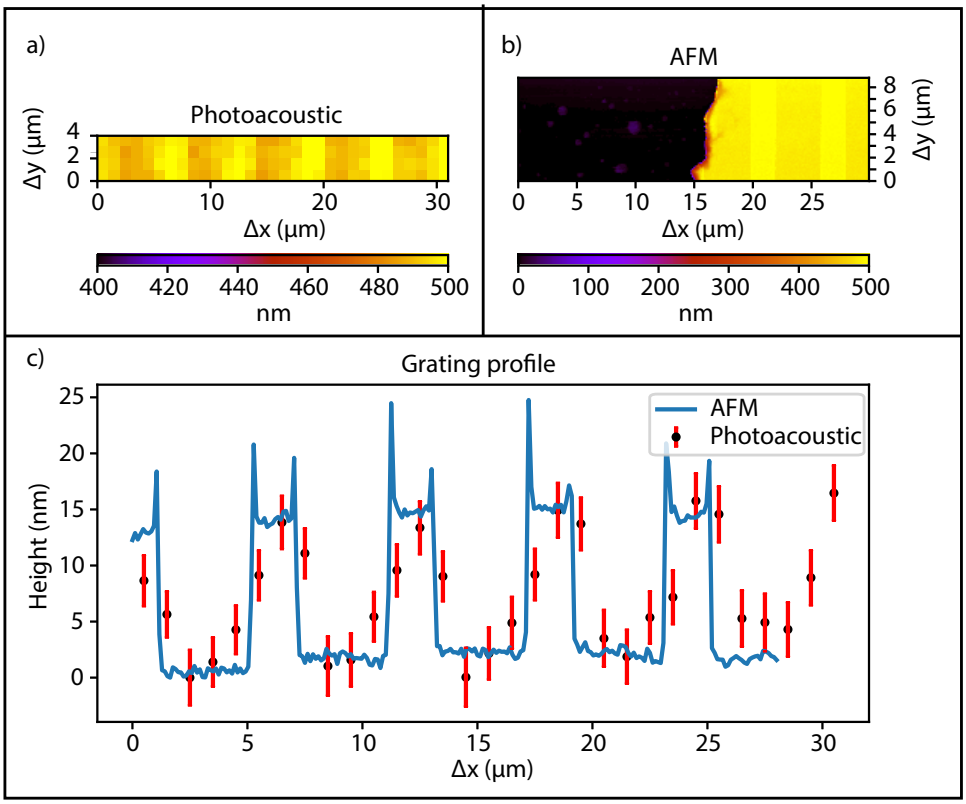

Figure 7.4: Photoacoustic imaging of a 10 nm amplitude grating underneath a 500 nm thick layer of gold. a) The measured height map obtained by making a delay scan per pixel. Thickness reconstruction using time-domain fitting. See text for details on the model used for the fit. b) AFM measurement near an edge of the coated layer, showing the total grating thickness. c) Comparison of AFM and photoacoustic measurements, averaged along the y-direction for a range as shown in Fig. 7.4(a). The photoacoustic measurement points are offset by the absolute measured height of 487 nm.

an echo in a 500 nm gold layer. While this time delay difference is larger than the temporal resolution of the measurement, the small relative difference in signal strength combined with the relative wide width of the acoustic frequency profiles (Fig. 7.2(b)) requires an accurate determination of the exact echo timing from the measured data, which can be challenging especially in the case of limited signal-to-noise ratio (SNR). An alternative approach better suited for echo timing determination on our thick Au samples is to fit the time-domain signals directly [5]. To this end, we apply a numerical low pass filter (f_{cut}=30 GHz) and perform a least-squares fit of the filtered data to a damped oscillator model $y_s = A \cdot e^{\alpha_{osc} t} \sin(2\pi f t + \phi)$. However, since the

oscillatory signal is on top of a slowly decaying background, we introduce two extra terms in the model: $y_b = A_e \cdot e^{\alpha_e t} + A_b \cdot e^{\alpha_{osc} t} \sin(2\pi f_b t + \pi/2)$. The complete model is the sum of y_s and y_b. The fit is done for all traces measured at different points on the rastered area. The background is determined only for one spatial location and kept constant for all others. In this way we retrieve the oscillation period, from which the local layer thickness can be calculated with a well-defined fit uncertainty. The fit procedure returns the variance that is used to calculate the interval of confidence ($\pm 3\sigma$). The result is shown in panel a of Fig. 7.4, and shows good agreement with the nominal values. The Au layer thickness was found to be 487 ± 2 nm. To obtain an independent validation of the measured thickness, we perform atomic force microscopy (AFM) measurements on the grating side of the sample, near the edge of a cleared area in the gold layer (Fig. 7.4(b)). The measured Au layer thickness was 486 ± 2 nm. A direct comparison between the photoacoustic measurement and the AFM measurement is given in Fig. 7.4(c), showing a line-out in the direction perpendicular to the grating lines for both measurement methods. The photoacoustic data are an average of the 4 data points along the vertical direction of Fig. 7.4(a). The error bar mainly results from the fit uncertainty of the thickness measurements for the individual scan points. There is a good agreement in terms of the determination of the height of the grating lines: some deviations in the transverse shape can be seen, although these are mostly within the photoacoustic measurement uncertainty.

7.3.2. Non-periodic structures and image resolution

To prove the versatility of our imaging system, we have extended the measurements to imaging of non-periodic structures. Reference images of the studied samples are displayed in Fig. 7.5(a),(b). These samples contain the logo of our institute (ARCNL) and a map of Amsterdam, which have been patterned into a 270 nm and 200 nm Au layer respectively using a Focused Ion Beam (FIB). Two separate versions of the institute logo were produced, differing only in the step height between the logo and its surroundings (being 60 and 120 nm). An AFM image of the 60-nm-depth sample is shown in Fig. 7.5(c).

Spatially resolved photoacoustic measurements are performed on both logo samples, and the results are shown in Fig. 7.6(a,b). The image size is 60 µm by 30 µm, obtained with a step size of 2 µm in both directions. The thickness determination is performed using the time-domain fitting procedure discussed in the previous section, and shows quantitative agreement with

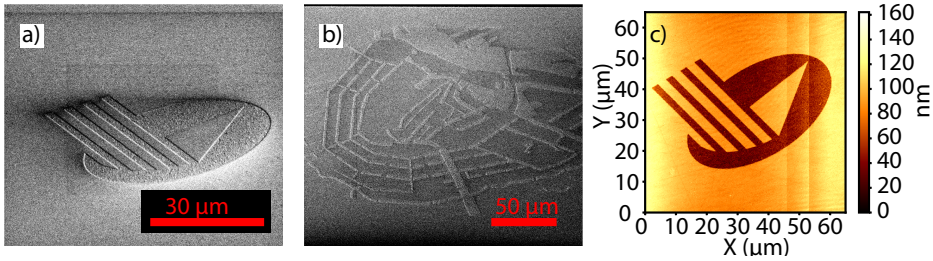

Figure 7.5: a) Scanning electron microscope (SEM) image of the ARCNL logo, fabricated using Focused Ion Beam (FIB) milling. The patterns were milled 60 nm deep into a 270 nm thick Au layer. b) SEM image of a map of Amsterdam also produced by FIB, milled 50 nm deep into a 200 nm thick Au layer. c) AFM image of the ARCNL logo, showing the 60 nm thickness difference.

the nominal values. Each spatial pixel required a time-domain scan of ≈20 seconds, resulting in a measurement time of 3 hours for the full image. To improve the image acquisition speed, the pump-probe delay can be set to a fixed value determined from a single time-delay scan at a reference position. A spatial raster scan at such a constant time delay can then still provide image contrast for buried layers, although at the cost of losing the absolute layer thickness information [141].

Examples of such measurements on the 60-nm-deep logo sample are shown in Fig. 7.6(c)-(e), where we set the pump-probe time delay to different values around the arrival time of the first acoustic echo from the flat Au layer, and measure the sample reflectivity as a function of position by spatially scanning the sample along the focused beams. Each horizontal scan is performed by continuous motion at constant velocity, after which a discrete vertical step of 1 µm is taken. With this approach, recording each image in Fig. 7.6(c)-(e) takes 2 minutes. We emphasize that this measurement method only provides reflection-based image contrast rather than quantitative layer thickness information: by setting the time delay to different values, the contrast changes strongly and can even be inverted. The change in contrast between the logo and the surrounding are visible in Fig 7.6(c)-(e) for different delay time. In Fig 7.6(f), the time traces for a scan position at the logo and at the surrounding area are shown. A large difference in $\Delta R/R$ results in higher image contrast. In Fig. 7.6(c), 120 ps time delay corresponds to the expected peak of the first echo from the logo. At a 180 ps time delay (Fig. 7.6(d)), which is close to the expected arrival time of the echo from the structure surround-

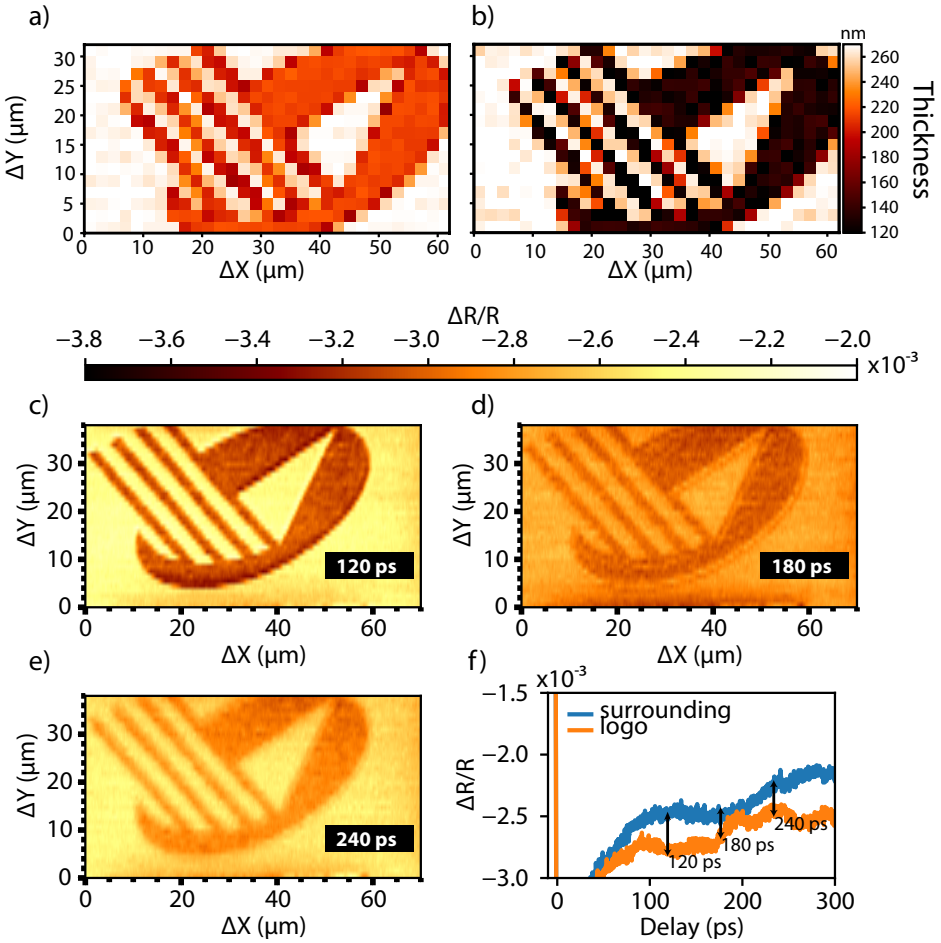

Figure 7.6: Photoacoustic measurements on the ARCNL logo below a 270 nm thick gold layer. (a),(b) Spatially resolved thickness measurements on samples with depths of 60 nm (a) and 120 nm (b). (c-e) Photoacoustic measurements on the 60-nm-depth structure with a fixed delay between pump and probe. The three images are taken at different time delay settings. These measurements are significantly faster, but do not provide quantitative thickness information. (f) Part of the time-delay scan for the spatial positions at and next to the logo sample, for the range including the time delays of images (c-e).

ing the logo, the contrast between logo and surroundings diminishes. The contrast increases again towards the second echo from the logo at 240 ps (Fig. 7.6(e)).

In a scanning-probe imaging method as employed here, the achievable transverse resolution is ultimately limited by the focal spot size. In addition, the step size of the spatial scan needs to be chosen smaller than the laser spot

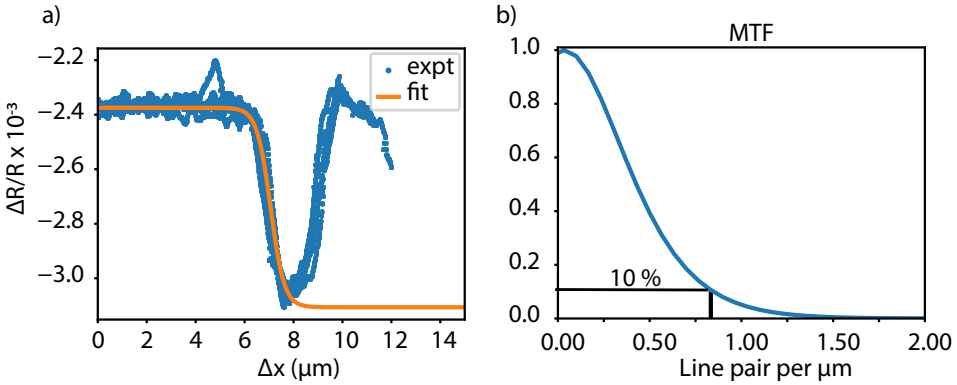

Figure 7.7: a) Reflectivity change as a function of scan position for a 1D scan across a diagonal line on the left side of the ARCNL logo (Fig. 7.6(c)), at various ΔY positions (scans corrected for horizontal displacement as function of ΔY). Least-squares fitting yields the edge response function. b) The modulation transfer function (MTF), which is the Fourier transform of the derivative of the edge response function. The 10% value corresponds to the maximum number of line pairs per μm that can be resolved.

size to avoid undersampling issues. Using a continuous scan of the stage this requirement is satisfied at an acquisition rate of 1 kHz and a stage speed of 20 μm /s. To characterize the transverse resolution of our imaging system we use an edge response method [143]. The reflectivity changes near the edge of the tilted lines in the logo shown in Fig. 7.6(c) are used to reconstruct an oversampled edge function. Multiple horizontal scans of the leftmost line at increasing ΔY positions are recorded, subsequently aligned, and used to least-squares fit an edge response function (Fig. 7.7(a)). The derivative of the determined edge response function gives the line response, and a Fourier transform of this line response function yields the modulation transfer function (MTF) that is typically used to define the resolution of optical systems [144]. The resulting normalized MTF for our system is shown in Fig. 7.7(b): the 10% value is typically taken as the number of line pairs that the imaging system can resolve. We find a value of 0.83 line pairs per μm, meaning a spatial resolution of 1.2 μm. This resolution is close to the Rayleigh diffraction limit at 0.45 NA, given by 0.61 λ/NA = 1.1 μm, and is consistent with the measured spot sizes of pump and probe.

The improved acquisition speed of the fixed-time-delay method allows imaging of millimeter scale structures with no compromise in imaging resolution. To demonstrate this important aspect we fabricated such a sample, shown

in Fig. 7.5(b). The sample is a map of the canals of Amsterdam, with spatial dimensions of 250 × 250 µm ^{2}. We use the FIB to draw the map on a 200 nm gold layer and remove 50 nm from the exposed area. A photoacoustic measurement at a fixed time delay of 110 ps is shown in Fig. 7.8. A good contrast image of the map is obtained scanning a length of 350 µm at 40 µm /s along the x-direction and a length of 400 µm in steps of 2 µm along the y-direction. The map contains various 1-µm-size features, which are well resolved without significant loss of contrast even comparing with the SEM image (Fig.7.5(b)).

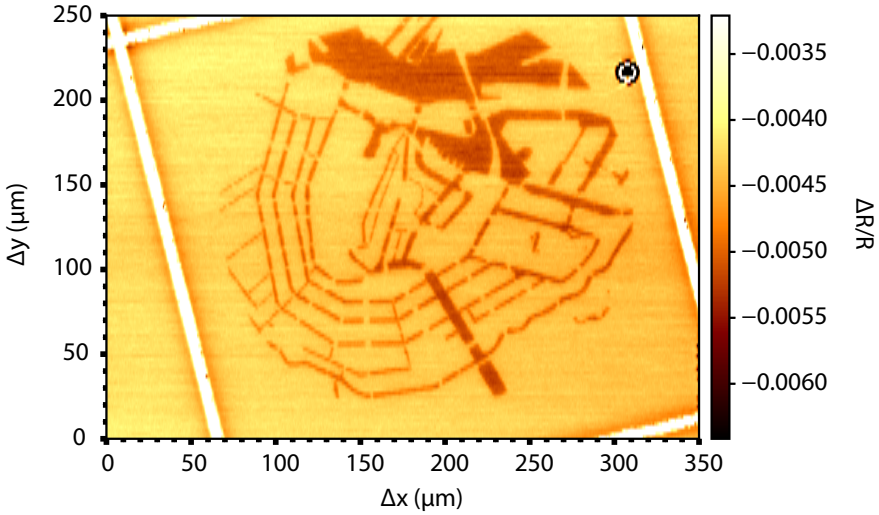

Figure 7.8: Photoacoustic measurement of the Amsterdam canal map sample buried underneath a 150 nm thick gold layer. The pump-probe time delay was fixed at 110 ps.

7.4. Conclusion

We have developed a scanning-probe photoacoustic microscope that enables high-resolution imaging of microscopic structures buried below opaque layers. A fitting procedure has been used to determine the thickness of the layer, reconstructing height maps of buried objects with an accuracy of 2 nm. We note that the achievable depth sensitivity is dependent on material properties, which determine the frequency content of the acoustic wave. As gold supports only limited acoustic frequencies, even higher depth sensitivity may be expected for other metals. We have recorded images of spatially non-

periodic structures with sub-µm feature sizes, using pump-probe scans at discrete spatial positions, as well as continuous scans at fixed pump-probe time delay. From these images we have characterized the spatial resolution of the imaging system by determining its MTF, which resulted in a near-diffraction-limited spatial resolution of 1.2 µm.

We compared the photoacoustic measurement to an AFM measurement, which showed good agreement in the height determination of the grating structure. Furthermore, we emphasize that our measurement method is non-invasive as it operates well below the damage threshold of the opaque layer. Future improvements to the SNR such as higher-frequency LIA methods can be envisaged, further improving sensitivity and imaging speed. We therefore see applications of this imaging approach in materials science and the characterization of semiconductor nanostructures, among others.

References

[1] G. E. Moore, *Cramming more components onto integrated circuits,* Proceedings of the IEEE **86**, 82 (1998).

[2] H. Mujtaba, *Amd 2nd gen epyc rome processors feature a gargantuan 39.54 billion transistors, io die pictured in detail,* https://wccftech.com/amd-2nd-gen-epyc-rome-iod-ccd-chipshots-39-billion-transistors/.

[3] A. J. den Boef, *Optical wafer metrology sensors for process-robust CD and overlay control in semiconductor device manufacturing,* Surface Topography: Metrology and Properties **4**, 023001 (2016).

[4] S. W. G. Bouwhuis, *Automatic alignment system for optical projection printing,* IEEE Transactions on Electron Devices **26**, 723 (1979).

[5] H. Zhang, A. Antoncecchi, S. Edward, I. Setija, P. Planken, and S. Witte, *Unraveling phononic, optoacoustic, and mechanical properties of metals with light-driven hypersound,* Phys. Rev. Applied **13**, 014010 (2020).

[6] P. Ruello and V. E. Gusev, *Physical mechanisms of coherent acoustic phonons generation by ultrafast laser action,* Ultrasonics **56**, 21 (2015).

[7] J. Hohlfeld, S.-S. Wellershoff, J. Güdde, U. Conrad, V. Jähnke, and E. Matthias, *Electron and lattice dynamics following optical excitation of metals,* Chemical Physics **251**, 237 (2000).

[8] M. Bonn, D. N. Denzler, S. Funk, M. Wolf, S.-S. Wellershoff, and J. Hohlfeld, *Ultrafast electron dynamics at metal surfaces: Competition between electron-phonon coupling and hot-electron transport,* Phys. Rev. B **61**, 1101 (2000).

[9] T. Q. Qiu and C. L. Tien, *Heat Transfer Mechanisms During Short-Pulse Laser Heating of Metals,* Journal of Heat Transfer **115**, 835 (1993), https://asmedigitalcollection.asme.org/heattransfer/article-pdf/115/4/835/5698866/835_1.pdf .

[10] J. E. B. J. K. Chen, *Numerical study of ultrashort laser pulse interactions with metal films,* Numerical Heat Transfer, Part A: Applications **40**, 1 (2001), https://doi.org/10.1080/104077801300348842 .

[11] Z. Lin, L. V. Zhigilei, and V. Celli, *Electron-phonon coupling and electron heat capacity of metals under conditions of strong electron-phonon nonequilibrium,* Phys. Rev. B **77**, 075133 (2008).

[12] O. Matsuda, M. C. Larciprete, R. L. Voti, and O. B. Wright, *Fundamentals of picosecond laser ultrasonics,* Ultrasonics **56**, 3 (2015).

[13] H. Irschik, A. Bedford, and D. S. Drumheller, *Introduction to Elastic Wave Propagation. Chichester etc., John Wiley & Sons 1994. XIII, 297 pp., £ 39.95. ISBN 0-471-93884-X*, Vol. 75 (1995) pp. 222–222, https://onlinelibrary.wiley.com/doi/pdf/10.1002/zamm.19950750309 .

[14] J. H. Ferziger and M. Peric, *Computational Methods for Fluid Dynamics* (Springer, 2002).

[15] R. D. Blandford and K. S. Thorne, *Applications of Classical Physics* (Stanford University and California Institute of Technology, 2013).

[16] D. M. Sullivan, *Electromagnetic simulation using the FDTD method* (IEEE press, 2000).

[17] K. Yee, *Numerical solution of initial boundary value problems involving maxwell's equations in isotropic media,* IEEE Trans. Antennas Propag. **14**, 302 (1966).

[18] J. Rose, *Ultrasonic Waves in Solid Media*, Ultrasonic Waves in Solid Media (Cambridge University Press, 2004).

[19] C. Thomsen, H. Maris, and J. Tauc, *Picosecond acoustics as a nondestructive tool for the characterization of very thin films,* Thin Solid Films **154**, 217 (1987).

[20] O. B. Wright and K. Kawashima, *Coherent phonon detection from ultrafast surface vibrations,* Phys. Rev. Lett. **69**, 1668 (1992).

[21] V. Gusev, *Generation of inhomogeneous bulk plane acoustic modes by laser-induced thermoelastic grating near mechanically free surface,* Journal of Applied Physics **107**, 114906 (2010).

[22] T. Pezeril, P. Ruello, S. Gougeon, N. Chigarev, D. Mounier, J.-M. Breteau, P. Picart, and V. Gusev, *Generation and detection of plane coherent shear picosecond acoustic pulses by lasers: Experiment and theory,* Phys. Rev. B **75**, 174307 (2007).

[23] D. Schneider, T. Witke, T. Schwarz, B. Schöneich, and B. Schultrich, *Testing ultra-thin films by laser-acoustics,* Surface and Coatings Technology **126**, 136 (2000).

[24] T. Saito, O. Matsuda, M. Tomoda, and O. B. Wright, *Imaging gigahertz surface acoustic waves through the photoelastic effect,* J. Opt. Soc. Am. B **27**, 2632 (2010).

[25] J. A. Rogers, A. A. Maznev, M. J. Banet, and K. A. Nelson, *Optical generation and characterization of acoustic waves in thin films: Fundamentals and applications,* Annual Review of Materials Science **30**, 117 (2000), https://doi.org/10.1146/annurev.matsci.30.1.117 .

[26] Z. Su and L. Ye, *Fundamentals and analysis of lamb waves,* in *Identification of Damage Using Lamb Waves: From Fundamentals to Applications* (Springer London, London, 2009) pp. 15–58.

[27] J. A. Rogers, L. Dhar, and K. A. Nelson, *Noncontact determination of transverse isotropic elastic moduli in polyimide thin films using a laser based ultrasonic method,* Applied Physics Letters **65**, 312 (1994), https://doi.org/10.1063/1.112356 .

[28] Q. Xie, S. Mezil, P. H. Otsuka, M. Tomoda, J. Laurent, O. Matsuda, Z. Shen, and O. B. Wright, *Imaging gigahertz zero-group-velocity lamb waves,* Nat. Commun. **10**, 2228 (2019).

[29] C. Rossignol, J. M. Rampnoux, M. Perton, B. Audoin, and S. Dilhaire, *Generation and detection of shear acoustic waves in metal submicrometric films with ultrashort laser pulses,* Phys. Rev. Lett. **94**, 166106 (2005).

[30] T. Dehoux, N. Chigarev, C. Rossignol, and B. Audoin, *Three-dimensional elasto-optical interaction for reflectometric detection of diffracted acoustic fields in picosecond ultrasonics,* Phys. Rev. B **76**, 024311 (2007).

[31] H. Zhang, A. Antoncecchi, S. Edward, P. Planken, and S. Witte, *Ultrafast laser-induced guided elastic waves in a freestanding aluminum membrane,* Phys. Rev. B **103**, 064303 (2021).

[32] A. Devos and C. Lerouge, *Evidence of laser-wavelength effect in picosecond ultrasonics: Possible connection with interband transitions,* Phys. Rev. Lett. **86**, 2669 (2001).

[33] H. J. Eichler and A. Hermerschmidt, *Light-induced dynamic gratings and photorefraction,* in *Photorefractive Materials and Their Applications 1: Basic Effects* (Springer New York, New York, NY, 2006).

[34] T. F. Crimmins, A. A. Maznev, and K. A. Nelson, *Transient grating measurements of picosecond acoustic pulses in metal films,* Applied Physics Letters **74**, 1344 (1999).

[35] R. M. Slayton and K. A. Nelson, *Picosecond acoustic transmission measurements. i. transient grating generation and detection of acoustic responses in thin metal films,* The Journal of Chemical Physics **120**, 3908 (2004).

[36] S. Edward, A. Antoncecchi, H. Zhang, H. Sielcken, S. Witte, and P. C. M. Planken, *Detection of periodic structures through opaque metal layers by optical measurements of ultrafast electron dynamics,* Opt. Express **26**, 23380 (2018).

[37] T. Avanesian and P. Christopher, *Adsorbate specificity in hot electron driven photochemistry on catalytic metal surfaces,* The Journal of Physical Chemistry C **118**, 28017 (2014), https://doi.org/10.1021/jp509555m .

[38] J. Gadzuk, *Hot-electron femtochemistry at surfaces: on the role of multiple electron processes in desorption,* Chemical Physics **251**, 87 (2000).

[39] P. B. Corkum, F. Brunel, N. K. Sherman, and T. Srinivasan-Rao, *Thermal response of metals to ultrashort-pulse laser excitation,* Phys. Rev. Lett. **61**, 2886 (1988).

[40] G. K. P. Ramanandan, G. Ramakrishnan, N. Kumar, A. J. L. Adam, and P. C. M. Planken, *Emission of terahertz pulses from nanostructured metal surfaces,* Journal of Physics D: Applied Physics **47**, 374003 (2014).

[41] G. Ramakrishnan and P. C. M. Planken, *Percolation-enhanced generation of terahertz pulses by optical rectification on ultrathin gold films,* Opt. Lett. **36**, 2572 (2011).

[42] F. Kadlec, P. Kužel, and J.-L. Coutaz, *Optical rectification at metal surfaces,* Opt. Lett. **29**, 2674 (2004).

[43] F. Kadlec, P. Kužel, and J.-L. Coutaz, *Study of terahertz radiation generated by optical rectification on thin gold films,* Opt. Lett. **30**, 1402 (2005).

[44] W. S. Fann, R. Storz, H. W. K. Tom, and J. Bokor, *Direct measurement of nonequilibrium electron-energy distributions in subpicosecond laser-heated gold films,* Phys. Rev. Lett. **68**, 2834 (1992).

[45] W. S. Fann, R. Storz, H. W. K. Tom, and J. Bokor, *Electron thermalization in gold,* Phys. Rev. B **46**, 13592 (1992).

[46] C. Suárez, W. E. Bron, and T. Juhasz, *Dynamics and transport of electronic carriers in thin gold films,* Phys. Rev. Lett. **75**, 4536 (1995).

[47] T. Juhasz, H. E. Elsayed-Ali, G. O. Smith, C. Suárez, and W. E. Bron, *Direct measurements of the transport of nonequilibrium electrons in gold films with different crystal structures,* Phys. Rev. B **48**, 15488 (1993).

[48] J. Hohlfeld, J. G. Müller, S.-S. Wellershoff, and E. Matthias, *Time-resolved thermoreflectivity of thin gold films and its dependence on film thickness (appl. phys. b 64, 387f–390 (1997)),* Applied Physics B **65**, 681 (1997).

[49] J. Hohlfeld, D. Grosenick, U. Conrad, and E. Matthias, *Femtosecond time-resolved reflection second-harmonic generation on polycrystalline copper,* Applied Physics A **60**, 137 (1995).

[50] S. D. Brorson, A. Kazeroonian, J. S. Moodera, D. W. Face, T. K. Cheng, E. P. Ippen, M. S. Dresselhaus, and G. Dresselhaus, *Femtosecond room-temperature measurement of the electron-phonon coupling constant γ in metallic superconductors,* Phys. Rev. Lett. **64**, 2172 (1990).

[51] J. L. Hostetler, A. N. Smith, D. M. Czajkowsky, and P. M. Norris, *Measurement of the electron-phonon coupling factor dependence on film thickness and grain size in au, cr, and al,* Appl. Opt. **38**, 3614 (1999).

[52] P. E. Hopkins and P. M. Norris, *Substrate influence in electron?phonon coupling measurements in thin au films,* Applied Surface Science **253**, 6289 (2007), proceedings of the Fifth International Conference on Photo-Excited Processes and Applications.

[53] T. Juhasz, H. E. Elsayed-Ali, X. H. Hu, and W. E. Bron, *Time-resolved thermoreflectivity of thin gold films and its dependence on the ambient temperature,* Phys. Rev. B **45**, 13819 (1992).

[54] W. M. Ibrahim, H. E. Elsayed-Ali, C. E. Bonner, and M. Shinn, *Ultrafast investigation of electron dynamics in multi-layer metals,* International Journal of Heat and Mass Transfer **47**, 2261 (2004).

[55] J. Guo, T. Wang, D. Wang, J. Shao, A. Chen, and M. Jin, *Simulation of thermionic emission optimization in femtosecond laser irradiation metal film by two-layer structure,* Applied Physics A **117**, 1367 (2014).

[56] A. Chen, L. Sui, Y. Shi, Y. Jiang, D. Yang, H. Liu, M. Jin, and D. Ding, *Ultrafast investigation of electron dynamics in the gold-coated two-layer metal films,* Thin Solid Films **529**, 209 (2013), tACT2011 International Thin Films Conference.

[57] R. H. M. Groeneveld, R. Sprik, and A. Lagendijk, *Effect of a non-thermal electron distribution on the electron-phonon energy relaxation process in noble metals,* Phys. Rev. B **45**, 5079 (1992).

[58] T. Qiu and C. Tien, *Short-pulse laser heating on metals,* International Journal of Heat and Mass Transfer **35**, 719 (1992).

[59] A. N. Smith and P. M. Norris, *Influence of intraband transitions on the electron thermoreflectance response of metals,* Applied Physics Letters **78**, 1240 (2001), https://doi.org/10.1063/1.1351523 .

[60] P. E. Hopkins, J. L. Kassebaum, and P. M. Norris, *Effects of electron scattering at metal-nonmetal interfaces on electron-phonon equilibration in gold films,* Journal of Applied Physics **105**, 023710 (2009), https://doi.org/10.1063/1.3068476 .

[61] M. Aeschlimann, M. Bauer, S. Pawlik, W. Weber, R. Burgermeister, D. Oberli, and H. C. Siegmann, *Ultrafast spin-dependent electron dynamics in fcc co,* Phys. Rev. Lett. **79**, 5158 (1997).

[62] S. D. Brorson, J. G. Fujimoto, and E. P. Ippen, *Femtosecond electronic heat-transport dynamics in thin gold films,* Phys. Rev. Lett. **59**, 1962 (1987).

[63] C.-K. Sun, F. Vallée, L. H. Acioli, E. P. Ippen, and J. G. Fujimoto, *Femtosecond-tunable measurement of electron thermalization in gold,* Phys. Rev. B **50**, 15337 (1994).

[64] C.-K. Sun, F. Vallée, L. Acioli, E. P. Ippen, and J. G. Fujimoto, *Femtosecond investigation of electron thermalization in gold,* Phys. Rev. B **48**, 12365 (1993).

[65] G. D. Tsibidis, *Thermal response of double-layered metal films after ultrashort pulsed laser irradiation: The role of nonthermal electron dynamics,* Applied Physics Letters **104**, 051603 (2014), https://doi.org/10.1063/1.4863959 .

[66] W. Wang and D. G. Cahill, *Limits to thermal transport in nanoscale metal bilayers due to weak electron-phonon coupling in au and cu,* Phys. Rev. Lett. **109**, 175503 (2012).

[67] A. M. Chen, Y. F. Jiang, L. Z. Sui, H. Liu, M. X. Jin, and D. J. Ding, *Thermal analysis of double-layer metal films during femtosecond laser heating,* Journal of Optics **13**, 055503 (2011).

[68] G.-M. Choi, R. B. Wilson, and D. G. Cahill, *Indirect heating of pt by short-pulse laser irradiation of au in a nanoscale pt/au bilayer,* Phys. Rev. B **89**, 064307 (2014).

[69] A. Chen, H. Xu, Y. Jiang, L. Sui, D. Ding, H. Liu, and M. Jin, *Modeling of femtosecond laser damage threshold on the two-layer metal films,* Applied Surface Science **257**, 1678 (2010).

[70] S. Anisimov, B. Kapeliovich, and T. Perel-man, *Electron emission from metal surfaces exposed to ultrashort laser pulses,* Journal of Experimental and Theoretical Physics **66**, 375 (1974).

[71] J. Güdde, J. Hohlfeld, J. Müller, and E. Matthias, *Damage threshold dependence on electron–phonon coupling in au and ni films,* Applied Surface Science **127-129**, 40 (1998).

[72] H. E. Elsayed-Ali, T. B. Norris, M. A. Pessot, and G. A. Mourou, *Time-resolved observation of electron-phonon relaxation in copper,* Phys. Rev. Lett. **58**, 1212 (1987).

[73] P. B. Johnson and R. W. Christy, *Optical constants of the noble metals,* Phys. Rev. B **6**, 4370 (1972).

[74] M. Perner, P. Bost, U. Lemmer, G. von Plessen, J. Feldmann, U. Becker, M. Mennig, M. Schmitt, and H. Schmidt, *Optically induced damping of the surface plasmon resonance in gold colloids,* Phys. Rev. Lett. **78**, 2192 (1997).

[75] C. Thomsen, H. T. Grahn, H. J. Maris, and J. Tauc, *Surface generation and detection of phonons by picosecond light pulses,* Phys. Rev. B **34**, 4129 (1986).

[76] O. B. Wright, *Ultrafast nonequilibrium stress generation in gold and silver,* Phys. Rev. B **49**, 9985 (1994).

[77] P. J. S. van Capel and J. I. Dijkhuis, *Time-resolved interferometric detection of ultrashort strain solitons in sapphire,* Phys. Rev. B **81**, 144106 (2010).

[78] A. Devos and A. LeLouarn, *Strong effect of interband transitions in the picosecond ultrasonics response of metallic thin films,* Phys. Rev. B **68**, 045405 (2003).

[79] J.-W. Kim, M. Vomir, and J.-Y. Bigot, *Ultrafast magnetoacoustics in nickel films,* Phys. Rev. Lett. **109**, 166601 (2012).

[80] T. Saito, O. Matsuda, and O. B. Wright, *Picosecond acoustic phonon pulse generation in nickel and chromium,* Phys. Rev. B **67**, 205421 (2003).

[81] O. Matsuda, O. B. Wright, D. H. Hurley, V. Gusev, and K. Shimizu, *Coherent shear phonon generation and detection with picosecond laser acoustics,* Phys. Rev. B **77**, 224110 (2008).

[82] O. Matsuda, M. Tomoda, T. Tachizaki, S. Koiwa, A. Ono, K. Aoki, R. P. Beardsley, and O. B. Wright, *Ultrafast ellipsometric interferometry for direct detection of coherent phonon strain pulse profiles,* J. Opt. Soc. Am. B **30**, 1911 (2013).

[83] R. M. Slayton, K. A. Nelson, and A. A. Maznev, *Transient grating measurements of film thickness in multilayer metal films,* Journal of Applied Physics **90**, 4392 (2001).

[84] C. He, O. Ristow, M. Grossmann, D. Brick, Y. Guo, M. Schubert, M. Hettich, V. Gusev, and T. Dekorsy, *Acoustic waves undetectable by transient reflectivity measurements,* Phys. Rev. B **95**, 184302 (2017).

[85] Q. Li, K. Hoogeboom-Pot, D. Nardi, M. M. Murnane, H. C. Kapteyn, M. E. Siemens, E. H. Anderson, O. Hellwig, E. Dobisz, B. Gurney, R. Yang, and K. A. Nelson, *Generation and control of ultrashort-wavelength two-dimensional surface acoustic waves at nanoscale interfaces,* Phys. Rev. B **85**, 195431 (2012).

[86] J. N. Hernandez-Charpak, K. M. Hoogeboom-Pot, Q. Li, T. D. Frazer, J. L. Knobloch, M. Tripp, S. W. King, E. H. Anderson, W. Chao, M. M. Murnane, H. C. Kapteyn, and D. Nardi, *Full characterization of the mechanical properties of 11?50 nm ultrathin films: Influence of network connectivity on the poisson?s ratio,* Nano Lett. **17**, 2178 (2017).

[87] J. J. Kasinski, L. Gomez-Jahn, K. J. Leong, S. M. Gracewski, and R. J. D. Miller, *Optical generation of coherent surface acoustics: an optically based probe of surface structure and dynamics,* Opt. Lett. **13**, 710 (1988).

[88] K. Naugolnykh and L. Ostrovsky, *Nonlinear Wave Processes in Acoustics* (Cambridge University Press, 1998).

[89] B. C. Daly, K. Kang, Y. Wang, and D. G. Cahill, *Picosecond ultrasonic measurements of attenuation of longitudinal acoustic phonons in silicon,* Phys. Rev. B **80**, 174112 (2009).

[90] D. Li and D. G. Cahill, *Attenuation of 7 ghz surface acoustic waves on silicon,* Phys. Rev. B **94**, 104306 (2016).

[91] A. Devos, M. Foret, S. Ayrinhac, P. Emery, and B. Ruffle, *Hypersound damping in vitreous silica measured by picosecond acoustics,* Phys. Rev. B **77**, 100201(R) (2008).

[92] A. M. Lomonosov, P. Hess, and A. P. Mayer, *Observation of solitary elastic surface pulses,* Phys. Rev. Lett. **88**, 076104 (2002).

[93] D. Nardi, M. Travagliati, M. E. Siemens, Q. Li, M. M. Murnane, H. C. Kapteyn, G. Ferrini, F. Parmigiani, and F. Banfi, *Probing thermomechanics at the nanoscale: Impulsively excited pseudosurface acoustic waves in hypersonic phononic crystals,* Nano Lett. **11**, 4126 (2011).

[94] O. L. Muskens and J. I. Dijkhuis, *High amplitude, ultrashort, longitudinal strain solitons in sapphire,* Phys. Rev. Lett. **89**, 285504 (2002).

[95] V. V. Temnov, C. Klieber, K. A. Nelson, T. Thomay, V. Knittel, A. Leitenstorfer, D. Makarov, M. Albrecht, and R. Bratschitsch, *Femtosecond nonlinear ultrasonics in gold probed with ultrashort surface plasmons,* Nat. Commun. **4**, 1468 (2013).

[96] S. Edward, H. Zhang, I. Setija, V. Verrina, A. Antoncecchi, S. Witte, and P. Planken, *Detection of hidden gratings through multilayer nanostructures using light and sound,* Phys. Rev. Applied **14**, 014015 (2020).

[97] P. M. Shearer, *Introduction to Seismology* (Cambridge University Press, New York, 2009).

[98] D. M. Sullivan, *Electromagnetic simulation using the FDTD method* (IEEE press, 2000).

[99] M. Born and E. Wolf, *Principles of Optics* (Cambridge University Press, Cambridge., 1999).

[100] H. Lamb, *On waves in an elastic plate,* Proc. R. Soc. Lond. A. **93**, 114 (1917).

[101] R. B. Wilson, B. A. Apgar, L. W. Martin, and D. G. Cahill, *Thermoreflectance of metal transducers for optical pump-probe studies of thermal properties,* Opt. Express **20**, 28829 (2012).

[102] T.Favaloro, J.-H. Bahk, and A. Shakouri, *Characterization of the temperature dependence of the thermoreflectance coefficient for conductive thin films,* Rev. Sci. Instrum **86**, 024903 (2015).

[103] Y. Wang, J. Y. Park, Y. K. Koh, and D. G. Cahill, *Thermoreflectance of metal transducers for time-domain thermoreflectance,* J. Appl. Phys **108**, 043507 (2010).

[104] A. G. MATHEWSON and H. P. MYERS, *Optical absorption in aluminium and the effect of temperature,* J. Phys. F: Metal Phys. **2**, 403 (1972).

[105] A. Akhiezer, J. Phys (USSR) **1**, 277 (1939).

[106] S. K. Kor, U. S. Tandon, and G. Rai, *Ultrasonic attenuation in copper, silver, and gold,* Phys. Rev. B **6**, 2195 (1972).

[107] H. N. Lin, R. J. Stoner, H. J. Maris, and J. Tauc, *Phonon attenuation and velocity measurements in transparent materials by picosecond acoustic interferometry,* Journal of Applied Physics **69**, 3816 (1991).

[108] O. Matsuda, T. Pezeril, I. Chaban, K. Fujita, and V. Gusev, *Time-domain brillouin scattering assisted by diffraction gratings,* Phys. Rev. B **97**, 064301 (2018).

[109] A. Devos, R. Côte, G. Caruyer, and A. Lefèvre, *A different way of performing picosecond ultrasonic measurements in thin transparent films based on laser-wavelength effects,* Applied Physics Letters **86**, 211903 (2005).

[110] V. E. Gusev and P. Ruello, *Advances in applications of time-domain brillouin scattering for nanoscale imaging,* Applied Physics Reviews **5**, 031101 (2018).

[111] A. Bertholds and R. Dandliker, *Determination of individual strain-optic coefficients in single-mode optical fibers,* J. Light. Technol. **6**, 17 (1988).

[112] D. R. Lide, *CRC Handbook of Chemistry and Physics, Internet Version 2005* (CRC Press, Boca Raton, FL, 2005).

[113] R. H. M. Groeneveld, R. Sprik, and A. Lagendijk, *Femtosecond spectroscopy of electron-electron and electron-phonon energy relaxation in ag and au,* Phys. Rev. B **51**, 11433 (1995).

[114] M. Metcalfe, S. M. Carr, A. Muller, G. S. Solomon, and J. Lawall, *Resolved sideband emission of* InAs/GaAs *quantum dots strained by surface acoustic waves,* Phys. Rev. Lett. **105**, 037401 (2010).

[115] K. J. Satzinger, Y. P. Zhong, H. S. Chang, G. A. Peairs, A. Bienfait, M.-H. Chou, A. Y. Cleland, C. R. Conner, E. Dumur, J. Grebel, I. Gutierrez, B. H. November, R. G. Povey, S. J. Whiteley, D. D. Awschalom, D. I. Schuster, and A. N. Cleland, *Quantum control of surface acoustic-wave phonons,* Nature **563**, 661 (2018).

[116] Y. Chu, P. Kharel, W. H. Renninger, L. D. Burkhart, L. Frunzio, P. T. Rakich, and R. J. Schoelkopf, *Quantum acoustics with superconducting qubits,* Science **358**, 199 (2017).

[117] B. C. Daly, T. B. Norris, J. Chen, and J. B. Khurgin, *Picosecond acoustic phonon pulse propagation in silicon,* Phys. Rev. B **70**, 214307 (2004).

[118] K.-H. Lin, C.-T. Yu, S.-Z. Sun, H.-P. Chen, C.-C. Pan, J.-I. Chyi, S.-W. Huang, P.-C. Li, and C.-K. Sun, *Two-dimensional nanoultrasonic imaging by using acoustic nanowaves,* Appl. Phys. Lett. **89**, 043106 (2006).

[119] B. Giammarinaro, D. Espindola, F. Coulouvrat, and G. Pinton, *Focusing of shear shock waves,* Phys. Rev. Applied **9**, 014011 (2018).

[120] S. Mezil, F. Bruno, S. Raetz, J. Laurent, and D. Royer, *Investigation of interfacial stiffnesses of a tri-layer using zero-group velocity lamb modes,* J. Acoust. Soc. Am. **138**, 3202 (2015).

[121] G. Yan, S. Raetz, N. Chigarev, V. E. Gusev, and V. Tournat, *Characterization of progressive fatigue damage in solid plates by laser ultrasonic monitoring of zero-group-velocity lamb modes,* Phys. Rev. Applied **9**, 061001 (2018).

[122] D. M. Photiadis, M. K. Zalalutdinov, A. S. Bracker, S. G. Carter, D. Gammon, and B. H. Houston, *Photoexcited elastic waves in freestanding gaas films,* Phys. Rev. B **101**, 245304 (2020).

[123] M. Grossmann, O. Ristow, M. Hettich, C. He, R. Waitz, E. Scheer, V. Gusev, T. Dekorsy, and M. Schubert, *Time-resolved detection of propagating lamb waves in thin silicon membranes with frequencies up to 197 GHz,* Appl. Phys. Lett. **106**, 171904 (2015).

[124] T. Tachizaki, T. Muroya, O. Matsuda, Y. Sugawara, D. H. Hurley, and O. B. Wright, *Scanning ultrafast sagnac interferometry for imaging two-dimensional surface wave propagation,* Review of Scientific Instruments **77**, 043713 (2006), https://doi.org/10.1063/1.2194518 .

[125] J. L. Rose, *Ultrasonic Guided Waves in Solid Media* (Cambridge University Press, 2014).

[126] B. Lüthi, *Physical Acoustics in the Solid State* (Springer, Berlin, Heidelberg, 2005).

[127] H. Zhang, A. Antoncecchi, S. Edward, P. Planken, and S. Witte, *Enhancing the detection of laser-excited strain waves via transparent nanolayers,* Phys. Rev. B **104**, 205416 (2021).

[128] H.-Y. Hao and H. J. Maris, *Experiments with acoustic solitons in crystalline solids,* Phys. Rev. B **64**, 064302 (2001).

[129] J. H. Lopes, M. A. B. Andrade, J. P. Leao-Neto, J. C. Adamowski, I. V. Minin, and G. T. Silva, *Focusing acoustic beams with a ball-shaped lens beyond the diffraction limit,* Phys. Rev. Applied **8**, 024013 (2017).

[130] A. Antoncecchi, H. Zhang, S. Edward, V. Verrina, P. C. M. Planken, and S. Witte, *High-resolution microscopy through optically opaque media using ultrafast photoacoustics,* Opt. Express **28**, 33937 (2020).

[131] V. Verrina, S. Edward, H. Zhang, S. Witte, and P. C. M. Planken, *Photoacoustic detection of low duty cycle gratings through optically opaque layers,* Appl. Phys. Lett. **117**, 051104 (2020).

[132] B. A. Auld, *Acoustic Fields and Waves in Solids Vol. 1* (Wiley, New York, 1973).

[133] J. Evertsson, F. Bertram, F. Zhang, L. Rullik, L. Merte, M. Shipilin, M. Soldemo, S. Ahmadi, N. Vinogradov, F. Carlà, J. Weissenrieder, M. Göthelid, J. Pan, A. Mikkelsen, J.-O. Nilsson, and E. Lundgren, *The thickness of native oxides on aluminum alloys and single crystals,* Applied Surface Science **349**, 826 (2015).

[134] H. Schwenke, U. Neuschaefer-Rube, T. Pfeifer, and H. Kunzmann, *Optical methods for dimensional metrology in production engineering,* CIRP Annals **51**, 685 (2002).

[135] N. Mokhlesi and R. Scheuerlein, *Three dimensional nand memory,* US Patent **US7851851B2** (2007).

[136] H. Kim, S. Ahn, Y. G. Shin, K. Lee, and E. Jung, *Evolution of nand flash memory: From 2d to 3d as a storage market leader,* in *2017 IEEE International Memory Workshop (IMW)* (2017) pp. 1–4.

[137] A. G. Every and W. Sachse, *Determination of the elastic constants of anisotropic solids from acoustic-wave group-velocity measurements,* Phys. Rev. B **42**, 8196 (1990).

[138] B. Audoin, M. Perton, N. Chigarev, and C. Rossignol, *Diffraction of picosecond bulk longitudinal and shear waves in micron thick films; application to their nondestructive evaluation,* Ultrasonics **48**, 574 (2008), selected Papers from ICU 2007.

[139] O. B. Wright and V. E. Gusev, *Acoustic generation in crystalline silicon with femtosecond optical pulses,* Applied Physics Letters **66**, 1190 (1995).

[140] B. C. Daly, N. C. R. Holme, T. Buma, C. Branciard, T. B. Norris, D. M. Tennant, J. A. Taylor, J. E. Bower, and S. Pau, *Imaging nanostructures with coherent phonon pulses,* Applied Physics Letters **84**, 5180 (2004), https://doi.org/10.1063/1.1764599 .

[141] S. Ramanathan and D. G. Cahill, *High-resolution picosecond acoustic microscopy for non-invasive characterization of buried interfaces,* Journal of Materials Research **21**, 1204–1208 (2006).

[142] S.-S. Wellershoff, J. Güdde, J. Hohlfeld, J. Muller, and E. Matthias, *Role of electron-phonon coupling in femtosecond laser damage of metals,* Proc. SPIE **3343** (1998).

[143] S. Najafi and K. Madanipour, *Measurement of the modulation transfer function of a charge-coupled device array by the combination of the self-imaging effect and slanted edge method,* Appl. Opt. **52**, 4724 (2013).

[144] J. W. Coltman, *The specification of imaging properties by response to a sine wave input,* J. Opt. Soc. Am. **44**, 468 (1954).

Acknowledgements

I want to dedicate the final words of this manuscript to thank all the people who in the past years have helped me, encouraged me and had fun with me.

I want to start by thanking Stefan! You are the best supervisor I could have asked for: your optimism and patience helped me overcome moments in which I struggled to see any positive outcome for my PhD. At the end of my second year, I asked you for a side-project in case the photoacoustic imaging would not have worked. You answered me that, in a short time, I was going to be flooded by data to analyze, and a side-project would have been unnecessary. This is one of many examples of the trust you put in me, which I can only hope to have repaid a little bit. In general, all the discussions with you were always very inspiring and constructive, and you taught me how to critically approach the obstacles I had to face during my experiments. Besides being my supervisor, you are an interesting person to be around and spend time with. Thanks to your humour and simplicity, you have created a great atmosphere within the group during all our activities: meetings, lunches and outings. I will always be grateful for all this!

Next, I would like to thank Kjeld. You were always happy to answer my questions and share your opinion, even though you were not entirely involved in the photoacoustic project. It was remarkable how the famous "only 5 minutes" you said you could give were transformed into half hours or more, carried on by your contagious enthusiasm for experiments and physics.

I would like to give credits to my close collaborators. Stephen, we started this project together. However, you quickly became a real expert (:P) on the pump-probe technique, and I could rely on you if I needed some help or somebody to talk to. After a few adjustments, working with you became natural. We became very good friends, and I am happy to share my scientific success with you.

Hao, we have worked together on all the projects. Your support in modelling and your criticism helped me a lot scientifically. You also have encouraged me not to give up, and you trusted me and my experimental results all these

years. It was nice having you in the office. You were very quiet but always ready to say your very honest opinion in front of the whiteboard or one of the plots I was proudly showing you. In England, at one of the conferences we attended, I also had the great pleasure of seeing you play football and being tipsy. Thanks a lot and I hope we can meet again!!

Maksym and Matthijs, although my contract was already over, you kept me involved and updated me on the evolution of the project. I am sure your PhD's will be successful, as you have already shown what skilful scientists you are.

I want to thank all the other members of the EUV Generation and Imaging group: Nik, Tiago, Aneta, Lars F., Maisie, Randy, Thijs, Jan, Lars L., Dirk, Faisal, Kevin, Anne, Amelie and Zeudi. The group quickly grew, but every addition was a perfect match. Thanks for the fun group meetings, scientific discussions and fun coffee breaks we had together.

I should not forget that the Photoacoustic project started as a collaboration with the EUV-target group led by Prof. Paul Planken. Paul, thank you for "adopting" me in your laboratory and allowing me to use the equipment, including the laser systems. Vanessa, the final version of my setup was built next to yours, and then the results started to arrive. The optical table was just one of the many things we have shared in Amsterdam, among which: the house, the office and even a project. I was very lucky to meet you and to work with you. Guido and Thomas, thank you for the friendly atmosphere in the lab.

Marjan and Joost, thanks for the full support I had during these years from the management of ARCNL. Also, I would like to thank the ARCNL/AMOLF support staff, the electronic and software department, ICT and the Nanocenter staff.

Amsterdam has not only been a great place to start and develop my professional career, but it is where I met many new friends from all over the world, even though the Italian community was often the largest one. To all of you, thanks! We have shared many fun and crazy moments, but also some hard and sad ones as well. But thanks to you, I managed to overcome every difficulty, and together we survived a pandemic. The few lines I wrote are not enough to express how grateful I am for having met all of you.

Finally, I would like to thank my whole family for their unconditional love and support.